

Chulalongkorn University

## Chula Digital Collections

---

Chulalongkorn University Theses and Dissertations (Chula ETD)

---

2021

### A numerical study of flow past arrays of cylinders at low Reynolds number

Woraphon Wannaviroj  
*Faculty of Engineering*

Follow this and additional works at: <https://digital.car.chula.ac.th/chulaetd>



Part of the [Applied Mechanics Commons](#), and the [Engineering Mechanics Commons](#)

---

#### Recommended Citation

Wannaviroj, Woraphon, "A numerical study of flow past arrays of cylinders at low Reynolds number" (2021). *Chulalongkorn University Theses and Dissertations (Chula ETD)*. 4781.  
<https://digital.car.chula.ac.th/chulaetd/4781>

This Thesis is brought to you for free and open access by Chula Digital Collections. It has been accepted for inclusion in Chulalongkorn University Theses and Dissertations (Chula ETD) by an authorized administrator of Chula Digital Collections. For more information, please contact [ChulaDC@car.chula.ac.th](mailto:ChulaDC@car.chula.ac.th).

A numerical study of flow past arrays of cylinders at low Reynolds number



Mr. Woraphon Wannaviroj

A Thesis Submitted in Partial Fulfillment of the Requirements  
for the Degree of Master of Engineering in Mechanical Engineering

Department of Mechanical Engineering

FACULTY OF ENGINEERING

Chulalongkorn University

Academic Year 2021

Copyright of Chulalongkorn University

การศึกษาด้วยวิธีการทางตัวเลขของการไหลผ่านกลุ่มของทรงกระบอกที่เรย์โนลด์ส์นับเบอร์ต่ำ



นายวรพล วรรณวิโรจน์

วิทยานิพนธ์นี้เป็นส่วนหนึ่งของการศึกษาตามหลักสูตรปริญญาวิศวกรรมศาสตรมหาบัณฑิต

สาขาวิชาวิศวกรรมเครื่องกล ภาควิชาวิศวกรรมเครื่องกล

คณะวิศวกรรมศาสตร์ จุฬาลงกรณ์มหาวิทยาลัย

ปีการศึกษา 2564

ลิขสิทธิ์ของจุฬาลงกรณ์มหาวิทยาลัย

Thesis Title	A numerical study of flow past arrays of cylinders at low Reynolds number
By	Mr. Woraphon Wannaviroj
Field of Study	Mechanical Engineering
Thesis Advisor	KARU CHONGSIRIPINYO, Ph.D.

---

Accepted by the FACULTY OF ENGINEERING, Chulalongkorn University in  
Partial Fulfillment of the Requirement for the Master of Engineering

..... Dean of the FACULTY OF  
ENGINEERING  
(Professor SUPOT TEACHAVORASINSKUN, D.Eng.)

THESIS COMMITTEE

..... Chairman  
(Assoc. Prof. ALONGKORN PIMPIN, Ph.D.)  
..... Thesis Advisor  
(KARU CHONGSIRIPINYO, Ph.D.)  
..... Examiner  
(Assistant Professor Saran Salakij, Ph.D.)  
..... External Examiner  
(Associate Professor Vejapong Juttijudata, Ph.D.)



วรพล วรณวิโรจน์ : การศึกษาด้วยวิธีการทางตัวเลขของการไหลผ่านกลุ่มของทรงกระบอกที่เรย์  
โนลด์นัมเบอร์ต่ำ. ( A numerical study of flow past arrays of cylinders at low Reynolds  
number) อ.ที่ปรึกษาหลัก : ดร.การุญ จงศิริภิญโญ

การกัดเซาะชายฝั่งตามแนวชายฝั่งแพร่หลายเพิ่มมากขึ้น วิธีการบรรเทาปัญหาที่ได้รับความนิยมคือ  
การใช้เขื่อนกันคลื่นที่ทำจากไม้ไผ่ซึ่งเป็นที่ยอมรับว่า "รู้ไม่ผิด" วิทยานิพนธ์ฉบับนี้ใช้วิธีการคำนวณตรวจสอบการไหล  
สม่ำเสมอที่ความเร็วต่ำผ่านการจัดเรียงรูปแบบตามเลขาคณิตที่หลายของรั้วไม้ไผ่โดยถูกจำลองด้วยแถวของวัตถุ  
ทรงกระบอกโดยใช้โปรแกรม ANSYS®-Fluent เรย์โนลด์นัมเบอร์ซึ่งขึ้นอยู่กับความเร็วการไหลเข้า ( $U_\infty$ ), เส้นผ่าน  
ศูนย์กลางของทรงกระบอก (D) และความหนืดจลนศาสตร์ของของไหลมีค่า  $Re = 100$  โดยมีการตรวจสอบการ  
การรวมกันของ mesh และ ขนาดของ time-step การไหลผ่านวัตถุทรงกระบอกกลมเดี่ยวแบบสองมิติ สำหรับ  
วัตถุทรงกระบอกสองชั้นที่ถูกจัดเรียงแบบหน้ากระดานถูกพบว่ามีระยะห่างระหว่างกัน (T) กลายเป็นเรื่องเล็กน้อย  
แทบไม่มีความหมายเมื่อ  $T/D = 15$  สำหรับการจัดเรียงแถวของวัตถุทรงกระบอกแบบซ้อนทับด้วย 3 ถึง  
13 คอลัมน์ ทรงกระบอกมีค่าสัมประสิทธิ์แรงกดดันใกล้เคียงกันทุกตำแหน่งยกเว้นจากตำแหน่งของคอลัมน์สุดท้าย  
ซึ่งสัมประสิทธิ์แรงกดดันมีค่าน้อยลงมาก สำหรับการจัดเรียงแบบแนวเดียวกันด้วย 3 ถึง 5 คอลัมน์ วัตถุ  
ทรงกระบอกที่คอลัมน์แรกมีขนาดแรงกดดันมากที่สุดขณะที่แรงกดดันของวัตถุทรงกระบอกที่เหลือมีค่าต่ำกว่าและ  
ใกล้เคียงกัน ความดันลดระหว่างรั้วทรงกระบอกถูกพบว่ามีสัดส่วนโดยตรงกับแรงดันรวมตามที่เสนอโดยทฤษฎี  
ผลรวมของแรงดันและความดันลดเพิ่มขึ้นอย่างเชิงเส้นตามคอลัมน์ที่ถูกเพิ่มแต่อัตราการเพิ่มมีขนาดสูงกว่า  
สำหรับการจัดวางแบบซ้อนทับ งานวิจัยยังพิจารณาชนิดของการจัดวางอื่นที่ถูกพบในโลก มันถูกพบว่าการ  
จัดเรียงแบบซิกแซกมีค่าความแรงดันรวมและความดันลดใกล้เคียงกับการจัดวางแบบซ้อนทับ 5 คอลัมน์แต่มี  
จำนวนวัตถุทรงกระบอกมากกว่า สำหรับโมดูลรูปแบบสามเหลี่ยมและรูปแบบเพชร ทรงกระบอกซ้ายสุดและขวา  
สุดจากด้านข้างมีแรงดันที่สูงที่สุด ผลรวมแรงดันและความดันลดของโมดูลรูปแบบเพชรมีค่ามากกว่าแบบ  
สามเหลี่ยมประมาณสองเท่า สำหรับรูปทรงตัวทึบและรูปทรงเส้น ค่าแรงดันรวมและความดันลดน้อยลงอย่างมี  
นัยสำคัญเทียบกับแบบซิกแซก โมดูลรูปแบบสามเหลี่ยมและรูปแบบเพชร สุดท้ายแล้วส่วนหางของรูปทรงตัวทึบ  
ผันแปรอย่างมีนัยสำคัญต่อแรงดันรวมและความดันลด

สาขาวิชา วิศวกรรมเครื่องกล

ปีการศึกษา 2564

ลายมือชื่อนิสิต .....

ลายมือชื่อ อ.ที่ปรึกษาหลัก .....

# # 6270245321 : MAJOR MECHANICAL ENGINEERING

KEYWORD: drag force, drag coefficient, array of cylinders, fluid flow, pressure drop

Woraphon Wannaviroj : A numerical study of flow past arrays of cylinders at low Reynolds number.

Advisor: KARU CHONGSIRIPINYO, Ph.D.

Coastal erosion along shorelines has increasingly been prevalent. A popular method for alleviating this problem is to use breakwaters, made of bamboo, known as “bamboo fencing”. The thesis numerically investigates steady, low-velocity flow past several geometrical configurations of bamboo fences, modelled as array of cylinders using the ANSYS®-Fluent software. The Reynolds number based on incoming flow velocity ( $U_\infty$ ), cylinder diameter ( $D$ ), and fluid kinematic viscosity is  $Re = 100$ . Validation is done for mesh convergence and time-step size for the two-dimensional flow past a circular cylinder. For a pair of side-by-side arranged cylinders, it is found that the effect of traverse gap ( $T$ ) between the cylinder becomes negligible at about  $T/D = 15$ . For the staggered arrangement of array of cylinders with 3 to 13 columns, cylinders located at any position experience similar value of drag coefficient except for those located at the last column whose drag coefficient is much smaller. For the aligned arrangement with 3 to 5 columns, cylinders at the first column experience largest drag while the drag forces of cylinders for the rest are of similar, lower value. The pressure drop across the fence of cylinders is found to be directly proportional to the combined drag, as suggested by the theory. The summation of drag force and pressure drop increase linearly as more column is added but the increasing rate is larger for the staggered configuration. The investigation also considers other types of arrangement, found in the real world. It is found that the zigzag arrangement has drag summation and pressure reduction that are only slightly larger than the 5-column staggered arrangement, while consists of a larger number of cylinders. For the triangular and diamond modules, cylinders at the far left and far right in the lateral direction experience largest drag. The summation of drag force and pressure drop of the diamond module are approximately twice as much as those of the triangle. For the T-shape and line-shape, the drag summation and pressure drop are significantly smaller relative to the zigzag, the triangular, and the diamond modules. Lastly, the tail of the T-shape does not significantly alter the summation of drag force and pressure drop.

CHULALONGKORN UNIVERSITY

Field of Study: Mechanical Engineering

Student's Signature .....

Academic Year: 2021

Advisor's Signature .....

## ACKNOWLEDGEMENTS

For two years and a half, this thesis has successfully accomplished with expert assistance from my thesis advisor, Karu Chongsiripinyo, who supported me wisely and generously. He also provided terrific advice and encouragement throughout on conducting this research as well as reviewing this thesis. I also would like to thank to Associate Professor Alongkorn Pimpin for being the chairman of the thesis committee, Assistant Professor Saran Salakij for being the thesis examiner, and Associate Professor Vejapong Juttijudata for being the thesis external examiner.

Woraphon Wannaviroj



## TABLE OF CONTENTS

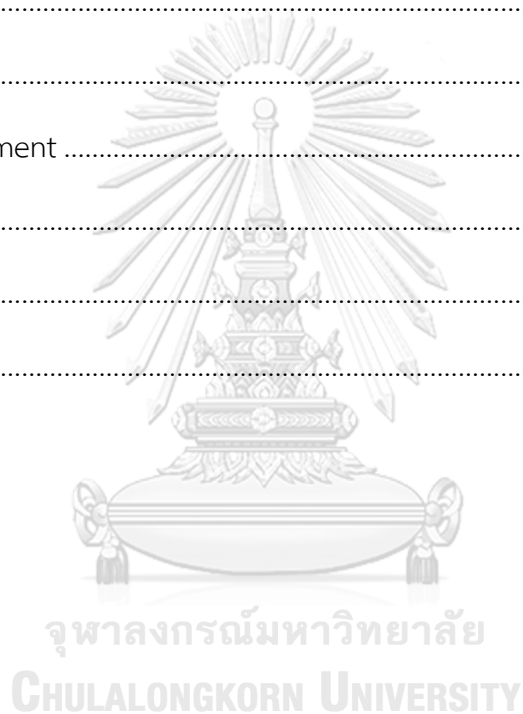
	Page
.....	iii
ABSTRACT (THAI) .....	iii
.....	iv
ABSTRACT (ENGLISH) .....	iv
ACKNOWLEDGEMENTS .....	v
TABLE OF CONTENTS .....	vi
LIST OF TABLES .....	xi
LIST OF FIGURES .....	xii
CHAPTER 1.....	18
INTRODUCTION.....	18
1.1 Solid object in fluid flows .....	18
1.2 The phenomenon of vortex shedding .....	21
1.3 Related problems .....	23
1.4 Objective of the research.....	26
1.5 The review of our thesis and scope.....	26
CHAPTER 2.....	28
RELATED THEORY AND REVIEW OF LITERATURES .....	28
2.1 Related theory .....	28
2.1.1 Governing equations .....	28
2.1.2 Non-dimensionalization of the Navier-Stokes equation.....	29
2.1.3 Reynolds number .....	30

2.1.4 Force coefficient .....	30
2.1.5 Strouhal number.....	33
2.1.6 Relating drag force and pressure with energy equation.....	34
2.1.6.1 Energy equation: First law of thermodynamics.....	34
2.1.6.2 Application of the energy equation with the Bernoulli Equation .	37
2.2 Review of literatures.....	38
2.2.1 Flow past a circular cylinder .....	38
2.2.1.1 Experiment.....	38
2.2.1.2 Numerical simulation.....	41
2.2.2 Flow past a pair of cylinders.....	45
2.2.2.1 Experiment.....	45
2.2.2.2 Numerical simulation.....	49
2.2.3 Other designs of sand fences and breakwaters .....	54
CHAPTER 3.....	57
RESEARCH METHODOLOGY AND VALIDATION .....	57
3.1 Research methodology .....	57
3.1.1 Numerical process of CFD.....	57
3.1.1.1 Problem setup .....	58
3.1.2 Finite volume method.....	59
3.1.2.1 The governing equations.....	60
3.1.2.2 Discretization of finite volume method and solution .....	61
3.1.3 Geometrical arranging description .....	63
3.1.3.1 The ‘side-by-side’ arrangement .....	63
3.1.3.2 The array arrangements of cylinders.....	65

3.2 Validation .....	67
3.2.1 Baseline case .....	68
3.2.2 Effect of time step.....	70
3.2.3 Mesh sensitivity .....	70
CHAPTER 4.....	72
PRELIMINARY RESULTS.....	72
4.1 Case $T/D = 1.5$ and 3: comparison with literatures .....	72
4.2 Effects of the gap width.....	79
CHAPTER 5.....	86
RESULTS.....	86
5.1 Mesh.....	86
5.2 Comparison: Staggered and aligned arrangements.....	88
5.2.1 Velocity vector .....	88
5.2.2 Drag coefficient and drag force.....	90
5.2.2.1 Drag coefficient on a cylinder.....	90
5.2.2.2 Drag force .....	94
5.2.3 Pressure.....	96
5.2.3.1 Pressure contour.....	96
5.2.3.2 Area-weighted averaged pressure.....	101
5.2.4 Relation of drag force and pressure .....	107
5.3 Additional columns for staggered arrangement .....	110
5.3.1 Drag coefficient and drag force.....	111
5.3.1.1 Drag coefficient on a cylinder.....	111
5.3.1.2 Drag force .....	114

5.3.2 Pressure.....	115
5.4 Other types of arrangements.....	116
5.4.1 Zigzag arrangement .....	116
5.4.1.1 Computational domain of zigzag arrangement and its position..	117
5.4.1.2 Velocity vector .....	118
5.4.1.3 Drag coefficient on a cylinder.....	119
5.4.1.4 Summation of drag force .....	120
5.4.1.5 Pressure contour and pressure drop.....	121
5.4.2 Triangular and diamond modules.....	123
5.4.2.1 Computational domains of triangular and diamond module and their position.....	124
5.4.2.2 Velocity vector .....	126
5.4.2.3 Drag coefficient on a cylinder.....	128
5.4.2.4 Summation of drag force .....	128
5.4.2.5 Pressure contour and pressure drop.....	129
5.4.3 T-shape and line-shape models.....	132
5.4.3.1 Computational domains of T-shape and line-shape and their positions.....	133
5.4.3.2 Velocity vector .....	135
5.4.2.3 Drag coefficient on a cylinder.....	137
5.4.3.4 Summation of drag force .....	138
5.4.3.5 Pressure contour and pressure drop.....	139
5.4 Summary result .....	142
CHAPTER 6.....	144

CONCLUSION .....	144
APPENDIX.....	147
CONFERENCE PROCEEDING .....	147
1 Introduction .....	1
2 Methodology .....	2
3 Validation .....	3
4 Result .....	5
5 Conclusion .....	2
6 Acknowledgement .....	2
7 Reference .....	2
REFERENCES .....	4
VITA.....	9





## LIST OF TABLES

	Page
Table 1 Dimensionless variables .....	29
Table 2 Reference results.....	69
Table 3 The results from two-dimensional simulations at $Re=100$ .....	71
Table 4 Drag Coefficient ( $C_d$ ), Lift Coefficient ( $C_l$ ) and Strouhal number ( $St$ ) comparison with the literatures.....	73
Table 5 Drag coefficients ( $C_d$ ) of the flow past two side-by-side circular cylinders at various gap width.....	80
Table 6 Lift coefficients ( $C_l$ ) of the flow past two side-by-side circular cylinders at various gap width.....	81
Table 7 Strouhal numbers ( $St$ ) of the flow past two side-by-side circular cylinders at various gap width.....	82
Table 8 Drag coefficient from cylinder in each column.....	92
Table 9 Summary result of arrays of cylinders .....	142

## LIST OF FIGURES

	Page
Figure 1 Sketches and notes of wake flows from Leonardo da Vinci .....	19
Figure 2 first flight of the Wright flyer.....	20
Figure 3 Simulation pictures of fluid flow past vehicle and spaceship.....	21
Figure 4 The first pictures of steam lines, vortices and experimental setup by Ahlborn, F. [2].....	22
Figure 5 Flows behind a circular cylinder: (a) $Re = 40.3$ (photo by Coutanceau and Bouard [6]), (b) $Re = 140$ (photo by M. V. Dyke [7]) .....	22
Figure 6 Bamboo fencing in Thailand.....	24
Figure 7 Blueprint of bamboo fencing designed by DMCR.....	25
Figure 8 Study site of Chachoengsao Province [12].....	25
Figure 9 the breakwater combined with ‘low-crested revetment’ and ‘bamboo fencing’ .....	26
Figure 10 Force from interaction between fluid flow and immersed an object: (a) pressure force, (b) viscous force and (c) resultant forces (lift and drag) [14] .....	31
Figure 11 Pressure and shear forces on a small area of the body surface [14] .....	32
Figure 12 Shape effects on drag coefficient.....	33
Figure 13 (a) Control volume and system for flow through an arbitrary, fixed control volume, (b) Typical control volume with more than one inlet and outlet.....	35
Figure 14 streamtube flow.....	37
Figure 15 Plot of $C_d$ against $\log_{10} Re$ with other researches: $\odot$ = pressure drag from this experiment, x = pressure drag from his previous experiment .....	39

Figure 16 Plot of $\log_{10}C_d$ against $\log_{10}Re$ from 8 kinds of fiber wire with estimated fitted line: x = fiber 1, O = fiber 2, + = fiber 3, $\Delta$ = fiber 4, $\nabla$ = fiber 5, $\diamond$ = fiber 6, $\square$ = fiber 7, Y = fiber 8.....	40
Figure 17 The Strouhal number against Reynolds number for a circular cylinder .....	41
Figure 18 Drag coefficient for time = 0-6 at Reynolds number of 40 and 100.....	42
Figure 19 Drag coefficient with Reynolds number: $\square$ represents Dennis values .....	42
Figure 20 Time-dependent drag & lift coefficient at $Re = 100$ .....	43
Figure 21 Velocity field at $t = 84.60$ .....	44
Figure 22 Pressure, lift, and drag coefficient with time-evolution at $Re = 100$ .....	45
Figure 23 Strouhal number versus range of cylinder gap at 3 points: O = downstream of cylinders, $\Delta = 90^\circ$ of one cylinder, X = gap center-line .....	46
Figure 24 Antiphase (top) and in-phase vortex street forms (bottom) in two colors ..	47
Figure 25 Photographs of flow pattern for side-by-side arrangement.....	48
Figure 26 Drag and lift coefficients with time for the lower cylinder in side-by-side arrangement: (a) $T=1.5$ , (b) $T=3$ .....	49
Figure 27 Drag and lift coefficients for side-by-side cylinders at $Re=100$ : $T=3$ .....	50
Figure 28 The grid of two 'side-by-side' cylinders for $T/D = 1.5$ .....	51
Figure 29 Drag and lift coefficients for side-by-side cylinders at $Re=100$ : $T=3$ .....	52
Figure 30 Outline of large and small cylinders .....	52
Figure 31 Time averaged force coefficients on the large cylinder: (a) drag coefficient, (b) lift coefficient .....	53
Figure 32 Time averaged force coefficients on the small cylinder: (a) drag coefficient, (b) lift coefficient .....	53
Figure 33 Instantaneous vorticity gap range = 0.05 and angle = $\pi/2$ .....	54
Figure 34 Zigzag arrangement of sand fence [31] .....	55

Figure 35 The set of triangular modules of the breakwater [32].....	55
Figure 36 The model of T-shaped bamboo-fencing and its actual placement in the coastal zone of the lower Mekong Delta in Vietnam [33] .....	56
Figure 37 The functions of the three main elements within a CFD analysis framework [34].....	57
Figure 38 2D control volume .....	63
Figure 39 The single cylinder schematic description .....	64
Figure 40 The ‘side-by-side’ arrangement schematic description .....	64
Figure 41 The schematic description of array of cylinders: (a) staggered arrangement, (b) aligned arrangement .....	66
Figure 42 The detail of breakwater made by bamboo designed by DMCR .....	67
Figure 43 Computational domain (left) and near-cylinder mesh (right) for the baseline case.....	67
Figure 44 Drag and lift coefficients.....	69
Figure 45 Drag coefficients ( $C_d$ ) with time-dependence comparison of flow past two side-by-side ( $T = 1.5D$ ) cylinders at $Re = 100$ .....	74
Figure 46 Lift coefficient ( $C_l$ ) with time-dependence comparison of flow past two side-by-side ( $T = 1.5D$ ) cylinders at $Re = 100$ .....	75
Figure 47 Drag coefficient ( $C_d$ ) with time-dependence comparison of flow past two side-by-side ( $T = 3D$ ) cylinders at $Re = 100$ .....	76
Figure 48 Lift coefficient ( $C_l$ ) with time-dependence comparison of flow past two side-by-side ( $T = 3D$ ) cylinders at $Re = 100$ .....	77
Figure 49 Velocity contour: (a) $T/D = 1.5$ , (b) $T/D = 3D$ .....	78
Figure 50 Drag coefficient ( $C_d$ ) with time around 1 <sup>st</sup> and 2 <sup>nd</sup> side-by-side circular cylinders at $Re=100$ .....	83

Figure 51 Lift coefficient ( $C_l$ ) with time around 1 <sup>st</sup> and 2 <sup>nd</sup> side-by-side circular cylinders at $Re=100$ .....	84
Figure 52 Results compared with a single cylinder at $Re=100$ .....	85
Figure 53 Computational domain: (a) full domain, (b) zoom-in, (c) near-cylinder .....	87
Figure 54 Vorticity for 3 columns of array: (a) staggered arrangement (Top) and zoom-in (bottom), (b) aligned arrangement (Top) and zoom-in (bottom).....	88
Figure 55 Vorticity for 4 columns of array: (a) staggered arrangement (Top) and zoom-in (bottom), (b) aligned arrangement (Top) and zoom-in (bottom).....	89
Figure 56 Vorticity for 5 columns of array: (a) staggered arrangement (Top) and zoom-in (bottom), (b) aligned arrangement (Top) and zoom-in (bottom).....	89
Figure 57 Order of columns: (a) staggered arrangement, (b) aligned arrangement .....	90
Figure 58 Time-averaged drag coefficient for each cylinder.....	92
Figure 59 Drag coefficient ( $C_d$ ) with time on cylinders for each column, both arrangement: (a) 3 columns, (b) 4 columns, (c) 5 columns.....	94
Figure 60 Summation of drag force with time.....	95
Figure 61 Time-averaged summation of drag force.....	95
Figure 62 Pressure contour $t= 50.00$ , 3 columns: (a) staggered, (b) aligned .....	97
Figure 63 Pressure contour $t= 50.00$ , 4 columns: (a) staggered, (b) aligned .....	98
Figure 64 Pressure contour at $t= 50.00$ , 5 columns: (a) staggered, (b) aligned.....	99
Figure 65 Pressure contour at $t= 50.00$ with horizontal line $y= -0.5$ .....	100
Figure 66 Pressure at $t= 50.00$ along the horizontal line $y= -0.5$ .....	101
Figure 67 The domain with reference line .....	102
Figure 68 Area-weighted average pressure for 3 columns: staggered arrangement (top), aligned arrangement (bottom).....	103

Figure 69 Area-weighted average pressure for 4 columns: staggered arrangement (top), aligned arrangement (bottom).....	104
Figure 70 Area-weighted average pressure for 5 columns: staggered arrangement (top), aligned arrangement (bottom).....	105
Figure 71 Time-average of area-weighted average pressure.....	106
Figure 72 Pressure drop across the computational domain.....	107
<i>Figure 73 Comparison of energy from pressure drop and drag force .....</i>	<i>109</i>
Figure 74 Comparison of time-average energy from pressure drop and drag force...	110
Figure 75 Drag coefficient for each cylinder for 6 and 8 columns.....	112
<i>Figure 76 Drag coefficient for each cylinder for 10 and 13 columns.....</i>	<i>113</i>
<i>Figure 77 Time-averaged drag coefficient for each cylinder up to 13 columns .....</i>	<i>113</i>
Figure 78 Summation of drag force with time up to 13 columns.....	114
Figure 79 Time-averaged summation of drag force up to 13 columns.....	114
Figure 80 Pressure drop with time up to 13 columns.....	115
Figure 81 Time-averaged pressure drop up to 13 columns .....	115
Figure 82 Zigzag arrangement of sand fence [31].....	116
Figure 83 (a) Computational domain of zigzag arrangement, (b) its position .....	117
Figure 84 Velocity vector of zigzag arrangement: (a) the whole domain, (b) zoom-in .....	118
Figure 85 Streamwise velocity for zigzag arrangement.....	119
Figure 86 Drag coefficient for each cylinder from zigzag arrangement: (a) front position, (b) mid position, (c) back position.....	120
Figure 87 Comparison of summation of drag force.....	121
Figure 88 Pressure contour from zigzag arrangement: (a) the whole domain, (b) front position, (c) back position .....	122

Figure 89 Area-weighted average pressure from zigzag arrangement.....	123
Figure 90 The set of triangular modules of the breakwater [32].....	124
Figure 91 The computational domains: (a) Triangular module, (b) Diamond module .....	125
Figure 92 Vorticity and streamline: (a) Triangular module, (b) Diamond module.....	126
Figure 93 Horizontal velocity: (a) triangular, (b) diamond modules.....	127
Figure 94 Drag coefficients on cylinders from triangular and diamond modules .....	128
Figure 95 Summation of drag force from triangular and diamond modules .....	129
Figure 96 Pressure contour at time = 50.00: (a) the triangular module, (b) the diamond module.....	130
Figure 97 Area-weighted average pressure: (a) the triangular module, (b) the diamond module .....	131
Figure 98 Line-shape breakwater .....	132
Figure 99 The model of T-shaped bamboo-fencing and its actual placement in the coastal zone of the lower Mekong Delta in Vietnam [33] .....	133
Figure 100 The computational domains: (a) T-shape, (b) line-shape .....	134
Figure 101 Velocity vector: (a) T-shape, (b) line-shape.....	135
Figure 102 Horizontal velocity: (a) T-shape, (b) line-shape.....	136
Figure 103 Drag coefficients from both models: (a) top position, (b) mid position....	137
Figure 104 Drag coefficients from tail position .....	138
Figure 105 Summation of drag force from T-shape and line-shape .....	139
Figure 106 Pressure contour at time = 50.00: (a) T-shape, (b) line-shape.....	140
Figure 107 Area-weighted average pressure: (a) T-shape, (b) line-shape .....	141
Figure 108 Summation of drag force vs number of cylinders.....	143

# CHAPTER 1

## INTRODUCTION

### 1.1 Solid object in fluid flows

The flow past objects occurs naturally in universe when fluid (gas or liquid state) runs through and around solid surface. There have many evidences that “Mesopotamia” the earliest human civilization began near the shoreline of rivers. Therefore, the humankind has achieved to employ the knowledge from the phenomenon of fluid dynamics since antiquity, such as the design of drainage channel to avoid flood and water supply for agriculture, sailing ships with oars. Moreover, human used this knowledge to design and develop weapons for hunting like arrows and spears.

Around 285-212 BC, Archimedes, remembered as the famous Greek philosopher and mathematician, was curious to know how he could differentiate gold and silver without color. He just had the fact that silver has less density than gold but no way to prove it. Once, he laid himself to the public bathtub, he noticed water level rose up significantly. Suddenly, he figured out the solution to the problem. With excitement, he jumped off from the tub, ran into streets nakedly and shouted out loud the legendary renowned word “Eureka!”. Archimedes discovered the law of buoyancy, also known as Archimedes’ principle and utilize them to find density of immersed object. This principle blazed a trail to contemporary fluid mechanics and flow past objects.

In Middle Ages, up to the Renaissance, flow around a bluff body is massively surveyed and one of the most concerned problems for experimentalists and theoreticians in fluid mechanics. From a primitive history, Leonardo da Vinci, during



1452 - 1519, might be first-known, observed wake flow due to obstacle such as figure 1.

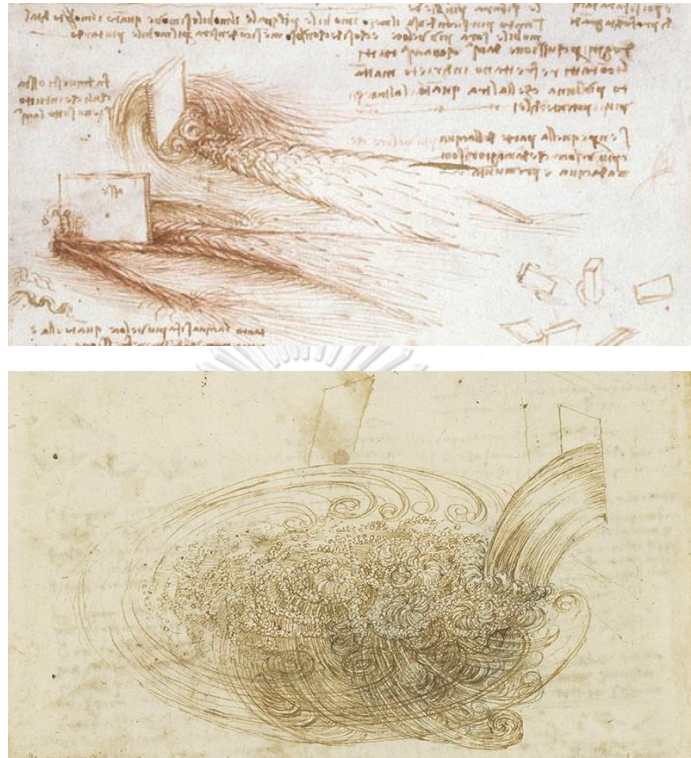


Figure 1 Sketches and notes of wake flows from Leonardo da Vinci

He left the quote 500 years ago which was the earliest importance of vortices and turbulent flow, and it originated the equation of dimensional steady flow that we study at present.

*"Observe the motion of the surface of the water, which resembles that of hair, which has two motions, of which one is caused by the weight of the hair, the other by the direction of the curls; thus the water has eddying motions, one part of which is due to the principal current, the other to the random and reverse motion."*

*"So moving water strives to maintain the course pursuant to the power which occasions it and, if it finds an obstacle in its path, completes the span of the course it has commenced by a circular and revolving movement."*

In nineteenth century, the study of flow past objects began to pick up steam when the Wright brothers, consisted of Orville and Wilbur Wright, invented the first heavier-than-air aircraft operated by motor, also known as “airplane”.

The design of glider without engine was released in 1899. They hypothesized the flow through wing warping with flat surface would generate lift force to his glider and made it float in the air. After that, they used the principle of lift force from flow past the wings and developed drag equation to improve their gliders and eventually, the engine was put to which glider prepared. The full-size flying machine from the Wright brothers was achieved at late morning of 19 December 1903 and it was well-known as the first powered flight in the world. The flight, controlled by Orville Wright, of 120 feet from the ground was flying just 12 seconds at a speed of only 6.8 miles per hour. The photograph of first flight was took within Wilbur Wright running at the wingtip in figure 2.



*Figure 2 first flight of the Wright flyer*

Until now, knowledge of external flows is still very significantly developed in term of aerodynamics such as airplane or spaceship flies through the atmosphere. Even though the flows past objects are literally important to the aerodynamics, there are many other fields that are of equal importance. The resultant forces, lift and drag, on vehicle surface such as formula one, general cars or cargo ship have

become remarkable topic. To correctly design the vehicles, it has become the possibility for reduction of fuel consumption and improvement of the handling characteristics of the vehicles or ships surrounded by two fluid, air and water.

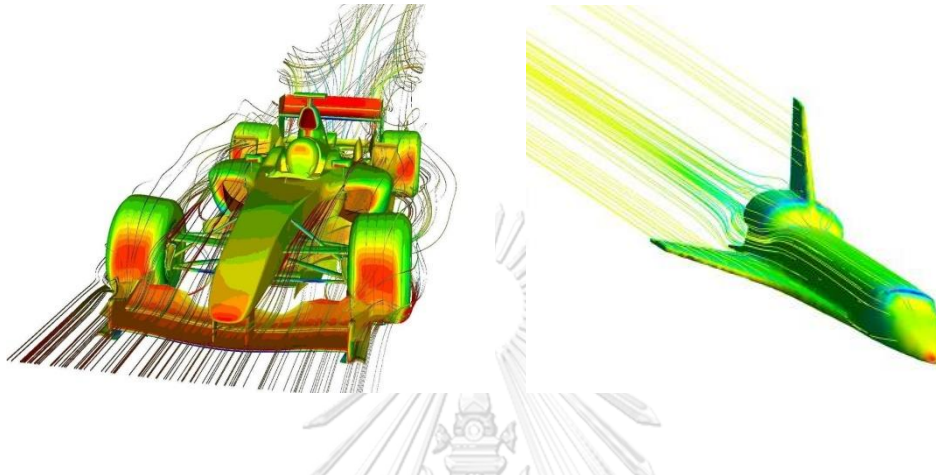


*Figure 3 Simulation pictures of fluid flow past vehicle and spaceship*

## 1.2 The phenomenon of vortex shedding

Vortex shedding is when free stream of fluid with certain velocity tackles to any bluff solid object as opposed to streamline, the flow swirls to the roll that is 'vortex' and then this vortex 'sheds' out of object so we call this consequent behavior as 'vortex shedding'. These vortices shed out along behind the object as a phenomenal path named as 'Kármán-vortex Street'.

During the time of success of the pioneering aviation, study of flow around objects also began systematically. Around the end of the nineteenth century when Vincenc Strouhal had been discovered the effect of vibration in wires due to wind (singing of aeolian tones), moreover Lord Rayleigh [1] soon performed similar experiments and acknowledged the relationship of vibration with wire thickness and wind speed which came to be known as the Strouhal number.

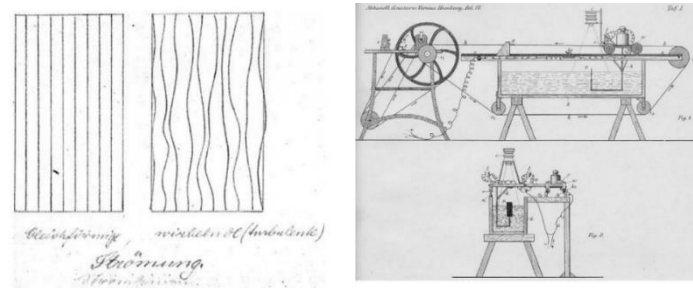


Figure 4 The first pictures of steam lines, vortices and experimental setup by Ahlborn, F. [2]

The first modern picture in figure 4 showing vortices in wake was published by Ahlborn, F. [3] in 1902, after that his pioneer visualizing technique was used extensively. In 1908, Bénard, H. [4] tried to associate this phenomenon with vortex formation then in 1912, Theodor von Kármán published his investigation and the famous theory of the stable, staggered arrangement of vortex street which bear his name, Kármán-vortex street represented this phenomenon, from that time on In addition, Willie [5] claimed that how Theodore von Kármán had been confronting with the problem of treating the alternating and swirling vortices separation, cause by process of vortex shedding, in pattern and linking the theory of Kármán and others were established, a huge number of investigations associated with vortex streets have been progressed rapidly widely spread for further studies.

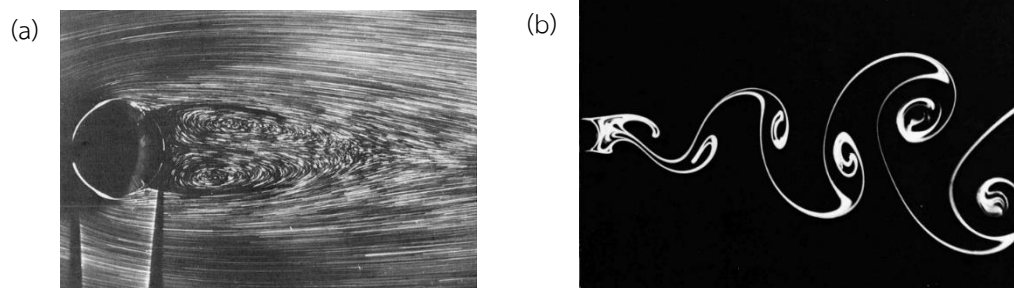


Figure 5 Flows behind a circular cylinder: (a)  $Re = 40.3$  (photo by Coutanceau and Bouard [6]), (b)  $Re = 140$  (photo by M. V. Dyke [7])

As figure 5, the Kármán-vortex street naturally occurs for in fluid flow past a circular cylinder at the Reynolds numbers ranging approximately from 100 to  $10^5$  [8]. Anyway, the formation of characteristic frequency, well-known as Strouhal number (St), meaning of Reynolds number (Re), relationship between Strouhal number and Reynolds number and others resultant values will be discussed in chapter 2 with many reliable previous literatures.

### 1.3 Related problems

The problem we pay attention to is coastal erosion that many muddy shorelines in Thailand have widely confronted this problem for long time. During the past decades, the mangroves near beaches have been disappeared in many areas in order to accommodate increasingly human land-use such as resident, transport infrastructure, agriculture and aquaculture (especially salt pan and shrimp farming). Due to vanishment of the mangroves, muddy coastline around the gulf of Thailand has been attacked seriously and chronically.

There are many solutions to mitigate coastal erosion. One of effective method, called 'soft solution', mainly 'sand beach nourishment', has become repetitive and popular process around Mediterranean coast of Europe. M. Bitan [9] showed the result of sand nourishment that treated more friendly with environment than hard solution, nevertheless, independent variable, such as gain size, gain roughness, volume of sand and length of beach area. Furthermore, durability is still a big question that the project of this paper in Israel after nourishment was poor, with very short time approximately just few months. However, much higher durability rates were shown 5-33% after 6 years in Germany, 80-100% after 10 years in England and 5-15 years in Denmark. This is environmentally friendly method, but on other hand, it requires an in-depth study of each area. the hard solution such as dam construction, is not practical to many area, moreover, it sometimes can aggravate the erosion to other side of littoral zone [9]. In southern of Thailand, especially muddy shoreline, the study of U. Thampanya [10] observed that increment of mangrove



progradation seems like another appropriate soft solution and can sustain mud and sediment of shoreline. The paper indicated that gross erosion was associated with increase of shrimp farm and loss of mangroves. They have obvious evidence the zone of mangroves had been reduced to about 50% then coastal erosion accretion has occurred faster and irregularly along the coastline for few years.

The soft solution that relates to our objective, simulation of flow past multi cylinder is ‘bamboo fencing’, shown in figure 6. This solution has become widespread along to the Gulf of Thailand due to suitability of muddy shoreline and easy installation. The guide of bamboo fencing for solving and preventing coastal erosion problem [11] was released by department of marine and coastal resources (DMCR) which contain the installation method and design of bamboo fencing with space for mangroves shown in figure 7. The guide also revealed that the fencing was provided by DMCR to Chachoengsao, Samutprakarn, Krabi, Samutsakhon and Samutsongkram total 13.665 kilometers and few kilometers by other departments.



*Figure 6 Bamboo fencing in Thailand*

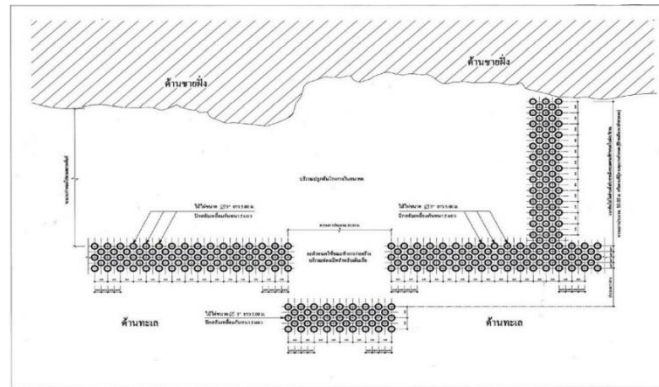


Figure 7 Blueprint of bamboo fencing designed by DMCR

Although bamboo fencing method has become the one of most popular application for the muddy coastal erosion zone, in some area, it confronts with too much wave energy, gust of wind, thunderstorm and stand just for short time. C. Saengsupavanich [12] surveyed coastal erosion by previous 10 years satellite images as figure 8 (capture in 1989-2010) along upper Gulf of Thailand, Chachoengsao province and offered more solutions to deal with the problem. The outcome of low-crested revetment (LCR) combined original solution ‘bamboo fencing’, as shown in figure 9, and this combination was approved by communities’ opinions 83.89%.

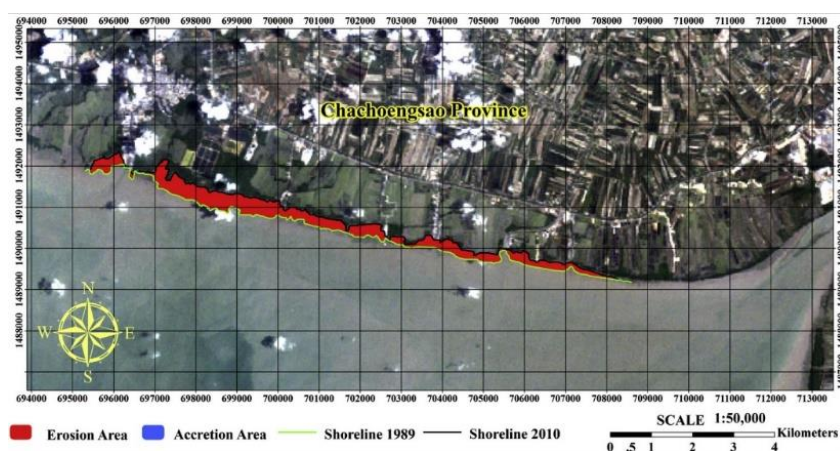


Figure 8 Study site of Chachoengsao Province [12]

From the studies mentioned above, bamboo fencing has become our native coastal protection but the arrangement of them consists by trial or adapting to areas. We purpose to attain the physical dependency about force coefficients, characteristic frequency, and other values to reinforce theoretical information and we hope our study will be useful and helpful to this chronic problem.

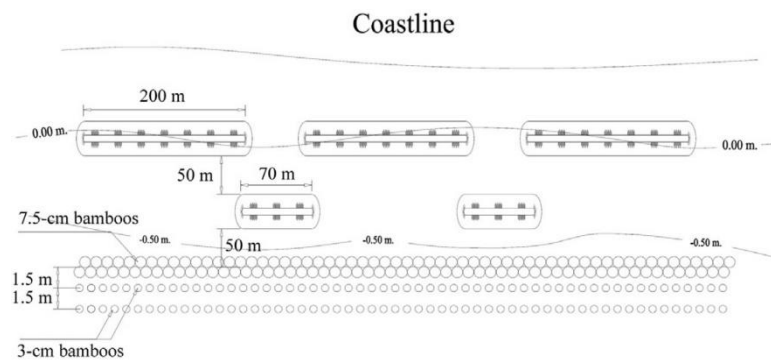


Figure 9 the breakwater combined with 'low-crested revetment' and 'bamboo fencing'

## 1.4 Objective of the research

The objective is to help adding to our understanding of two-dimensional flow past a group of cylinders in various arrangement at low to high Reynolds number. In particular, the properties of flow that are Strouhal number, velocity field, momentum field and kinetic energy behind cylinders will be investigated together with the drag force on the cylinders.

## 1.5 The review of our thesis and scope

Our thesis has consisted with five chapter. We commence our thesis with the brief history of vortex-shedding and related problem in first chapter. The study of flow past a circular cylinder solved by Navier-Stroke equation which has been investigated by many experts for centuries so we chronologize the investigation of near-wake of flow around a circular cylinder and Karman vortex street in next the



part of this chapter and then the variety of related problem researches will be discussed in the last part of the first chapter.

Chapter 2 contains the previous introductory literatures about the flow through a single cylinder, a pair of cylinders and array of cylinders in both experimental and numerical simulation. They presented various kinds of experiment and derivation of resultant values. Moreover, we show grid structure of numerical solutions from those researches that can be our inspired models. In a pair of cylinders part, we further learned the interaction of vortex shedding flow from each other caused by transverse gap in 'side-by-side' arrangement. Nevertheless, flow through array of cylinders, including angular position and pitch of cylinders, are still lacking of investigation that is why we have desire to accomplish this issue.

Chapter 3 presented finite-volume method and numerical solution from ANSYS-Fluent that we used to simulate the incompressible flow. The geometry configurations of cylinders are also shown in this chapter. In 'side-by-side' arrangement, we gradually change the spacing gap between cylinders to see transformation of force coefficient and characteristic frequency. In array of cylinder part, we change both spacing gap and angle between cylinders and record those results.

Chapter 4, we firstly report data from flow around a circular cylinder to validate with other references then, we present the results from a pair of 'side-by-side' cylinders and observe the interference of flow with variable transverse gap. The last part of this chapter, the results from array of cylinder', varied range of pitch and angle of cylinders, are report and analyze change of flow behind them.

Chapter 5, we summary all the result and present the principal conclusion of this research. The crucial benefits and flaws are highlighted. Avenues for future work for future research are advised.

## CHAPTER 2

### RELATED THEORY AND REVIEW OF LITERATURES

#### 2.1 Related theory

##### 2.1.1 Governing equations

For long time ago, humans have made a lot of effort to predict behavior of fluid flow. At present time, we usually apply Newton's viscosity law that the viscous stress of fluid flow is a linear function with strain rate at every point [13]. Newtonian fluid actually does not perfectly suit to real fluid however, we use this theory with the Navier-Stokes equations to approximately calculate flow of incompressible viscous fluid from the numerical domain to one another. In our study, the Navier-Stokes equations in 2 dimensions with absence of external force and heat transfer are obtained with conversation of mass and momentum defined as:

Continuity equation:

$$\frac{\partial u}{\partial x} + \frac{\partial v}{\partial y} = 0 \quad (1)$$

Momentum equations:

x-direction:

$$\rho \left( \frac{\partial u}{\partial t} + \frac{\partial(u^2)}{\partial x} + \frac{\partial(uv)}{\partial y} \right) = -\frac{\partial p}{\partial x} + \mu \left( \frac{\partial^2 u}{\partial x^2} + \frac{\partial^2 u}{\partial y^2} \right) \quad (2)$$

y-direction:

$$\rho \left( \frac{\partial v}{\partial t} + \frac{\partial(uv)}{\partial x} + \frac{\partial(v^2)}{\partial y} \right) = -\frac{\partial p}{\partial y} + \mu \left( \frac{\partial^2 v}{\partial x^2} + \frac{\partial^2 v}{\partial y^2} \right) \quad (3)$$

where  $u$  is a velocity component in x-direction (m/s)

$v$  is a velocity component in y-direction (m/s)

$\rho$  is density of fluid (kg/m<sup>3</sup>)

$\mu$  is dynamic viscosity (N·s/m<sup>2</sup>)

$p$  is fluid pressure (Pa)

$t$  is time (s)

### 2.1.2 Non-dimensionalization of the Navier-Stokes equation

The conversion of the Navier-Stokes equation to nondimensional form is a method that can normalize the scale size to dimensionless parameters. The Navier-Stokes equations from equation (2) and (3) that we presented above can be shortly rewritten as:

$$\frac{\partial \mathbf{v}}{\partial t} + (\mathbf{v} \cdot \nabla) \mathbf{v} = -\frac{1}{\rho} \nabla p + \mu (\nabla^2 \mathbf{v}) \quad (4)$$

where  $\mathbf{v}$  represents components of velocity  $u$  and  $v$  from equation (2) and (3)

$\nabla$  represents the del operator

The Navier-Stoke equation in short form can be non-dimensionalized by the dimensionless variables as:

Table 1 Dimensionless variables

Scale	Dimensionless variable
Length: $D$	Dimensionless length: $D^* = \frac{L}{D}$
Velocity of flow: $U_\infty$	Dimensionless velocity: $\mathbf{v}^* = \frac{\mathbf{v}}{U_\infty}$
Time: $\frac{D}{U_\infty}$	Dimensionless time: $t^* = t / \frac{D}{U_\infty}$
Pressure: $p$	Dimensionless pressure: $p^* = \frac{p}{\rho U_\infty^2}$

So, the non-dimensional form of the Navier-Stokes equation is:

$$\frac{\partial \mathbf{v}^*}{\partial t^*} + (\mathbf{v}^* \cdot \nabla) \mathbf{v}^* = -\nabla p^* + \frac{1}{Re} (\nabla^2 \mathbf{v}^*) \quad (5)$$

### 2.1.3 Reynolds number

The Reynolds number ( $Re$ ), named after the famous physician, Osborne Reynolds, is one of the most used dimensionless number in fluid dynamic, defined as:

$$Re = \frac{\rho U_{\infty} D}{\mu} \quad (6)$$

where  $U_{\infty}$  is characteristic velocity (m/s)

$D$  is characteristic length (m)

The Reynolds number is obtained for numerical calculation for moving particle or immersed objects in real world for examples, the Reynolds number about  $10^{-6}$  for very small organism like bacteria,  $10^6$  for a car at 30 mph or  $10^9$  for a large cruise ship that the fluid flows change from a laminar boundary layer to a turbulent boundary layer at a critical value of the Reynolds number on the order of  $2 \times 10^5$  to  $3 \times 10^6$  depending on roughness of the surface and the number of turbulence in the flow [14]. It is quite clear the fluid flows in surrounding for human life are mostly in turbulent form but nowadays, human still cannot literally calculate turbulent flow precisely.

### 2.1.4 Force coefficient

Due to interaction between an immersed object and fluid, the force can be induced that the fluid flow runs past a stationary object and the object moves through the still fluid with the velocity  $U_{\infty}$  then the force can be separated into pressure force and viscous force in figure 10. However, we only mimic in case of the constant velocity  $U_{\infty}$  past a stationary circular cylinder in our study to compare the results with other references. It can be described in term of the stresses that shear wall stress  $\tau_w$  is caused by viscous force effect as figure 10 (a) and normal stress is caused by pressure force ( $p$ ) as Figure 10 (b). The resultant force is distributed to term the of upstream velocity direction, known as drag force and the term of normal

to the upstream velocity, known as lift force, as shown in figure 10 (c). Both resultant forces can be obtained by integration from shear stress and pressure distribution on object surface.

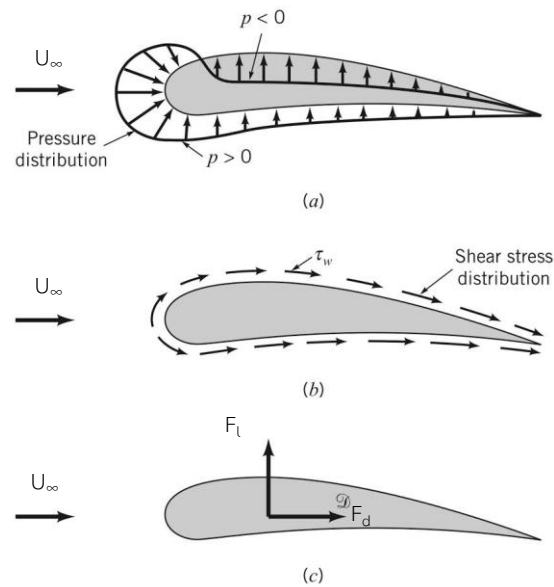


Figure 10 Force from interaction between fluid flow and immersed an object: (a) pressure force, (b) viscous force and (c) resultant forces (lift and drag) [14]

According to [14], the x and y components of the resultant forces on area of surface are

$$F_d = \int p \cos \theta dA + \int \tau_w \sin \theta dA \quad (7)$$

$$F_l = -\int p \sin \theta dA + \int \tau_w \cos \theta dA \quad (8)$$

where  $F_d$  is drag force (N)

$F_l$  is lift force (N)

$\tau_w$  is wall shear stress (N/m<sup>2</sup>)

$\theta$  is an angular location along the object

$dA$  is a small area of the object

The variables from equation (7) and (8) are depicted in figure 11.

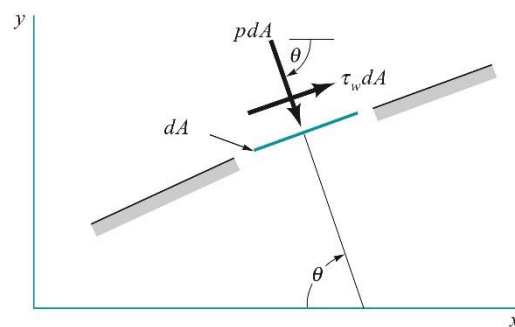


Figure 11 Pressure and shear forces on a small area of the body surface [14]

The two-dimensional resultant forces from shear stress and pressure divided to be in each direction are not dimensionless unit. The dimensionless counterparts of drag and lift forces are called drag coefficient and lift coefficient, defined as:

$$C_d = \frac{F_d}{\frac{1}{2} \rho U_\infty^2 A} \quad (9)$$

$$C_l = \frac{F_l}{\frac{1}{2} \rho U_\infty^2 A} \quad (10)$$

Where  $C_d$  is drag coefficient

$C_l$  is lift coefficient

$A$  is a frontal, projected area of the object (m<sup>2</sup>)

Characteristic area or frontal area of the object, that means the area is projected toward the object from a direction parallel to the upstream velocity  $U_\infty$ . the example of frontal area is depicted in figure 12. From  $C_d$  in the picture, obviously, shape has a significant effect on amount of drag produced even if they have the same frontal area.

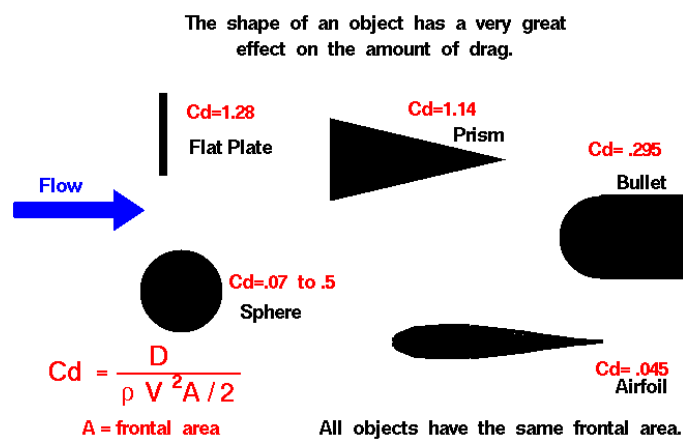


Figure 12 Shape effects on drag coefficient

### 2.1.5 Strouhal number

The Strouhal number is a dimensionless number which relates to the characteristic frequency in unsteady oscillating flow. It is defined as equation

$$St = \frac{f_s l}{U_\infty} \quad (11)$$

where  $St$  is the Strouhal number

$f_s$  is oscillating frequency of flow (Hz or 1/s)

$l$  is the characteristic length scale of the body (m)

The Strouhal number represents the ratio of inertial forces from unsteady flow to another internal forces due to changes in velocity from point to point in the

fluid flow field. This parameter is very important for development of flow past an immersed body that induces the system of vortices, known as Karman vortex stress which we introduced in first chapter.

## 2.1.6 Relating drag force and pressure with energy equation

### 2.1.6.1 Energy equation: First law of thermodynamics

The first law of thermodynamics represents the law of conversation of energy, distinguishing two kinds of energy transfer, as heat transfer and work. It can be formulated to the symbolical equation form as:

$$\frac{D}{Dt} \int_{sys} e \rho dV = \dot{Q}_{net} + \dot{W}_{net} \quad (4)$$

where

$e$  is the total stored energy per unit mass (kJ/K·kg)

$t$  is time (s)

$dV$  is unit volume of system (m<sup>3</sup>)

$\rho$  is density of fluid (kg/m<sup>3</sup>)

$\dot{Q}_{net}$  is time rate of additional energy by heat transfer into the system (kJ/K)

$\dot{W}_{net}$  is time rate of additional energy by work transfer into the system (kJ/K)



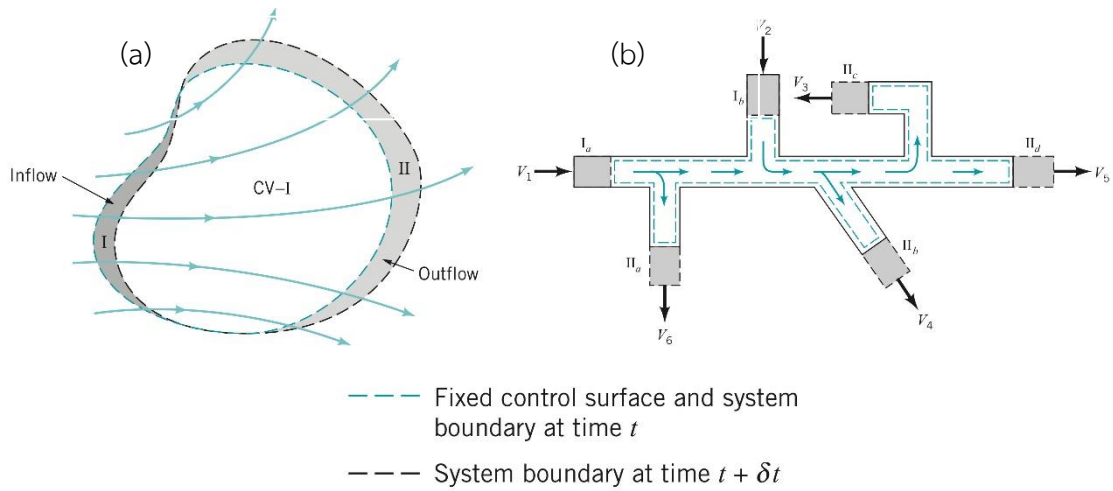


Figure 13 (a) Control volume and system for flow through an arbitrary, fixed control volume, (b) Typical control volume with more than one inlet and outlet

For the fixed and nondeforming control volume with inflow and outflow, the Reynolds number transport theorem is applied to the term of stored energy of system that can be written as:

$$\frac{D}{Dt} \int_{sys} e \rho dV = \frac{\partial}{\partial t} \int_{cv} e \rho dV + \int_{cs} e \rho \mathbf{v} \cdot \mathbf{n} dA \quad (5)$$

Where  $\mathbf{v} \cdot \mathbf{n}$  is component of fluid particle velocity normal to the area element  $dA$

In our study, we only observe the fluid flow in the condition of steady state, therefore, the term of  $\frac{\partial}{\partial t} \int_{cv} e \rho dV$  which represents the time rate change of the total stored energy of contents of control volume is zero. Then the equation of energy can be written as:

$$\int_{cs} e \rho \mathbf{v} \cdot \mathbf{n} dA = \dot{Q}_{net} + \dot{W}_{net} \quad (6)$$

The variable of the total stored energy per unit mass for each particle,  $e$ , can be written as equation as:

$$e = \tilde{u} + \frac{v^2}{2} + gz \quad (7)$$

where  $\tilde{u}$  is the internal energy per unit mass

$\frac{v^2}{2}$  is the kinetic energy per unit mass

$gz$  is the potential energy per unit mass

Hence, the energy equation become:

$$\int_{cs} (\tilde{u} + \frac{v^2}{2} + gz) \rho \mathbf{v} \cdot \mathbf{n} dA = \dot{Q}_{net} + \dot{W}_{net} \quad (8)$$

In the part of work transfer, it contains with internal and external work that we can split to:

$$\dot{W}_{net} = \dot{W}_{int} + \dot{W}_{ext} \quad (9)$$

The internal work,  $\dot{W}_{int}$  can be expressed as the product of local normal stress,  $\sigma = -p$ , and the fluid particle surface area,  $\mathbf{n} dA$ , the result is:

$$\dot{W}_{int} = \int_{cs} \sigma \mathbf{v} \cdot \mathbf{n} dA = \int_{cs} -p \mathbf{v} \cdot \mathbf{n} dA \quad (18)$$

Hence, we can rewrite the energy equation from equation (16) as in the following equation. For clarification, for a situation of flow past a body, the interaction between the body and fluid is counted toward 'external work' in the following equation that could take away or add energy to the fluid as:

$$\int_{cs} (\tilde{u} + \frac{p}{\rho} + \frac{v^2}{2} + gz) \rho \mathbf{v} \cdot \mathbf{n} dA = \dot{Q}_{net} + \dot{W}_{ext} \quad (19)$$

### 2.1.6.2 Application of the energy equation with the Bernoulli Equation

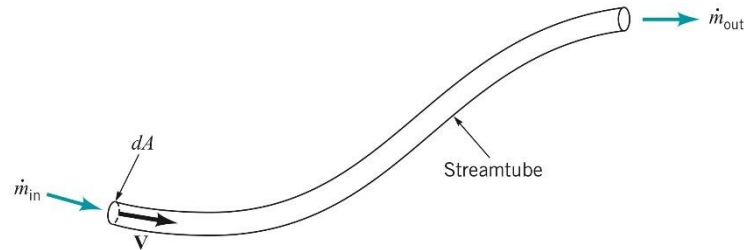


Figure 14 streamtube flow

We apply Bernoulli Equation to the energy equation explained above that the flow are considered as steady and incompressible flow. In our study, there is only one stream entering and leaving the control volume and all properties,  $\tilde{u}$ ,  $p/\rho$ ,  $v^2/2$ , and  $gz$ , are all assumed to be uniformly distributed over the flow cross-sectional areas involved, the integration becomes simple as:

$$\int_{cs} \left( \tilde{u} + \frac{p}{\rho} + \frac{v^2}{2} + gz \right) \rho \mathbf{v} \cdot \mathbf{n} dA = \left( \tilde{u} + \frac{p}{\rho} + \frac{v^2}{2} + gz \right)_{out} \dot{m}_{out} - \left( \tilde{u} + \frac{p}{\rho} + \frac{v^2}{2} + gz \right)_{in} \dot{m}_{in} \quad (20)$$

Uniform flow can be shortly described that will occur in an infinitely small diameter stream tube as illustrated in figure 14. This kind of streamtube flow is ideally representative of the steady flow of a particle of fluid along a path line so the mass flow rate,  $\dot{m}$ , of entering and leaving is the same.

So, we get the energy equation as:

$$\left[ \tilde{u}_{out} - \tilde{u}_{in} + \left( \frac{p}{\rho} \right)_{out} - \left( \frac{p}{\rho} \right)_{in} + \frac{v_{out}^2 - v_{in}^2}{2} + g(z_{out} - z_{in}) \right] \dot{m} = \dot{Q}_{net} + \dot{W}_{ext} \quad (21)$$

Dividing equation (21) by mass flow rate,  $\dot{m}$ , and rearranging term then we obtain:

$$\frac{p_{out}}{\rho} + \frac{v_{out}^2}{2} + gz_{out} = \frac{p_{in}}{\rho} + \frac{v_{in}^2}{2} + gz_{in} - (\tilde{u}_{out} - \tilde{u}_{in} - \dot{q}_{net}) + \dot{w}_{ext} \quad (22)$$

Due to the fact that the attention of our thesis remark upon the flow past array of cylinders simulating breakwater made of bamboo-fencing, the term of heat transfer,  $\tilde{u}_{out} - \tilde{u}_{in} - \dot{q}$ , would be neglected. Therefore, the suitable equation adapted from energy equation, the first law of thermodynamics, and Bernoulli equation is:

$$\frac{p_{out}}{\rho} + \frac{v_{out}^2}{2} + gz_{out} = \frac{p_{in}}{\rho} + \frac{v_{in}^2}{2} + gz_{in} + \dot{w}_{ext} \quad (23)$$

## 2.2 Review of literatures

### 2.2.1 Flow past a circular cylinder

#### 2.2.1.1 Experiment

Since the systematic investigation of vortex-shedding's frequency was kicked off by Vincenc Strouhal and Lord Rayleigh in around the nineteenth century, the flow around bluff body, especially circular cylinders, have been studied and accumulated extensively. Therefore, there have a lot of reliable exiting literatures. We commence the survey with studies of flow past a stationary circular cylinder with both experimental and simulating method. Then the works of more-than-one cylinders will be reviewed later.

The first review throw back to 1933 with the seminal work of A. Thom, "The flow past cylinder at low speeds" [15]. In this study, the drag coefficient was obtained with 5x5 inches tank used with various diameter cylinders consisting and measurement of Chattock gauge. The experiment is set up with basic definitions and the results contains coefficient of pressure drag comparing with skin friction drag line and total drag from other researchers for Reynolds numbers from 3.5 to 240. The plots of pressure drag with fit line against Reynolds number from [15] and other researches are shown in figure 15.

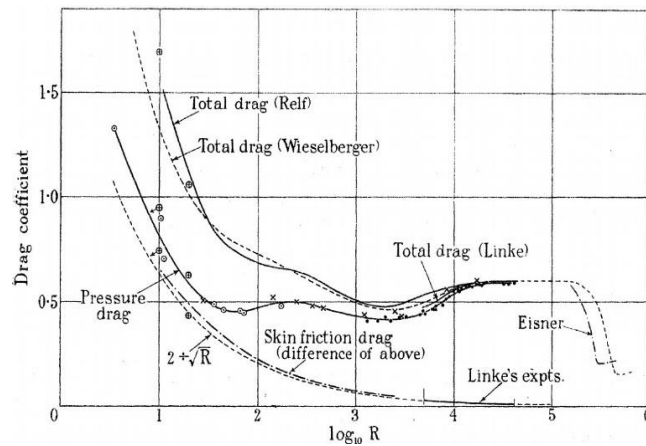


Figure 15 Plot of  $C_d$  against  $\log_{10} Re$  with other researches:  $\circ$  = pressure drag from this experiment,  $\times$  = pressure drag from his previous experiment

D. J. Tritton [16] primally described the measurement of drag coefficient by observing the bending of quartz fiber by stream flow at Reynolds numbers between 0.5-100. The formation is defined as:

$$h = \frac{8Fl^4}{\pi E d^4} \quad (24)$$

where

$F$  is force per unit length normal to its axis

$h$  is the extending length of the fibers

$l$  is the original length of the fibers

$d$  is the diameter of the fibers

$E$  is the Young's modulus of the fibers

The researcher defined drag coefficient, similar with equation (9), as:

$$C_d = \frac{F}{\frac{1}{2} \rho U_\infty^2 d} \quad (25)$$

Therefore, he combined equation (24) and (25) to the equation as:

$$C_d = \frac{\pi E d^3}{4 \rho U_\infty^2 l^4} \quad (26)$$

He spent 8 fiber wires with different property such as Young's modulus, length and diameter for various speeds of velocity to vary the Reynolds numbers. The result of drag coefficient from Thom's study are shown in figure 16 with the fit line created.

Even though, this study was very reliable and it have been referred until now, in this experiment, the researcher criticized that the diameter of fibers sometimes induced some trouble but the result was still satisfied. The error was estimated just 6%. The internal accuracy of point, however, much better (around 2%) and it had very close tendency compare with other sites.

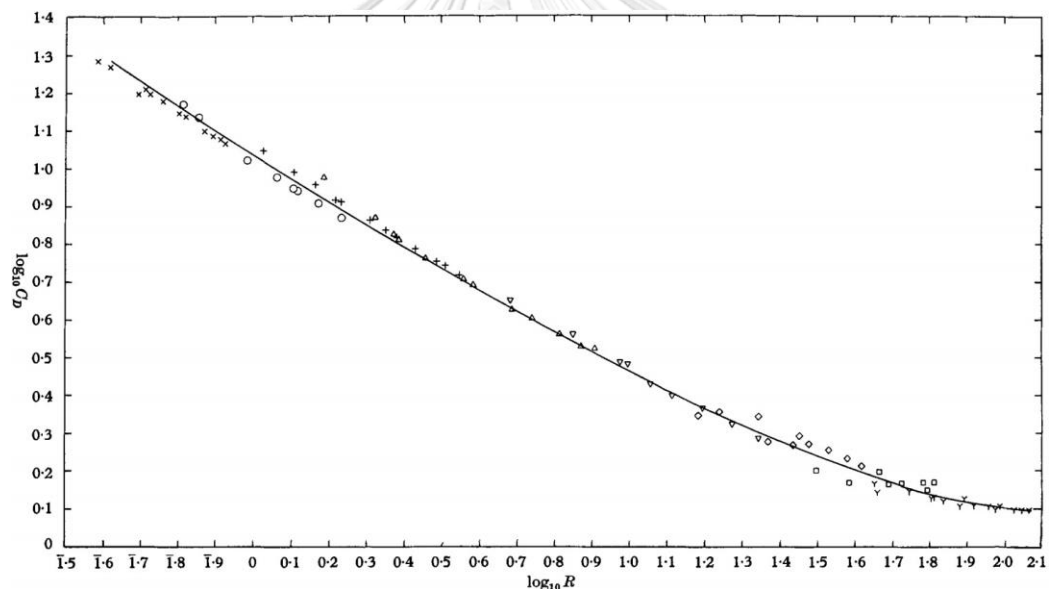
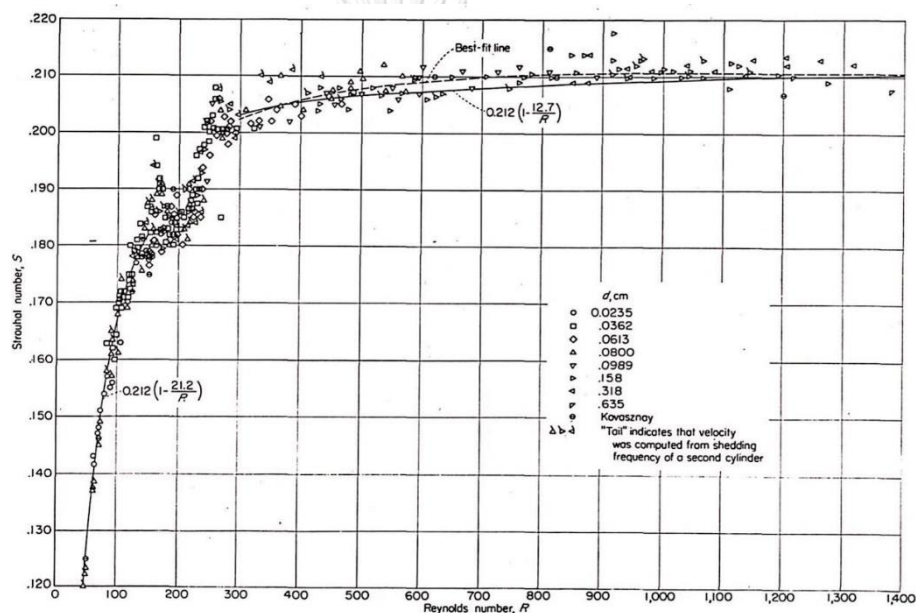


Figure 16 Plot of  $\log_{10}C_d$  against  $\log_{10}Re$  from 8 kinds of fiber wire with estimated fitted line:  $x$  = fiber 1,  $O$  = fiber 2,  $+$  = fiber 3,  $\Delta$  = fiber 4,  $\nabla$  = fiber 5,  $\diamond$  = fiber 6,  $\square$  = fiber 7,  $Y$  = fiber 8

A. Roshko [17] told us about wake development behind circular cylinder at Reynolds numbers from 40 to 10,000 and relationship between the Reynolds numbers and Strouhal number. He provided wind tunnel GALCIT 20-by-20-inch low-

turbulence tunnel with 0.0235 to 0.635 centimeters hot wire for variables of cylinder diameter. This investigation told us about the relationship between Strouhal number and Reynolds number. As known as the shedding frequency is expressed in terms of the non-dimension the Strouhal number as equation (11). The experiment's fit line of Strouhal number and Reynolds number had been plotted very close to the formation as  $St = 0.212 \left(1 - \frac{12.7}{Re}\right)$ , shown as figure 17.



CHULALONGKORN UNIVERSITY

Figure 17 The Strouhal number against Reynolds number for a circular cylinder

### 2.2.1.2 Numerical simulation

Study of Payne [18] is among the first study of numerical calculation for flow of a viscous fluid past a circular cylinder that Helmholtz's vorticity equation was used for Reynolds number 40 (from [19]) and 100 at small intervals of time ( $\Delta t = 0.1$ ). Drag coefficient around the cylinder was obtained for time = 0 – 6, shown as figure 18.

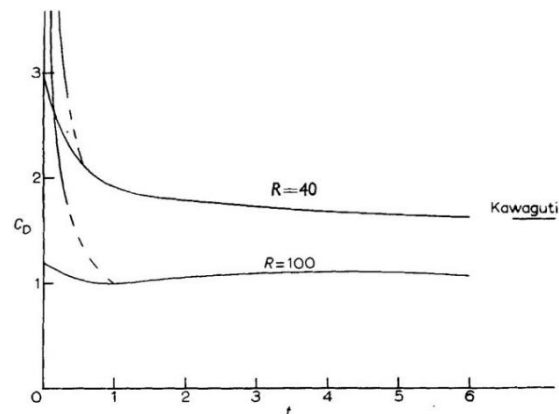


Figure 18 Drag coefficient for time = 0-6 at Reynolds number of 40 and 100

Afterwards, in 1970, S. C. R. Dennis et al.'s work [20] is the modified polar coordinates numerical solutions for two-dimensional flow past a circular cylinder. He applied finite-difference solutions of the equations of motion for steady incompressible to obtain incompressible flow around a stationary circular cylinder which obtained for Reynolds number of 5, 7, 10, 20, 40, 70 and 100. The values of drag coefficient the cylinder surface are solved and shown in figure 19.

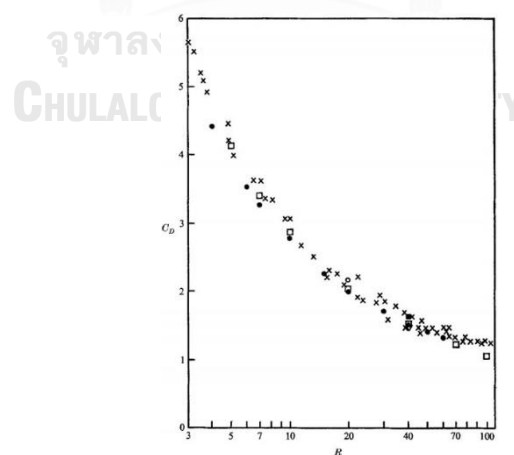


Figure 19 Drag coefficient with Reynolds number:  $\square$  represents Dennis values



Although, the numerical solution of S. C. R. Dennis et al. [20] and Payne [18] caught our eyes, the results of drag coefficient, especially average of  $C_d = 1.172$  from [20], did not get good agreement with data from recent researches probably due to obsolete technical application.

Later, the finite-volume velocity-pressure form of polar co-ordinates unsteady Navier-stokes equation for two-dimensional numerical simulation is applied to study of M. Braza et al. [21] to clarify the initiation of vortex shedding and the interactions of the near-wake was studied and analyzed for Reynolds numbers of 20, 40, 100, 200 and 1000. They claimed that the separation of the vortices, well-known as Karman vortex streets, initially exits at Reynolds number greater than 40. This paper impresses us that the drag, lift coefficient and the Strouhal number at  $Re = 100$  for a single cylinder were  $1.364, \pm 0.250$  and  $1.60$ . The coincidence between these values and other results, both experimental and numerical method, were very good. Furthermore, this study was among of first that shown the time-dependent evolution of the life and drag coefficient at Reynolds numbers of 100 (figure 20) which are similar to our study.

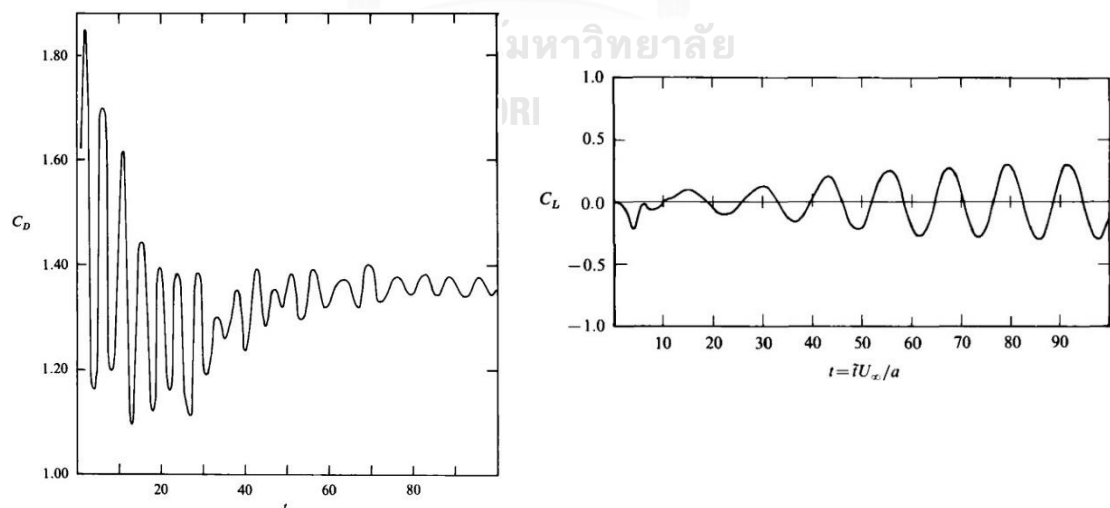
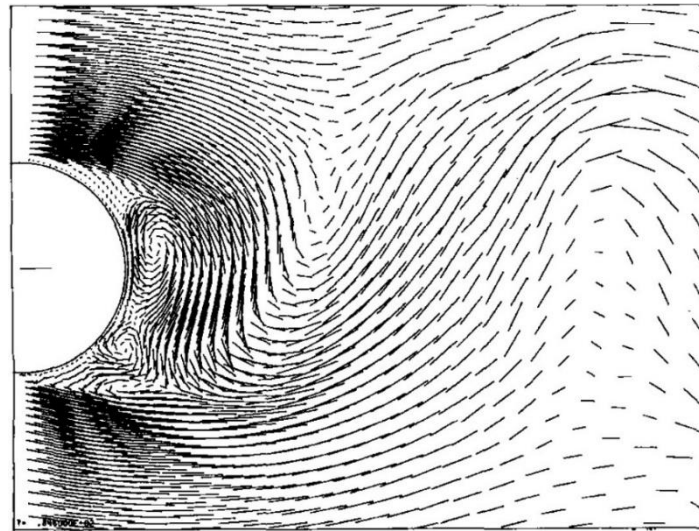


Figure 20 Time-dependent drag & lift coefficient at  $Re = 100$

In addition, flow pattern contour and velocity field from numerical simulation of [21] at time = 80 to 89 were presented in this paper as well, example is shown in figure 21



*Figure 21 Velocity field at  $t = 84.60$*

The objective of C. Liu et al.'s paper [22] is similar to work of M. Braza et al. [21] but with different solution. They obtained the incompressible Reynolds-averaged Navier–Stokes (RANS) equations which is a more modern method that has been used for around four decades to simulate flow around immersed objects. Force and self-excited time-dependent behavior of force are considered in this study. they firstly studied grid refinement for Reynolds number of 150 with  $10^{-6}$  residual of continuity. Then, the investigated drag coefficient, lift coefficient and Strouhal number (vortex shedding frequency) at Reynolds number of 200 were compared with other researches both numerical simulation and experimental data and the results got good agreements with those. After that, time-evolution of drag, lift and base-pressure coefficient were analyzed at Reynolds numbers of 100, 150 and 200, example shown in figure 22. We are very interested with their following procedure that they

commenced with grid study and comparison of resultant values with available data for validation therefore, the main purpose would proceed.

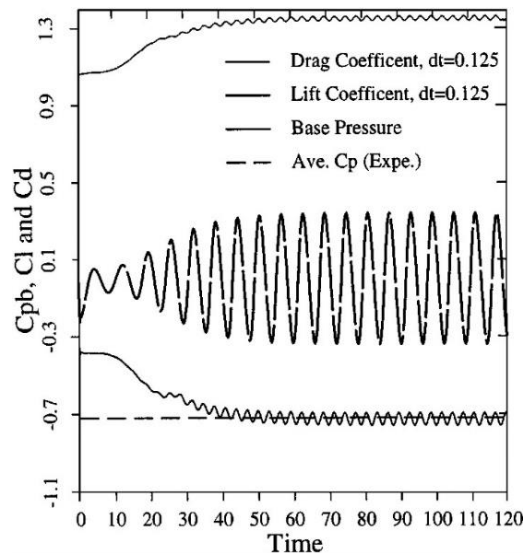


Figure 22 Pressure, lift, and drag coefficient with time-evolution at  $Re = 100$

## 2.2.2 Flow past a pair of cylinders

### 2.2.2.1 Experiment

There are infinite types of possible geometrical configuration of two cylinders for the approaching incompressible flow. For the most arrangement, two groups can be mainly identified; first group, one-cylinder places in front of another at any longitudinal transverse spacing arrangement called 'tandem arrangement'. Second group, both cylinders are placed 'side-by-side' at vertical direction facing the flow at any transverse gap length. Following this information, we would like to pay attention to 'side-by-side' group to observe interference to resultant values, such as drag coefficient, lift coefficient and Strouhal number, between cylinders. There are a lot of published data that studied about the range of intermittent changes of drag and lift force. We are going to present survey of the previous existing literatures in next paragraph.

P. W. Bearman et al.'s paper [23] is one of classical analysis of flow past two cylinders in side-by-side arrangement by experiment with hot wires in tunnel. At that time, flow around two circular cylinders was quite complicated to find out general conclusions about the individual drag and lift force and their interference between cylinders for the range of gap sizes. The investigation of a pair of cylinders was carried out of Reynolds number of  $2.5 \times 10^4$ . Velocity fluctuations in the area around the cylinder pair were detected with Disa constant-temperature hot-wire anemometers and correlation for 3 points in experiment then the results of the Strouhal numbers with range of cylinder gap are plotted in figure 23 (the range of gap in this study addresses from edge to another edge of cylinders).

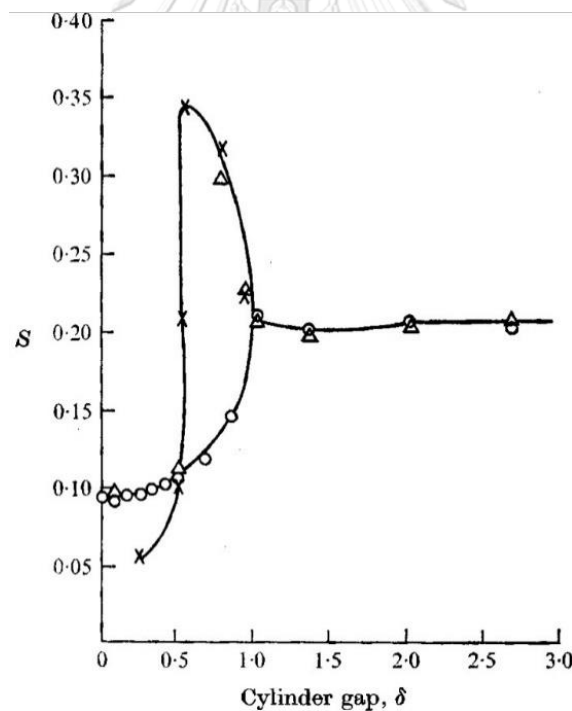
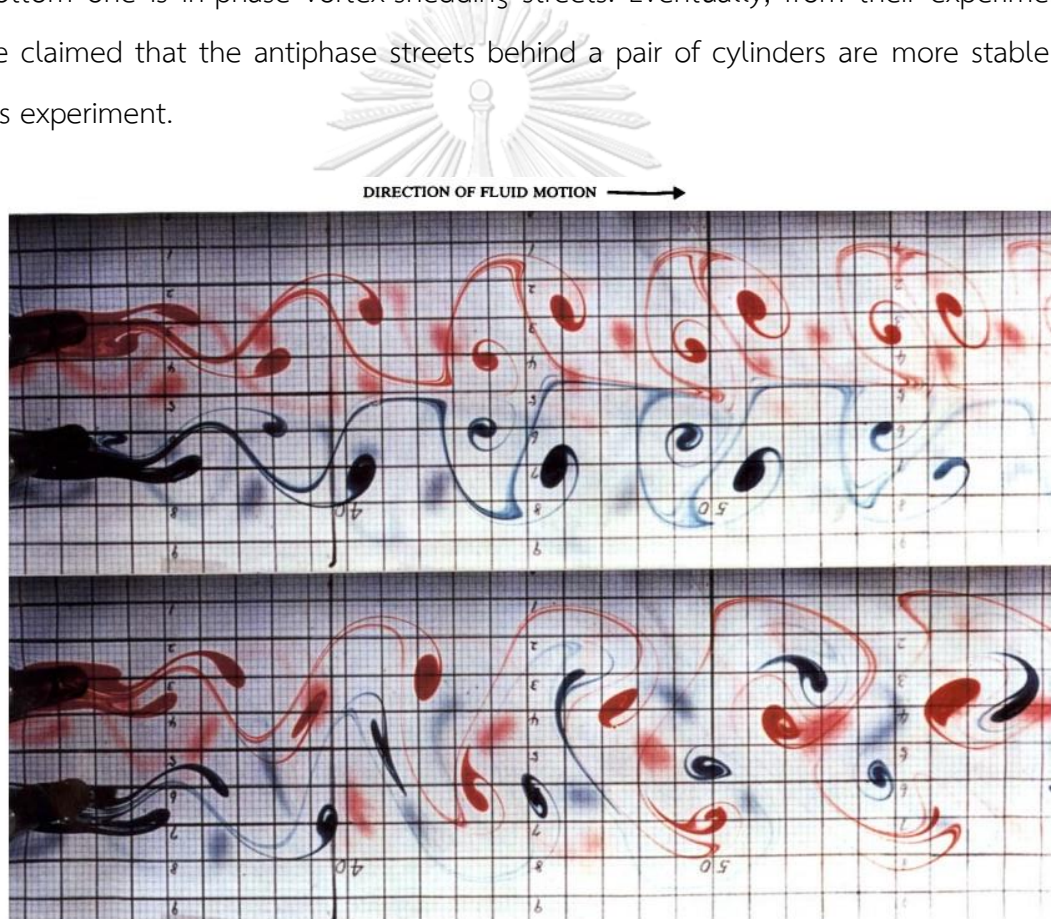


Figure 23 Strouhal number versus range of cylinder gap at 3 points: O = downstream of cylinders,  $\Delta = 90^\circ$  of one cylinder, X = gap center-line

C. H. K. Williamson [24] studied the flow behind a pair of cylinder placed side-by-side in a streamline and gap between cylinder was varied and investigated similarly as P. W. Bearman et al.'s study [23]. However, the remarkable point from this paper is various flow visualizations which could envision pictures of in-phase and antiphase vortex streets apparently at Reynolds number of 200. Another clear demonstrate of wakes from two cylinders is shown in figure 24 that red and blue colors distinguished vortices behind each cylinder. The top picture is antiphase, the bottom one is in-phase vortex-shedding streets. Eventually, from their experiment, he claimed that the antiphase streets behind a pair of cylinders are more stable in his experiment.



*Figure 24 Antiphase (top) and in-phase vortex street forms (bottom) in two colors*

The majority of M. M. Zdravkovich's paper [25] is to review researches of flow interference between two cylinders in various positions of both 'side-by-side' and 'tandem' arrangements. It might be the most comprehensive compiling experiments at high Reynolds numbers of this issue from large numbers of researchers. This experimental report mentioned the 'side-by-side' transverse gap between  $1.1 < T/D < 2.2$  is identified in intermediate critical gap or called 'uncoupled' that in this gap length, the flow is obviously deflected upwards and the frequency of time-dependent drag and lift coefficient do not seem bistable and periodic because of interference between both cylinders. In addition of high Reynolds numbers from work of S. Ishigai et al. [26], for  $H/D \geq 2$ , the process of vortex information of both cylinders is totally the same and the flow becomes the unsteady bulk for smaller  $H/D$  as in figure 25 (where  $H$  represents transverse gap in this work of S. Ishigai et al. [26]).

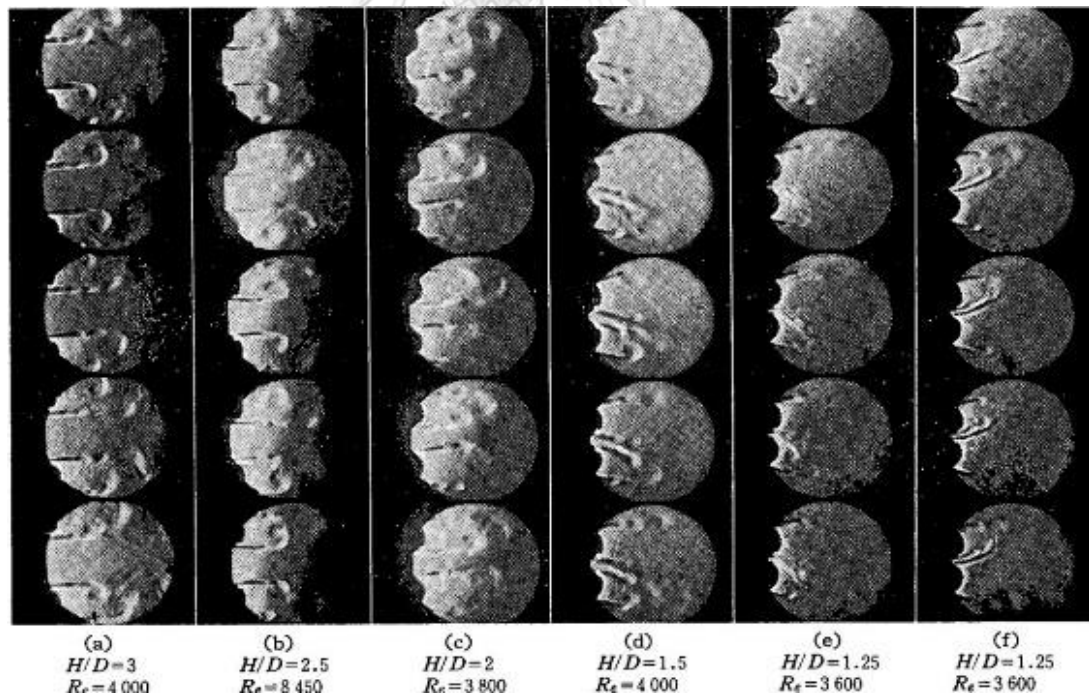


Figure 25 Photographs of flow pattern for side-by-side arrangement

### 2.2.2.2 Numerical simulation

There had been few numerical simulation of flow around two cylinders at that time so the A. Slaouti et al.'s paper [27] was among of first simulating studies about this topic. They used the random-vortex model to mock-up and investigate the two-dimensional flow around a pair of cylinders in 'tandem' and 'side-by-side' arrangements. This research advised us for the way to our solution to define significant results especially 'side-by-side' type. 0.1 time step was applied for the results of drag coefficient, lift coefficient and Strouhal number at only Reynolds number of 200. The range of transverse gaps (T/D) was set up for 1.1, 1.5, 3.0 and 4.0 to find out the variable results. The streamlines of near-wake for both cylinders also were presented at specific time then we could see the interaction of flow behind them. Another important results due to the range of spacing gap, drag and lift coefficient with time-independence of adjacent cylinders were shown for T/D = 1.1, 1.5 and 3, shown in figure 26, that we could see their behavior from beginning of time.

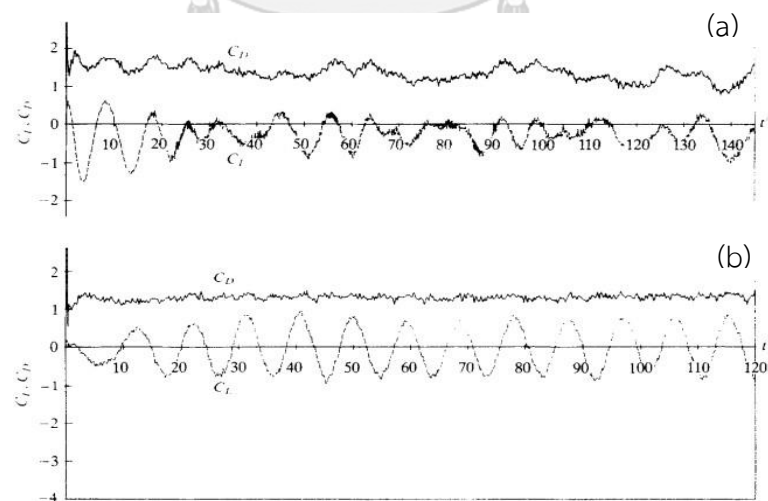


Figure 26 Drag and lift coefficients with time for the lower cylinder in side-by-side arrangement: (a)  $T=1.5$ , (b)  $T=3$

Despite drag and lift coefficients with time-dependence plotted, the drawbacks of this simulation are the fluctuation which deflected to the whole plots, moreover, in some points of the graphs, they seem not periodically stable. Another drawback is the drag and lift coefficient were shown for only lower cylinder which is incomplete information.

H. Ding et al.'s study [28] was very similar to previous one but more up-to-date simulating method. The mesh-free least square-based finite difference, called MLSFD, was applied for the simulation flow through 'tandem' and 'side-by-side' arrangement of a pair of cylinders as well as A. Slaouti et al.'s paper [27] but they carried out in two Reynolds numbers, that is  $Re = 100$  and  $200$  respectively. They claimed that mesh-free or MLSFD method not only fixes mesh-relate drawbacks but it also processes more flexibly and makes the procedure of node generation more easily. As the results from this method, the flow values of an isolated circular cylinder, consisted of the Strouhal number, mean value and amplitude of drag and lift coefficients, were listed with values achieved by other researchers for comparison and their results agreed excellently with those. Furthermore, the drag and lift coefficients with time-dependence on a single cylinder and a pair of cylinders for Reynolds numbers of  $100$  and  $200$  were demonstrated fairer and clearer periodicity than A. Slaouti et al.'s work [27]. The example is shown in figure 27. The instantaneous vorticity contours and streamline were also illustrated so we can see movement of flow behind cylinders apparently.

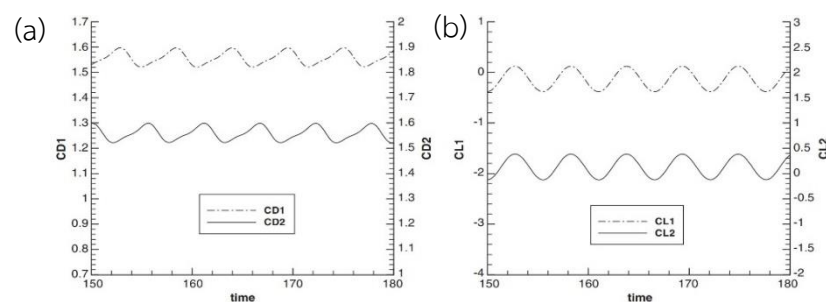


Figure 27 Drag and lift coefficients for side-by-side cylinders at  $Re=100$ :  $T=3$



A. Harichandan et al. [29] used unstructured grid based finite-volume discretization to solve Navier-Stokes equation for viscous flow past single or array of circular cylinders. This study also designed configuration geometry of cylinders going after H. Ding et al. [28] and A. Slauti et al. [27] but with different method. The finite-volume grid structure from this study has the similar mesh type from ANSYS-Mesh which we used for our simulation. The grid of 'side-by-side' arrangement of two cylinders,  $T/D = 1.5$ , is shown in figure 28.

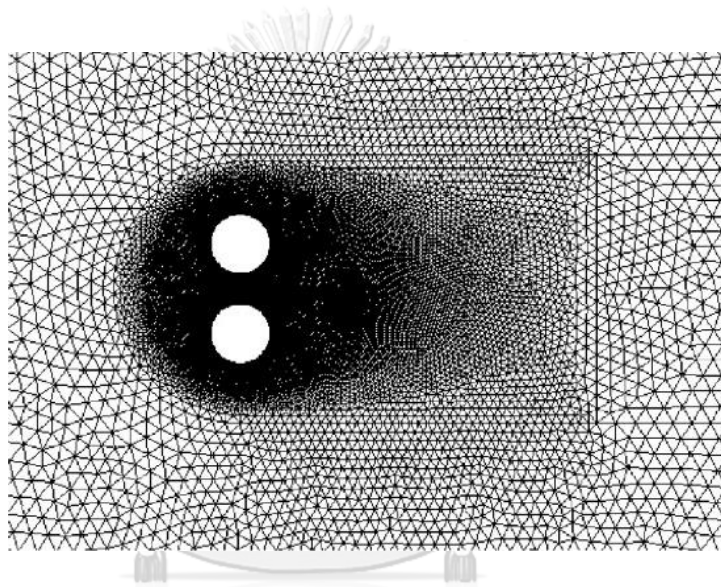


Figure 28 The grid of two 'side-by-side' cylinders for  $T/D = 1.5$

Its results around cylinders surface, including drag coefficient, lift coefficient, Strouhal number, also followed to previous studies and these results agreed reasonably well with them. The further study on the flow past three cylinders on both 'tandem' and 'side-by-side' arrangements with variety of spacing gap range is demonstrated in this paper. The plots of force coefficients with time are shown in figure 29 which are noticed that they have the same tendency with results of [28] and we used these drag and lift coefficient with time-dependence from both papers at Reynolds number of 100 for comparison.

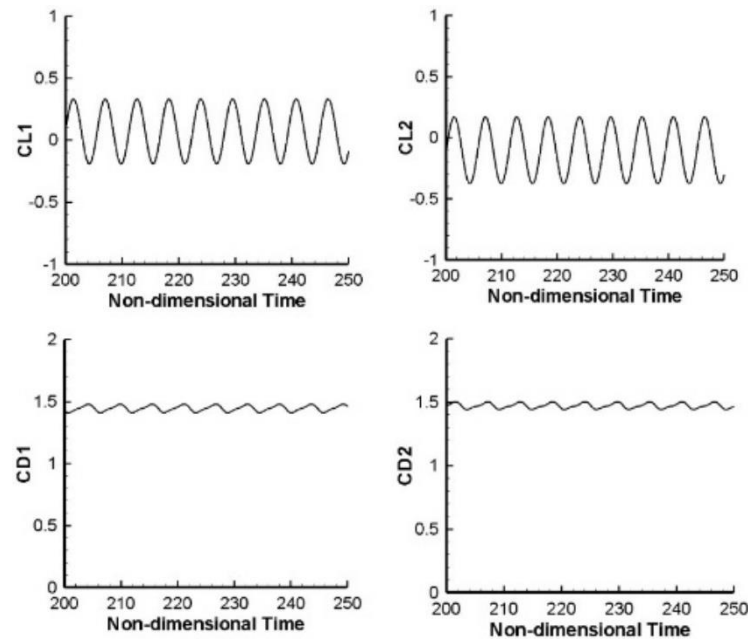


Figure 29 Drag and lift coefficients for side-by-side cylinders at  $Re=100$ :  $T=3$

The majority of M. Zhao et al.'s research [30] is very attractive that they presented flow around a pair of circular cylinders with different diameters. They claimed this study is relevant to pipelines in offshore for oil and gas engineering site. The large cylinder represented main pipeline and the small one represented piggyback pipeline. The diameter ratio of small cylinder to large one was maintained at 0.25. The outline of this study is shown in figure 30.

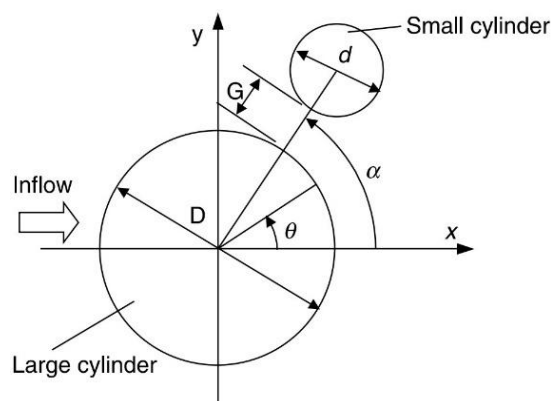


Figure 30 Outline of large and small cylinders

Due to the different diameters of these cylinders, Reynolds number of 500 is for large cylinder and 125 is for the small one. We were interested the position angle of cylinder which varied 0 to  $\pi$  referred by flow direction. As their result, the angle position is more effective to drag and lift coefficient of small cylinder than the big one. The drag coefficient is at the lowest point for angle = 0 or located behind the large one. In the other hand, the highest drag coefficient appeared when the angle =  $\pi/2$  or in the 'side-by-side' arrangement and it is greater than value of single cylinder at angular location between  $0.3\pi$  to  $0.75\pi$  then it decreased as the small cylinder moved into the wake of the large cylinder. The mean lift coefficient increased higher than value from a single cylinder when the angle is more than  $0.3\pi$ . The force coefficients of large and small cylinders in time-average are shown in figure 31 and 32.

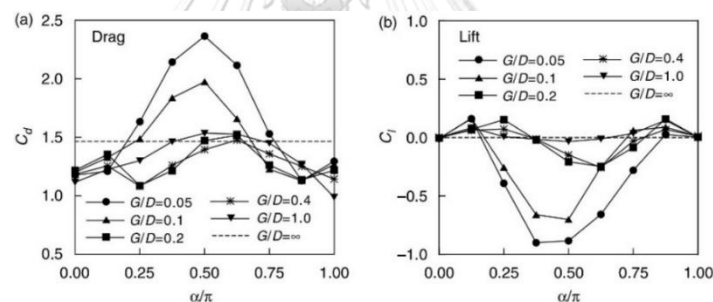


Figure 31 Time averaged force coefficients on the large cylinder: (a) drag coefficient, (b) lift coefficient

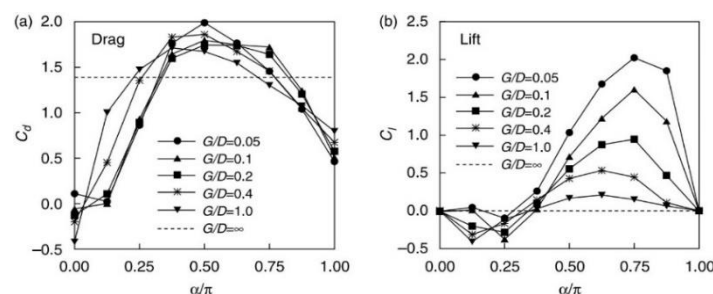


Figure 32 Time averaged force coefficients on the small cylinder: (a) drag coefficient, (b) lift coefficient

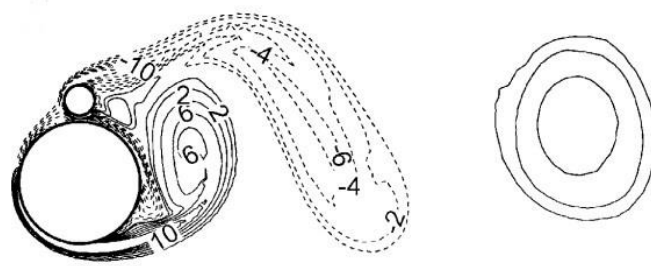


Figure 33 Instantaneous vorticity gap range = 0.05 and angle =  $\pi/2$

From all of the literatures above, the results to which we attend from a pair of cylinders are widely available, nonetheless, the results from array of cylinders that relate to our purpose are very difficult to find out. Thus, we recognized the knowledge gap that the simulation of flow past array of cylinders should be achieved to define the significant results, such as drag, lift coefficient and Strouhal number. It would be more or less useful to the relate problems that we surveyed above.

### 2.2.3 Other designs of sand fences and breakwaters

The study of Rudolph P. Savage [31] consists of construction of zigzag and straight types of arrangements of sand fences in state of North Carolina, U.S.A to determine the most effective design in building a sand dune by trapping windblown sand. The zigzag arrangement, shown in figure 34, appears more effective to trapping sand than straight type due to its spaces inside the model.

Another study occurred in Thailand that C. Chinnarasri [32] investigated efficiency of triangular shape of breakwater made of bamboo sticks. The modules were constructed on a mid-slope muddy shoreline in the upper Gulf of Thailand, Bang Khun thian, Bangkok. The plan of triangular module of breakwater made by bamboo fencing is shown in figure 35.

The last type of arrangement, in which we are interested, is called T-shape, shown in figure 36. T. Albers [33] investigated this configuration in muddy shoreline in

Vietnam that not only the model reduce effect of wave energy transmission to shoreline but tail of T-shape model also can restore sediment and create condition of mangrove regeneration.

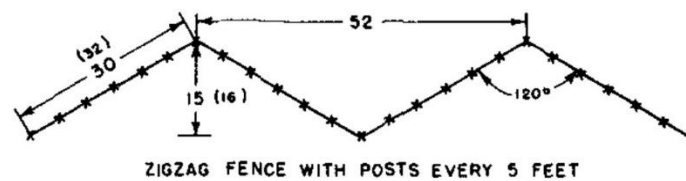


Figure 34 Zigzag arrangement of sand fence [31]

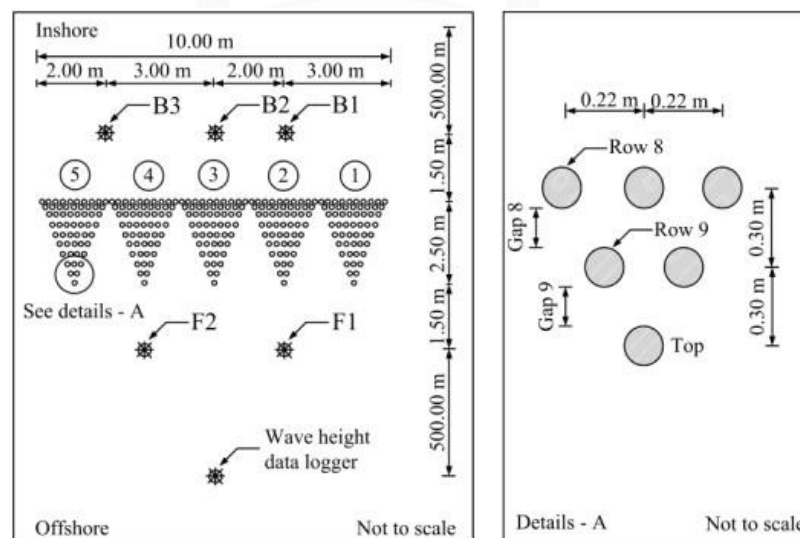


Figure 35 The set of triangular modules of the breakwater [32]

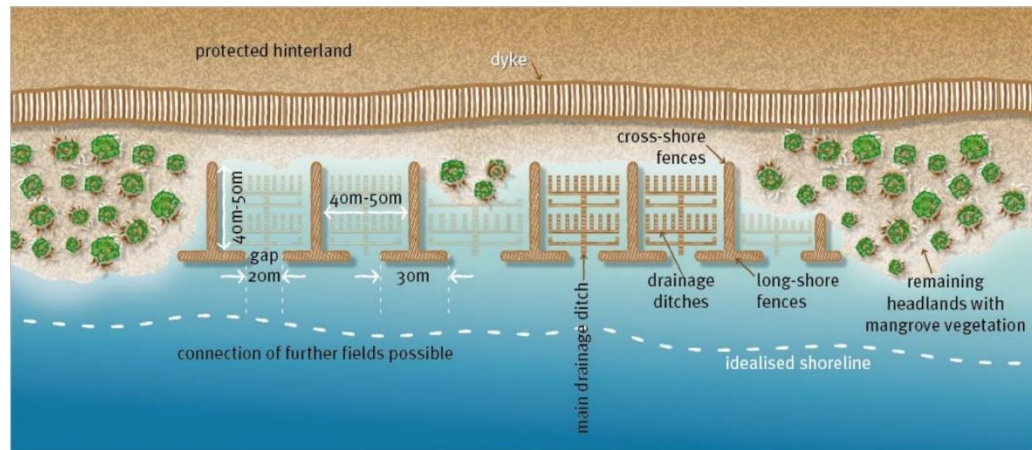


Figure 36 The model of T-shaped bamboo-fencing and its actual placement in the coastal zone of the lower Mekong Delta in Vietnam [33]

## CHAPTER 3

### RESEARCH METHODOLOGY AND VALIDATION

#### 3.1 Research methodology

##### 3.1.1 Numerical process of CFD

Nowadays, numerical simulation of fluid flow or heat transfer can be conveniently model by huge number of commercial software such as ANSYS-CFX, ANSYS-Fluent, COMSOL and STAR-CD, in our study, ANSYS-Fluent is selected to solve the problems. These programs are produced practically and friendly for user and the procedure of numerical process of CFD is summarized in figure 37.

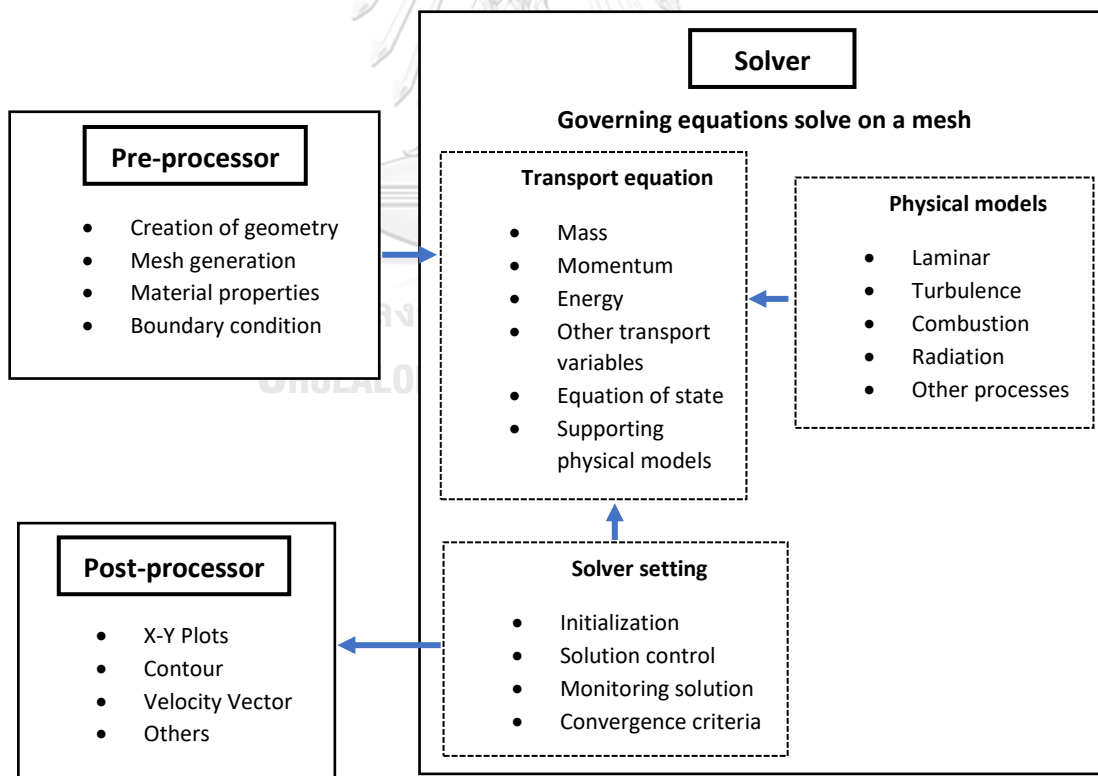


Figure 37 The functions of the three main elements within a CFD analysis framework

### **3.1.1.1 Problem setup**

- **Creation of Geometry**

The beginning step of any CFD is to define and create computational geometry model for the numerical simulation. Thus, CFD users need to design their own geometry, 2D or 3D, for representation of an object's shape and manipulate the proportion of surface or volume on domain of geometry for considering discretization of the fluid flow and heat flux. Anyway, users should remind that the geometry need to be thought over for mesh generation in next step.

- **Mesh generation**

The mesh generation is one of the most significant steps in the setup process after the creation of geometry. In the commercial CFD, the programs require the subdivide of domain into an amount of smaller without over-lapping for precise calculation.

The results of generation create subdomain, called mesh (or grid) of cells (or elements), overlying the whole geometry. By the way, the mesh generation has several techniques, such as structured or unstructured arrangement, depending on appropriate design of each domain.

- **Fluid properties**

The commercial CFDs have been built up for various physical and complicatedly chemical condition for fluid flow providing to many engineering fields, such as industries, offshore cite or environmental behavior. Thus, users need to attribute suitable initial properties before simulation to purpose the condition of real fluid.



- **Boundary condition**

Boundary condition step is relevant to previous step that the CFD uses have to define state of surface or area to proper condition, such as wall, insulation, inlet and outlet of flow, to mimic the genuine physical representation. On the other hand, this step specifies path of flow and heat flux dominance that border the flow geometry and the internal obstacles within the flow domain.

- **CFD solver**

This method is used to initialize solution procedure of simulation to reach the most precise result from control volume method (we will describe control volume method (CVM) in next part). Users can also set-up monitoring convergence during simulation that they can observe the performance all along simulation step-by-step.

- **Post process**

The post process is the last process of CFD. It shows all the outcome at finished point then users can call upon the particular results, display x-y plot, flow properties in form of vector and contour and show the simulating streamline as animation.

### **3.1.2 Finite volume method**

The momentum conversation of Newtonian fluid flow has been solved by partial differential equations (PDE), called Navier-Stokes equations, since the 18<sup>th</sup> century by Leonard Euler that we studied some part of PDE theory in the Advance Mathematics subject. However, the equations can only clarify quite simplified fluid flow but they are too complicated to deal with real cases. Nevertheless, in present technology, large access memories and very high speed processor of computers have capability enough to solve the Navier-Stokes equations with continuity at the same time using several numerical techniques such as finite difference method (FDM), finite element method (FEM) and finite volume method (FVM). In our study, we used

the commercial CFD ANSYS-Fluent to solve the equations for 2D unsteady flow of Newtonian incompressible fluid that the program implements finite volume techniques. The description of finite volume method (FVM) applying with the Navier-Stokes will be demonstrated as below.

Discretization of differential equations with FVM is one of the most popular numerical method applied with fluid flow. The original computational domain in FVM is discretized into petite subdomains called control volumes that flow governing equations are individually integrated over control-volume subdomains and they are computed consequently to the primary domain. In FVM, the volume integrals are transformed to surface integrals by Divergence theorem which we also studied in Advance Mathematics class then the results are transfer to adjacent meshes.

According to J. H. Ferziger's textbook, "Computational Methods for Fluid Dynamics" [35], the staggered two-dimensional grid based on SIMPLE-algorithm is a setting for spatial discretization, in which the flow parameter variables are not computed and transfer at the same position. Pressure is computed at the center of control volume but velocity components are calculated at the center of faces between control volumes. We will show the description below.

### **3.1.2.1 The governing equations**

The Governing equations of incompressible Newtonian fluid flow, described in Chapter 2, consist with the conversation of mass, known as continuity equation (from equation (1)) and conversation of momentum, known as momentum equations (from equations (2) and (3)). The equations (1), (2) and (3) are reduced the forms and transformed to dimensionless equations as:

Continuity equation:

$$\nabla \cdot \mathbf{v} = 0 \quad (27)$$

Momentum equation:

$$\frac{\partial \mathbf{v}}{\partial t} + \nabla \cdot (\mathbf{v}\mathbf{v}) = -\nabla p + \frac{1}{Re} (\nabla \cdot (\nabla \mathbf{v})) \quad (28)$$

where  $\mathbf{v}$  represents components of velocity  $u$  and  $v$  at the Reynolds number as equation (4) and time  $t$

$\nabla$  represents the del operator

### 3.1.2.2 Discretization of finite volume method and solution

Continuity equation and Navier-Stokes equation need to be integrated over control volume for each subdomain to transform the equations to system of algebraic equations for FVM.

Integrating equation (28) over control volume  $\Omega$ :

$$\iiint_{\Omega} \nabla \cdot \mathbf{v} d\Omega = 0 \quad (29)$$

Applying Gauss's Divergence Theorem to equation (29):

$$\iint_S \mathbf{v} \cdot \mathbf{n} dS = 0 \quad (30)$$

where  $\mathbf{n}$  is a unit vector perpendicular to surface  $S$

Afterwards, we transform to:

$$\iint_S \mathbf{v} \cdot \mathbf{n} dS = \sum_f \left( \iint_{S_f} \mathbf{v} \cdot \mathbf{n} dS_f \right) \approx \sum_f \mathbf{v}_f \cdot \mathbf{n}_f A_f \quad (31)$$

where  $\sum_f$  is summation over face of each control volume

$A_f$  is the area of the face  $f$

$\mathbf{v}_f$  is value of velocity at the center of the face  $f$

$\mathbf{n}_f$  is a unit vector perpendicular to face  $f$

the picture of 2D control volume is depicted in figure 38.

Then, we get:

$$\sum_f \mathbf{v}_f \cdot \mathbf{n}_f A_f = 0 \quad (32)$$

Integrating momentum equation over control volume  $\Omega$ , we separate equation (29) apart and apply Gauss's Divergence Theorem to all of the terms as well:

**Unsteady term**

$$\iiint_{\Omega} \frac{\partial \mathbf{v}}{\partial t} d\Omega = \frac{\partial \mathbf{v}}{\partial t} \Delta V \quad (33)$$

Where  $\Delta V$  is the volume of  $\Omega$

**Convection term**

$$\iiint_{\Omega} \nabla \cdot (\mathbf{v}\mathbf{v}) d\Omega = \iint_S (\mathbf{v}\mathbf{v}) \cdot \mathbf{n} dS = \sum_f \left( \iint_{S_f} (\mathbf{v}\mathbf{v}) \cdot \mathbf{n} dS \right) \approx \sum_f (\mathbf{v}\mathbf{v})_f \cdot \mathbf{n}_f A_f \quad (34)$$

**Pressure gradient term**

$$-\iiint_{\Omega} \nabla P d\Omega = -\iint_S p \mathbf{n} dS = -\sum_f \left( \iint_{S_f} p \mathbf{n} dS \right) \approx -\sum_f p_f \mathbf{n}_f A_f \quad (35)$$

### Viscous term

$$\iiint_{\Omega} \frac{1}{Re} \nabla \cdot (\nabla \mathbf{v}) d\Omega = \frac{1}{Re} \iint_S (\nabla \mathbf{v}) \cdot \mathbf{n} dS = \frac{1}{Re} \sum_f \left( \iint_{S_f} (\nabla \mathbf{v}) \cdot \mathbf{n} dS \right) \approx \frac{1}{Re} \sum_f (\nabla \mathbf{v})_f \cdot \mathbf{n}_f A_f \quad (36)$$

From equations (33-36), all momentum equations are consisted to the Navier-Stokes equation as:

$$\frac{\partial v}{\partial t} \Delta V + \sum_f (\mathbf{v}\mathbf{v})_f \cdot \mathbf{n}_f A_f = - \sum_f p_f n_f A_f + \frac{1}{Re} \sum_f (\nabla \mathbf{v})_f \cdot \mathbf{n}_f A_f \quad (37)$$

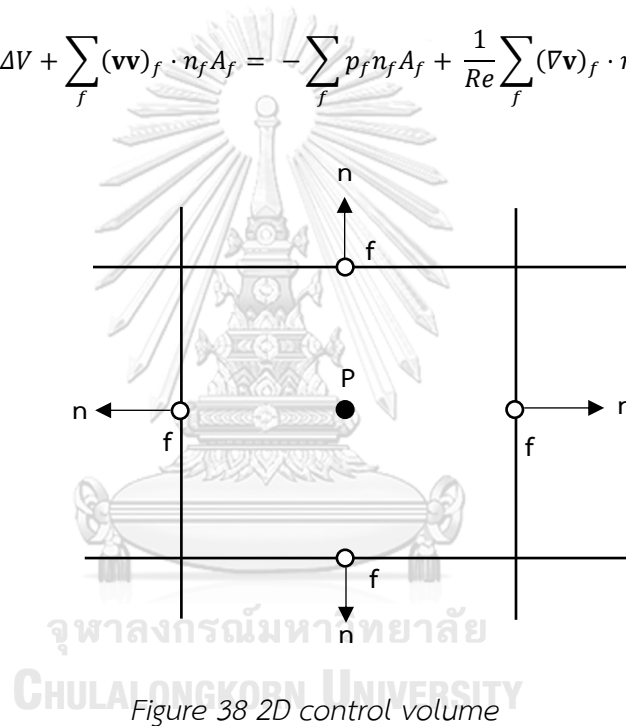


Figure 38 2D control volume

### 3.1.3 Geometrical arranging description

#### 3.1.3.1 The 'side-by-side' arrangement

As the review of previous literatures in the chapter 2, the fluid flow past a circular cylinder was studied for long time by both experiment and numerical simulation therefore, we will use this concept for validation. The configuration for a single cylinder is shown in figure 39. A pair of cylinders is very much more complicated as compared with a single cylinder because of interference effect

between cylinders. Hence, we set up the simulation of two ‘side-by-side’ cylinders that the geometrical description of arranged configuration is depicted in figure 40.

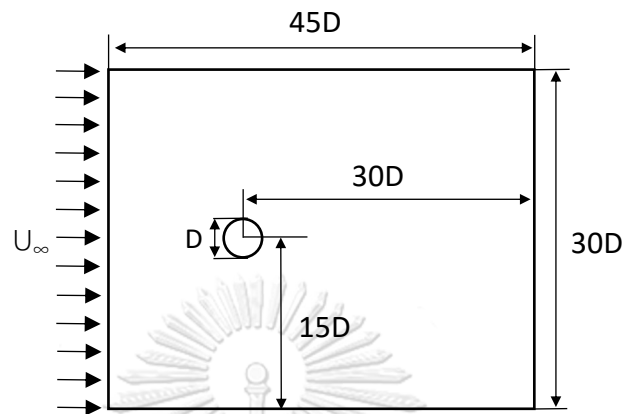


Figure 39 The single cylinder schematic description

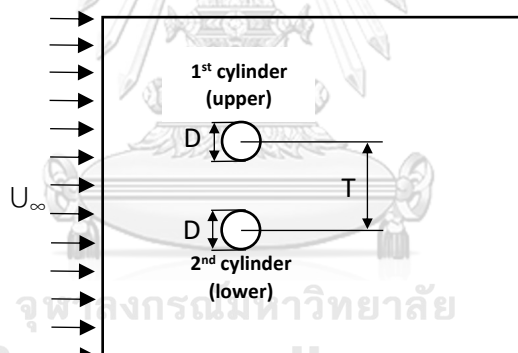


Figure 40 The ‘side-by-side’ arrangement schematic description

where  $D$  is diameter of cylinders

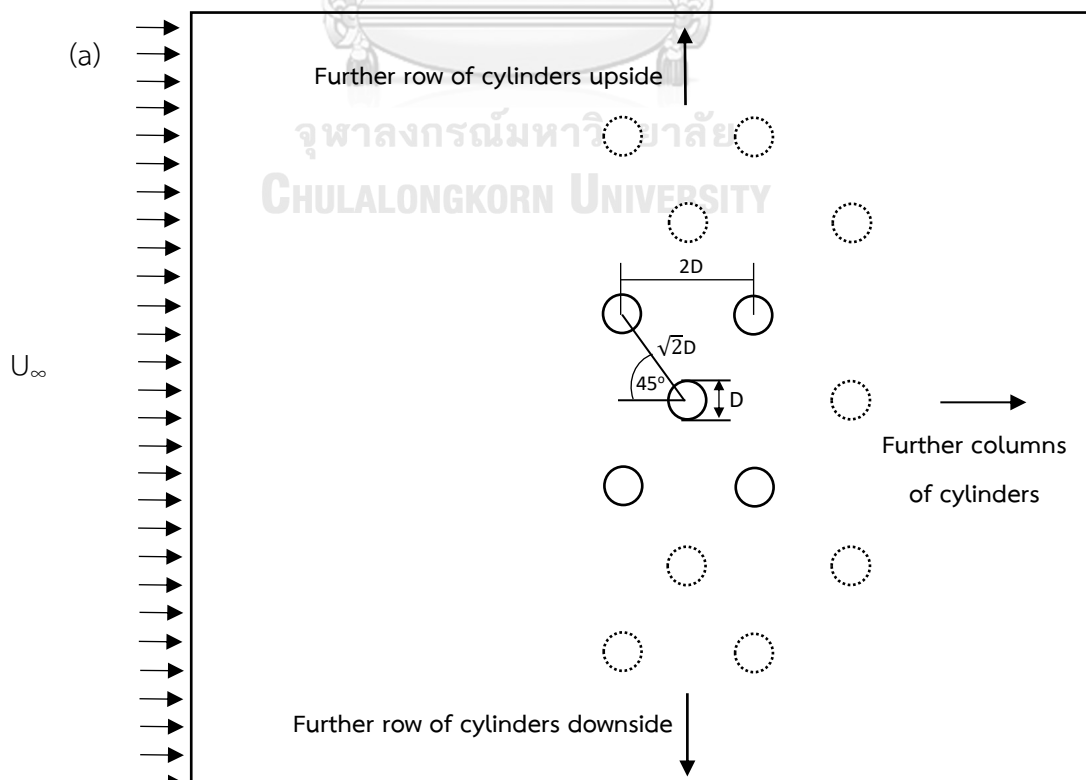
$T$  is a transverse distance

The two-dimensional problem is set up and solved in the dimensionless manner. The incompressible unsteady flow is allowed to march for about 4.5 flow throughs, from an initial condition of uniform  $U_\infty$ , to ensure that the steady state is reached before collecting data. It should be noted that to reach the steady state,

according to M. M. Zdravkovich [25], it takes a non-dimensional time of approximately 150 which is 3.3 flow throughs in corresponding to our computational domain.

### 3.1.3.2 The array arrangements of cylinders

In real situation of human lives, objects which the flow moves through is usually organized in several arrangements, like the related problems for which we reviewed, or sometimes disorganized. Therefore, we created simulations that will represent more real-world events. We created the geometry of arrays of cylinders to mimic the breakwater made of bamboo, called bamboo-fencing, along the muddy shoreline in front of the Gulf of Thailand. The detail of blueprints of bamboo-fencing in figure 7 from the department of marine and coastal resources (DMCR). In our study, we recognized the conceptual framework that the bundle of cylinders should be principally manipulated for 2 types of arrangement: (1) staggered arrangement, (2) aligned arrangement. The schematic description for both of arrangements are depicted in figure 41.



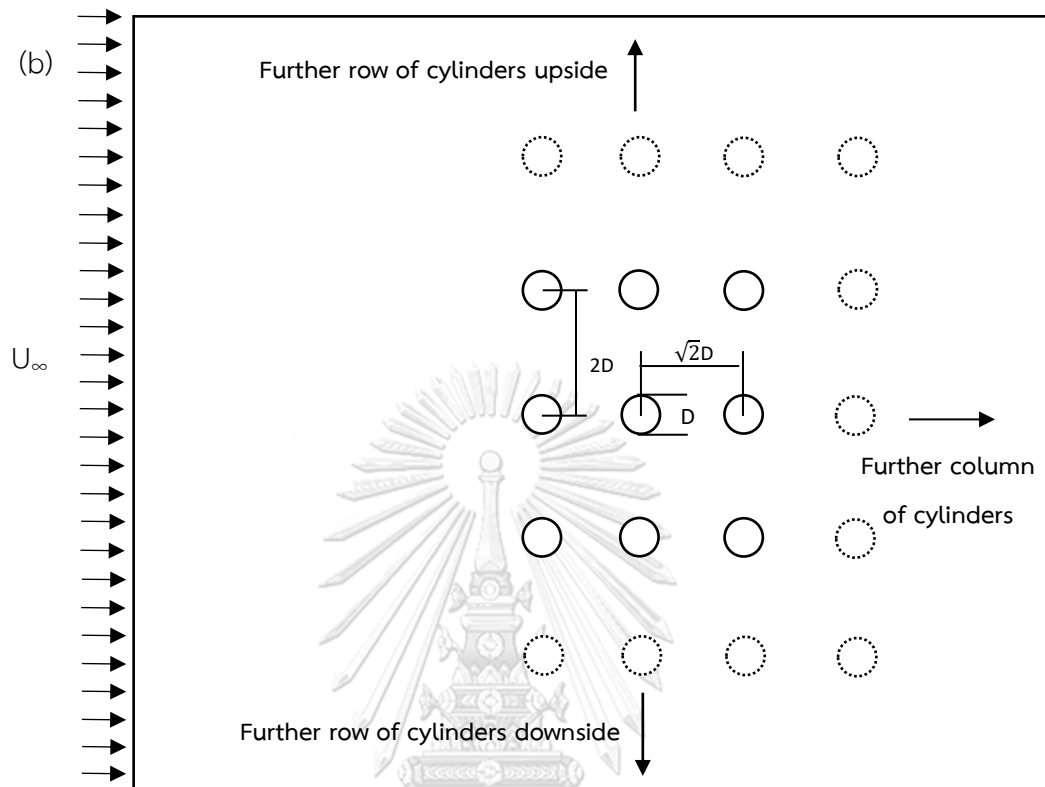


Figure 41 The schematic description of array of cylinders: (a) staggered arrangement, (b) aligned arrangement

The staggered arrangement, especially with 5 columns, is referred to the design from DMCR (the detail of design is illustrated in figure 42) and provided to many provinces which confront to the coastal erosion. Nevertheless, the aligned one is easier to organize. We begin the simulation with 3 columns of geometry as figure 41 for both of arrangement, then the column will be added for comparison.

Other designs of arrangement on previous research will be established for the study of numerical simulation as well, shown in chapter 5.



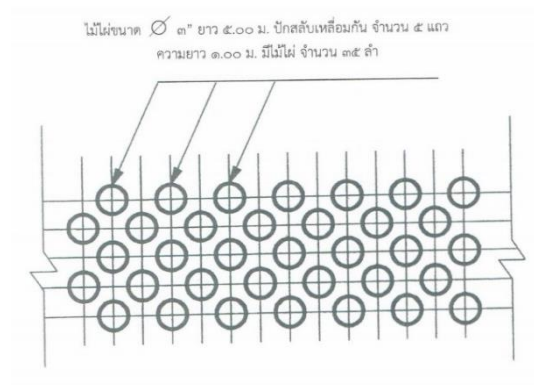


Figure 42 The detail of breakwater made by bamboo designed by DMCR

### 3.2 Validation

Before we present the results of the primary problem stated above, a set of simulations of flow past a single cylinder at  $Re = 100$  is performed in order to obtain an optimal mesh (number of distribution), time step size, as well as to validate the setup by comparison against literatures, shown in Table 2. The reliable data from researchers, H. Ding [28], A. Harichandan [29], M. Braza [21], C. Liu [22], and L. Qu [36] came from numerical simulations and those from D. J. Tritton [16] and C. Wiesenberger [37] were measured experimentally.

The set of simulations is conducted on a computational domain of size  $H=30D$  (height) and  $L=45D$  (length), shown in Figure 43 (left).

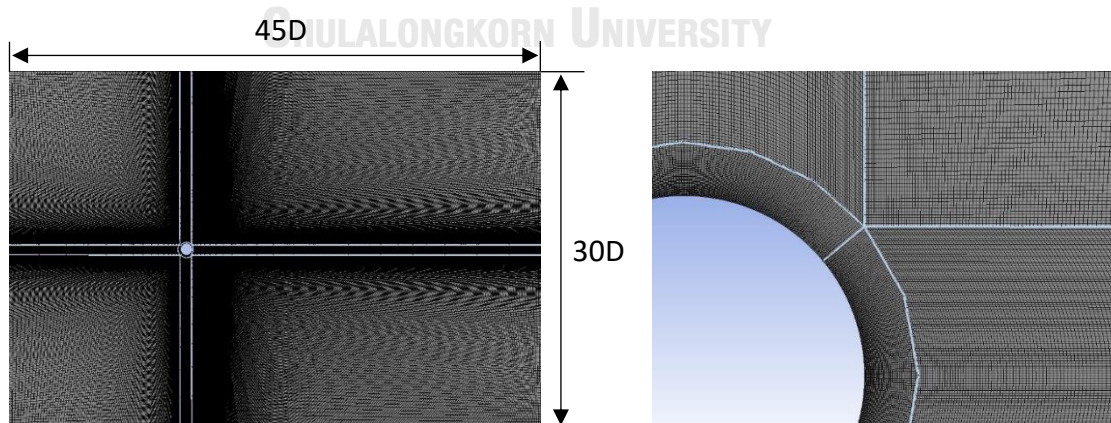


Figure 43 Computational domain (left) and near-cylinder mesh (right) for the baseline case

### 3.2.1 Baseline case

The baseline case, denoted R3, is performed first to establish if the order of element number and the time step size used can give results that lie within the acceptable ranges (bounded by the reference values). The number of elements and time step size is shown in table 3.

Table 2 lists mean value of drag coefficients, amplitudes of lift coefficients and Strouhal numbers respectively. It presents our results as well as other published data. The investigations with numerical method are from H. Ding [28], A. Harichandan [29], M. Braza [21], C. Liu [22], and L. Qu [36] and the rest of data on table 2, using experimental method, are from D. J. Tritton [16] and C. Wiesenberger [37]. It can be observed that our results have reasonably well agreement with those reports by the mentioned researchers.

According to table 2, our mean values of drag coefficients very marginally differ from those of H. Ding [28], A. Harichandan [29], M. Braza [21] and C. Liu [22] by less than 1%. It can be noticed that experimental D. J Tritton [16] and C. Wiesenberger, C. [37] reports show a little bit higher percentage of drag coefficients percentage by our value approximately 2.2% and 1.7% respectively. Our lift coefficient's amplitude deviates from H. Ding [28] 8.3%, A. Harichandan [29] 11.18% and M. Braza et al. [21] 20.13%. The lift coefficient's report from C. Liu [22] is only one that higher than ours about 7.7%. Qu (2013), experimental D. J. Tritton [16] and C. Wiesenberger [37]'s researches do not identify lift coefficient. Agreement of Strouhal number from our simulation looks very satisfied with all mentioned other researches that the difference is less than 2.2%. Furthermore, the remarkable experiment from A. Roskho [17], being well-known as the characteristic flow expert, indicated that the characteristic frequency for a circular cylinder at  $Re = 100$  is around 0.16-0.165. In addition, the drag and lift coefficients with time-dependence are shown in figure 44.

Table 2 Reference results

Cases	$C_d$	$C_l$	$S_t$
R3	1.350	$\pm 0.313$	0.164
H. Ding [28]	1.356	$\pm 0.287$	0.166
A. Harichandan [29]	1.352	$\pm 0.278$	0.161
M. Braza [21]	1.364	$\pm 0.250$	0.160
C. Liu [22]	1.350	$\pm 0.339$	0.165
L. Qu [36]	1.317	-	0.165
D. J. Tritton [16]	1.320	-	0.160
C. Wiesenberger [37]	1.326	-	0.161

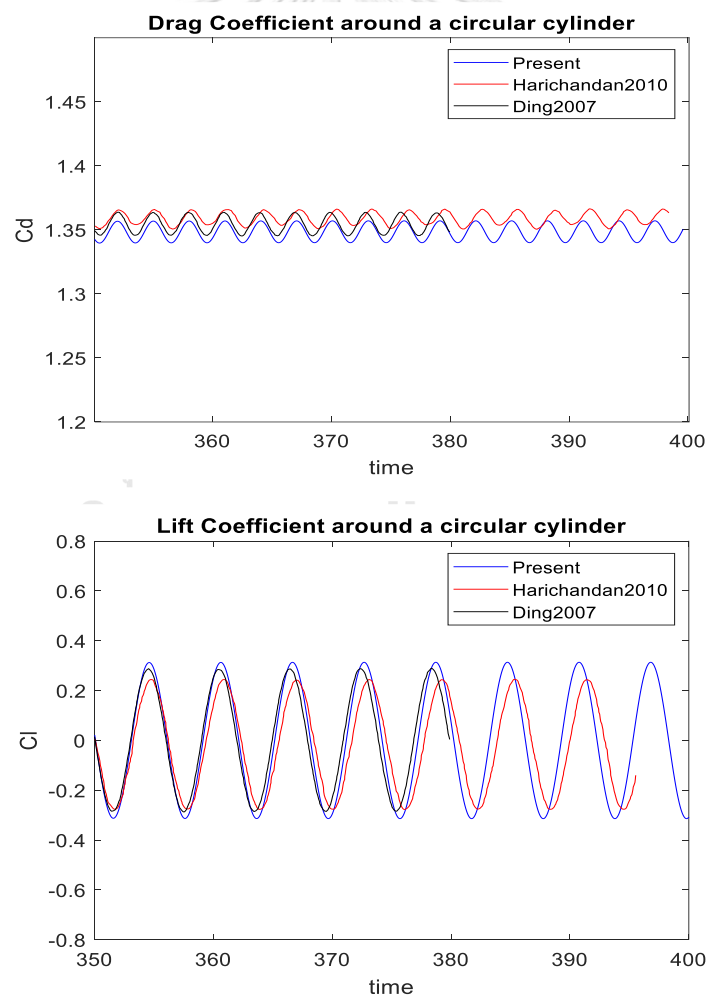


Figure 44 Drag and lift coefficients

### 3.2.2 Effect of time step

The study of time step or resolution of time was carried out for domain size  $30 \times 45$  dimensionless unit with approximate 300,000 meshes and the residual is set for  $10^{-6}$ . The results obtained using time steps ( $\Delta t$ ) from 0.1 to 0.05 in cases R1-R4 shown in Table 3.

There were perceptible influences from the time step on drag coefficients ( $C_d$ ), lift coefficients ( $C_l$ ) and Strouhal numbers ( $St$ ) between  $dt=0.005$  to  $dt=0.1$ . According to R1-R4 cases, time steps do not much affect to drag coefficients. R1 case has the largest time resolution and denotes  $C_d = 1.306$  that is not very notable gap compared with R3 ( $C_d = 1.350$ ) and R4 ( $C_d = 1.357$ ). In the part of lift coefficients, all of the cases result the  $C_l$  less than 10% difference and it can be doubted that the smaller time resolution is applied, the amplitude of lift coefficients expand higher. Strouhal number behind a circular cylinder at 100 Reynolds number is be defined approximately 1.6 referring to other studies and only R3 and R4 cases are similar that value.

As the results of time resolution, R3 and R4 seem reliably valid comparing with other references. However, R4 case, employing 0.005 time resolution, consumed too much computer resource. Hence, R3 (0.01 time step) is the most practical for our solution.

### 3.2.3 Mesh sensitivity

Mesh sensitivity study includes 6 cases (M1-M5, and R3) with mesh distribution, shown in Table 3, being almost identical in all the cases but the number of elements is scaled according to a preset value that ranges from 2,500 (M5) to 675,000 (M1). All of the mesh convergence cases are obtained using time step size of 0.01.

The result in Table 3 indicates that a minimum number of elements is of the order 55,000 (case M3) where the calculated  $C_d$ ,  $C_l$ , and  $St$  are close to the reference

values (Table 2). It is not clear why, in the M2 case,  $St$  deviates from the reference value (taken at 0.162) despite having more elements in comparison to the M3 case, providing that the mesh is distributed very similarly, while giving a better result in terms of  $C_d$  (reference value taken at 1.354) in comparison to the case M1 whose number of elements is larger by a factor of 5.

The number of elements in the order of 300,000-500,000 is chosen for the two-cylinder simulations based on the evidence that case R3, containing the number of elements being in the middle of M1 and M2, gives satisfactory results

*Table 3 The results from two-dimensional simulations at  $Re=100$*

Cases	Elements	$\Delta t$	$C_d$	$C_l$	$St$
R1	300,000	0.1	1.306	$\pm 0.2711$	0.1
R2	300,000	0.05	1.325	$\pm 0.2733$	0.14
R3	300,000	0.01	1.350	$\pm 0.313$	0.1636
R4	300,000	0.005	1.357	$\pm 0.325$	0.162
M1	675,000	0.01	1.340	$\pm 0.302$	0.160
M2	130,000	0.01	1.3586	$\pm 0.3185$	0.1556
M3	55,000	0.01	1.343	$\pm 0.3191$	0.160
M4	10,000	0.01	1.1635	$\pm 0.3205$	0.1261
M5	2,500	0.01	1.1826	-	0.0667

## CHAPTER 4

### PRELIMINARY RESULTS

This chapter is an initial part of results from the flow past a pair of cylinders arranged in ‘side-by-side’ configuration, the procedure of geometrical arrangement was described on chapter 3. This section presents the results from simulations of flow past two side-by-side cylinders with the transverse gap sizes  $T/D = 1.5$  and 3 in comparison to literatures as well as the dependency of  $C_d$ ,  $C_l$ , and  $St$  on the gap size ranging from  $T/D = 1.5$  to 20.

#### 4.1 Case $T/D = 1.5$ and 3: comparison with literatures

First part of the preliminary results, the simulations have been set for side-by-side arrangement of two cylinders that the gap between cylinders is  $T=1.5$  and  $T=3$ . We observed that the flow pattern would be bistable (drag and lift coefficient converge to stable state of both cylinders with narrow and wide wakes behind the cylinders and become an unsteady Karman-vortex street form when the time non-dimensional reaches approximately  $t=150$  as same agreement as Zdravkovich, M. M. [9] but we started observing at  $t = 200$  for good.

At  $T=1.5D$ , since this transverse gap is within the range of intermediate critical gap ( $1.1D < T < 2.2D$ ) observed by M. M. Zdravkovich [25] we cannot inspect any distinctive dominant frequency and the fully developed flows seem not periodic as figure 45 and 46. Therefore, Strouhal number, well-known as characteristic frequency, cannot be defined. Only mean drag and lift coefficients are resulted by time averaging over a substantial time period on Table 4 and Table 5. We compare our numerical results with those of H. Ding [28] and A. Harichandan [29] and both drag and lift coefficient are in acceptable agreement that  $C_d$  differ from A. Harichandan [29] and H. Ding [28] by 8.2% and 4.8% for upper cylinder, 2% and 1.3% for lower

cylinder respectively and H. Ding [28] by 4.8%.  $C_l$  have no difference compared with H. Ding [28] and they deviate by 13% from A. Harichandan [29] for both cylinders

At  $T=3D$ , M. M. Zdravkovich [25] studied that the Karman-vortex streets begin appearing and the fully developed flows are periodic as figure 47 and 48 when the gap for side-by-side arrangement is larger than  $2D$ . Thus, Strouhal number can be result by FFT and it results literally pleasure value both for upper and lower cylinders. Characteristic frequency values differ from both researchers' data less than 0.5%. As Table 4 and figure 47, the drag coefficients of both cylinders for our study show almost the same values as well as two researchers' results. The differences of mean  $C_d$  are below 5%. Lift coefficients' amplitudes for  $T = 3D$  do not appear very close to both results but mean values and frequency of both cylinders seem not severe, they are shown on figure 48. By the way, velocity contour for  $T/D = 1.5$  and 3 is shown in figure 49.

*Table 4 Drag Coefficient ( $C_d$ ), Lift Coefficient ( $C_l$ ) and Strouhal number ( $St$ ) comparison with the literatures*

T	cases	Drag coefficient ( $C_d$ )		Lift coefficient ( $C_l$ )		Strouhal number ( $St$ )	
		1 <sup>st</sup> cylinder	2 <sup>nd</sup> cylinder	1 <sup>st</sup> cylinder	2 <sup>nd</sup> cylinder	1 <sup>st</sup> cylinder	2 <sup>nd</sup> cylinder
1.5D	Present Result	1.46	1.49	-0.46	0.47	-	-
	H. Ding [28]	1.53	1.51	-0.46	0.47	-	-
	A. Harichandan [29]	1.58	1.52	-0.41	0.41	-	-
3D	Present Result	1.52 $\pm 0.0345$	1.51 $\pm 0.0345$	-0.13 $\pm 0.45$	0.13 $\pm 0.45$	0.1812	0.181
	H. Ding [28]	1.56 $\pm 0.03$	1.56 $\pm 0.03$	-0.131 $\pm 0.253$	0.131 $\pm 0.253$	0.182	0.182
	A. Harichandan [29]	1.45 $\pm 0.05$	1.45 $\pm 0.05$	-0.1 $\pm 0.25$	0.1 $\pm 0.25$	0.181	0.181

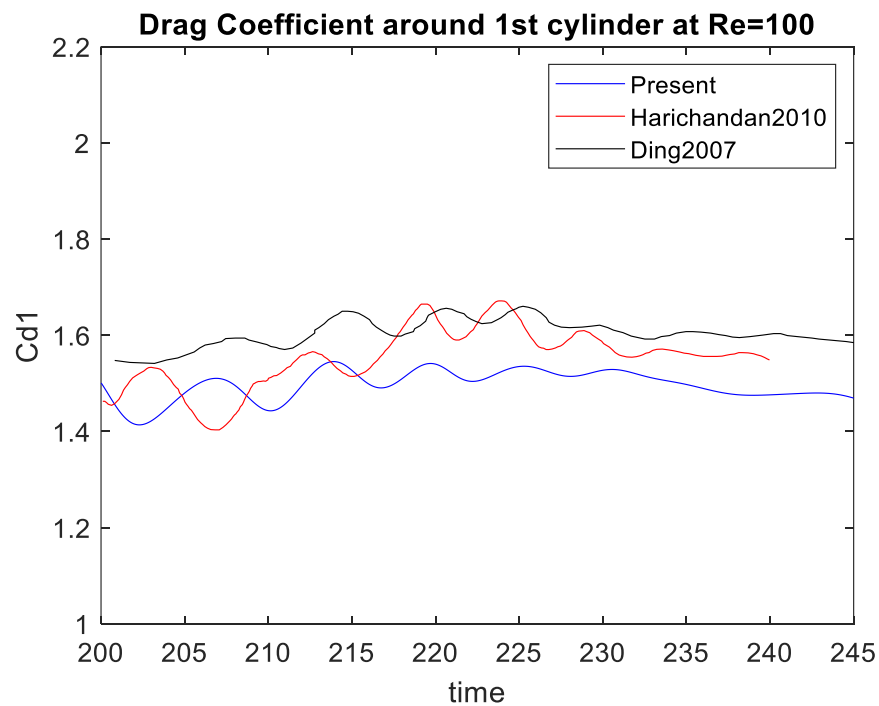
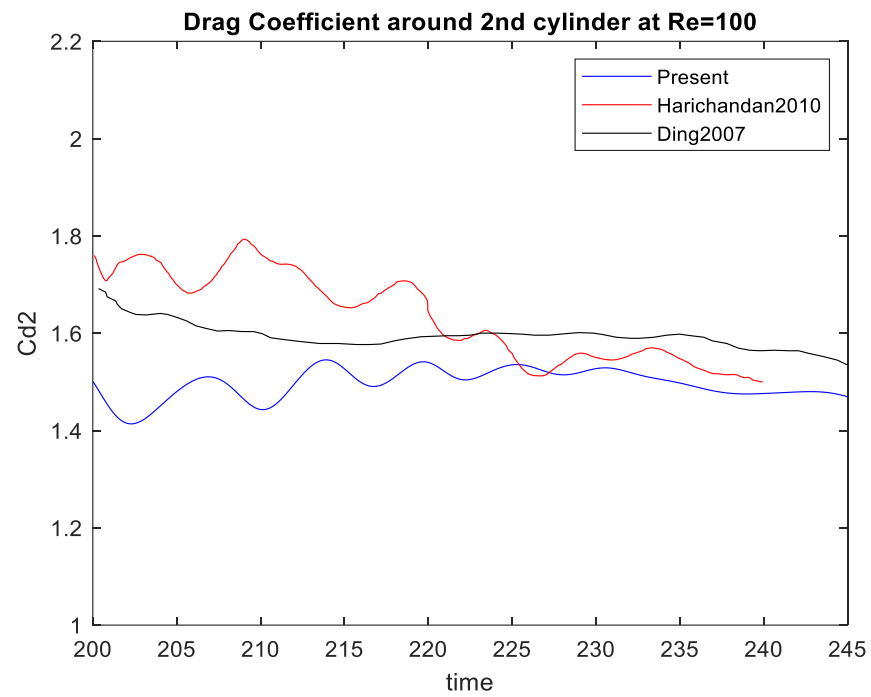


Figure 45 Drag coefficients ( $C_d$ ) with time-dependence comparison of flow past two side-by-side ( $T = 1.5D$ ) cylinders at  $Re = 100$



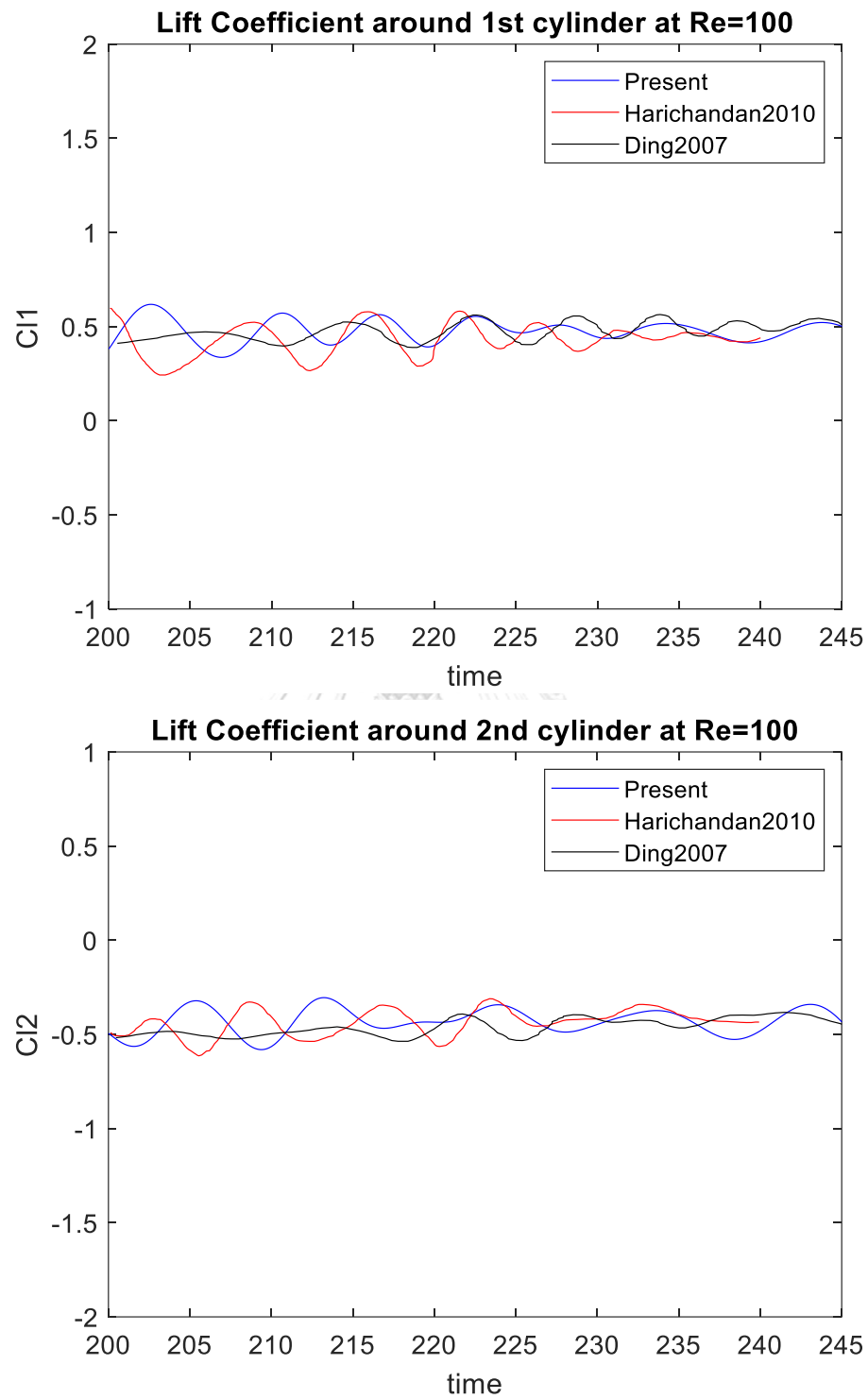


Figure 46 Lift coefficient ( $C_l$ ) with time-dependence comparison of flow past two side-by-side ( $T = 1.5D$ ) cylinders at  $Re = 100$

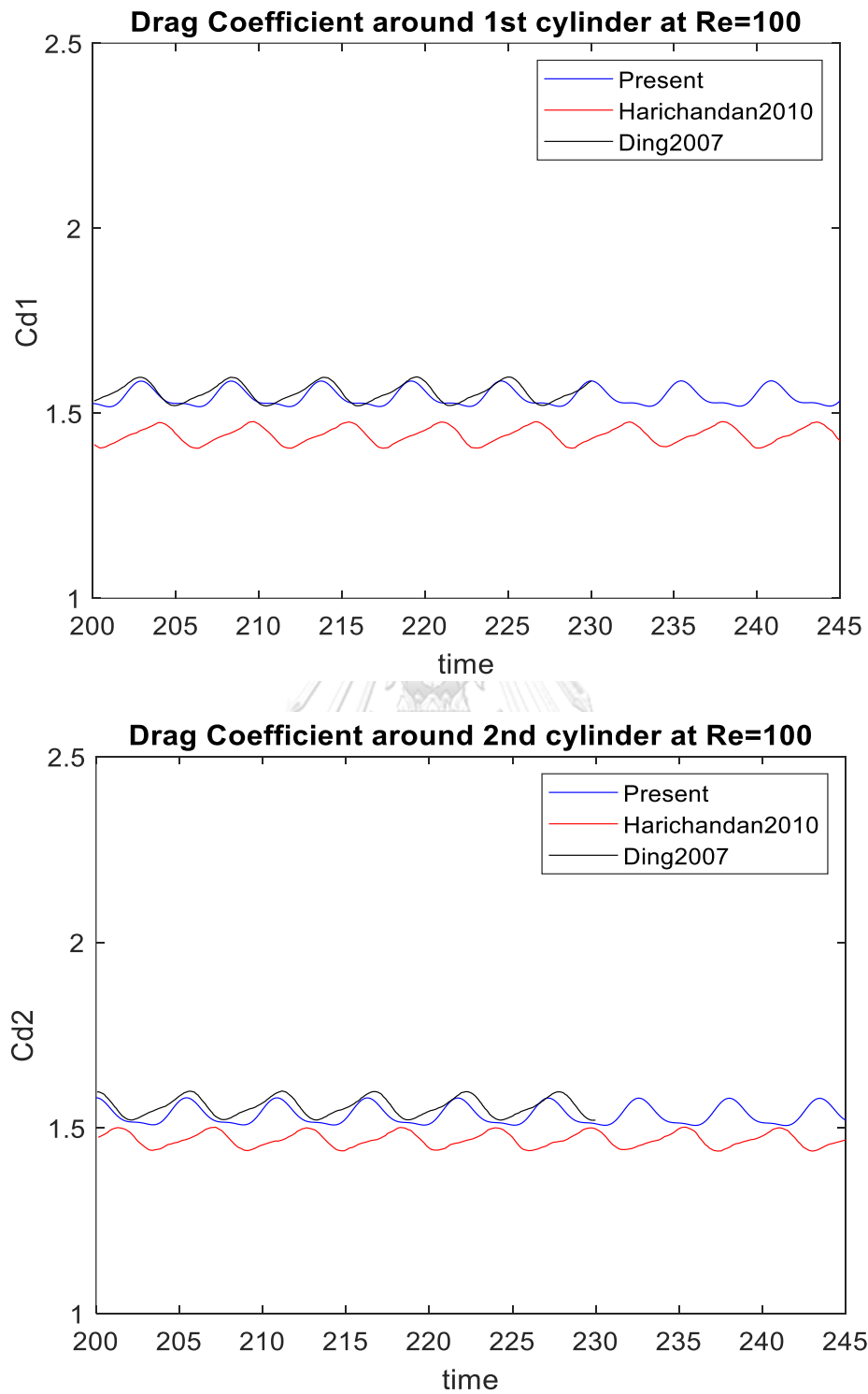


Figure 47 Drag coefficient ( $C_d$ ) with time-dependence comparison of flow past two side-by-side ( $T = 3D$ ) cylinders at  $Re = 100$

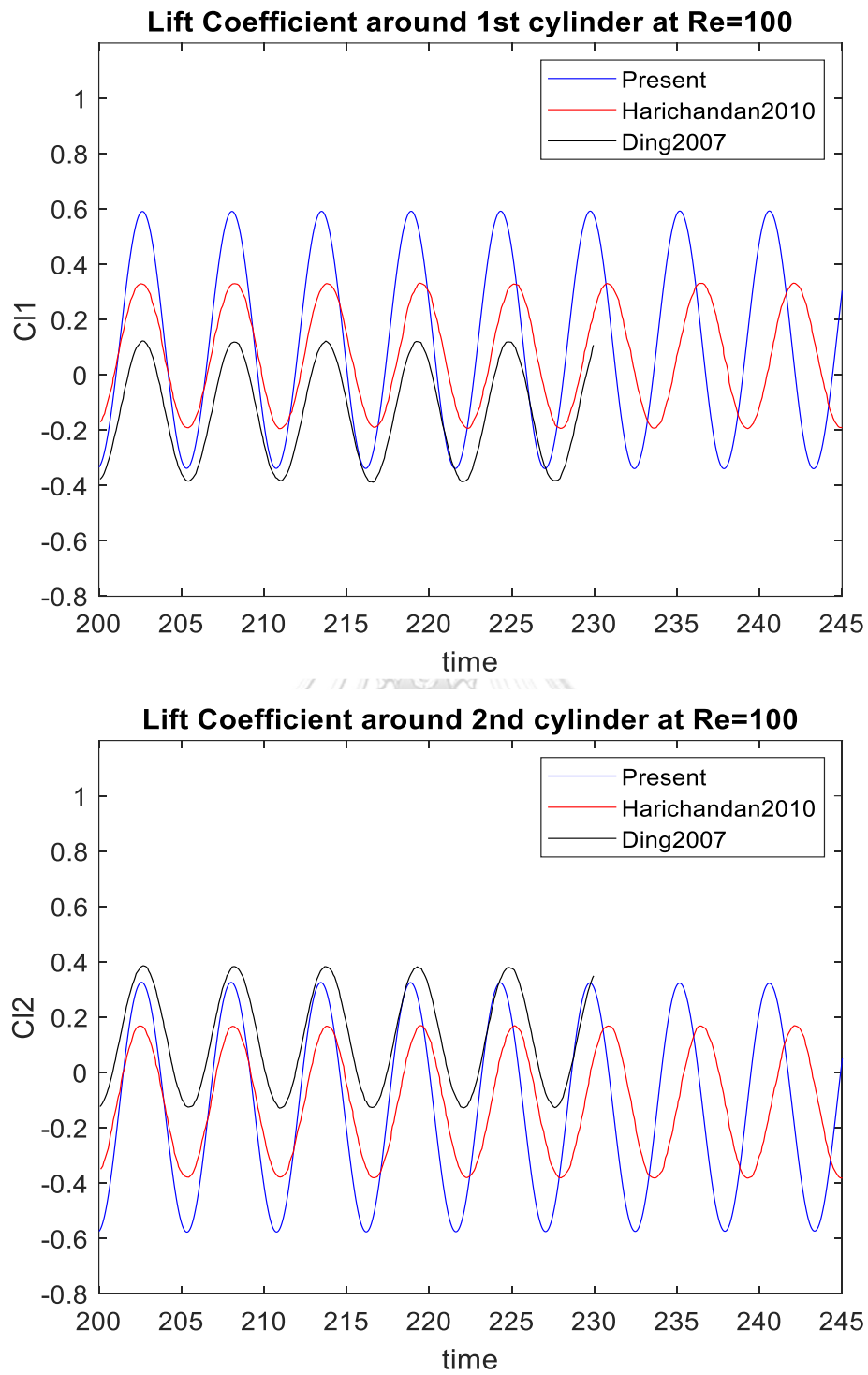
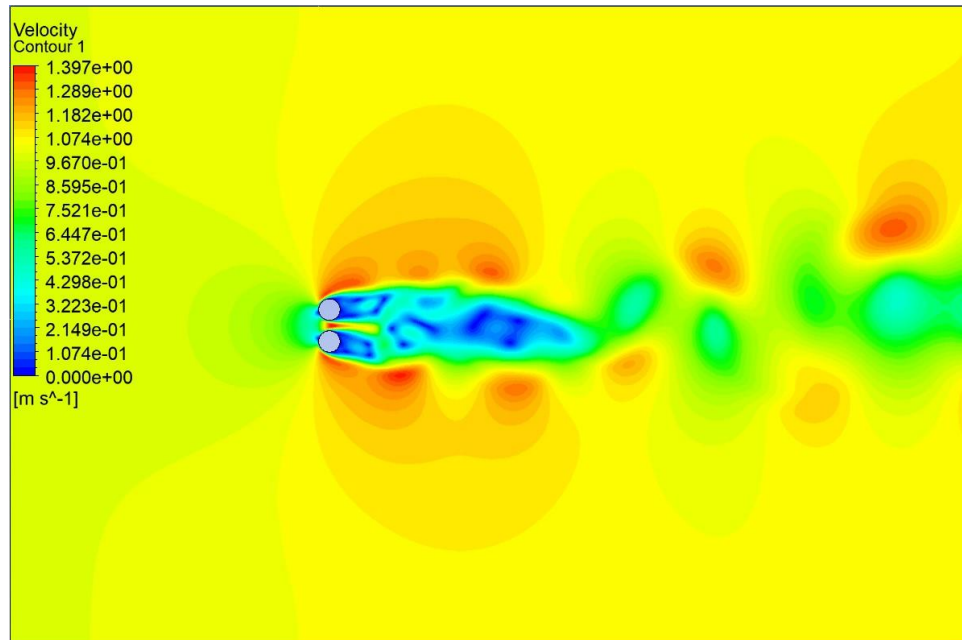


Figure 48 Lift coefficient ( $C_l$ ) with time-dependence comparison of flow past two side-by-side ( $T = 3D$ ) cylinders at  $Re = 100$

(a)



(b)

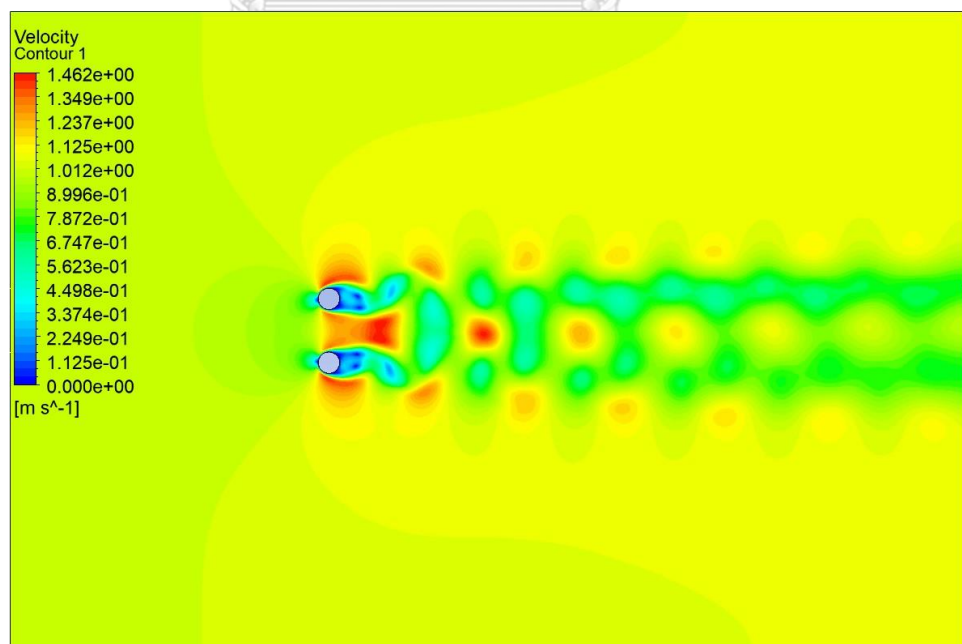


Figure 49 Velocity contour: (a)  $T/D = 1.5$ , (b)  $T/D = 3D$

## 4.2 Effects of the gap width

In this section, the drag and lift coefficients and Strouhal number are considered for variety of gap widths. The results of them are shown in Table 5, 6 and 7 respectively and visualized in Figure 50 and figure 51.

The result confirms our Intuitively guess in that increasing the width gradually diminishes the interaction between two flow streams passing the cylinders. As  $T/D$  increases, all of the interested dependent variables approach their corresponding values of the single cylinder. Placing cylinders side-by-side, at least for the  $T/D$  in the range studied here, increases drag, amplitude of lift force, as well as wake dominant frequency.

While obstructing a flow stream takes some streamwise momentum from it, obstructing and restricting the flow with an additional object arranged as in the present study further removes streamwise momentum from the stream. The incoming flow that diverges transversely, while passing the cylinders, does not freely advect its own streamwise momentum away by its transverse velocity component that is restricted by the other cylinder. Such modification enforces the stream to deposit a larger amount of streamwise momentum to the cylinders resulting in the larger drag coefficient.

According to figure 50 and 51, the increase in  $C_l$  magnitude can be explained in the similar manner as  $C_d$ . The transverse momentum of the incoming stream, while net-zero in total, distributes into positive and negative portions as the flow goes around the object. Toward the centerline (between the two cylinders), the transverse momentum is not freely advected away by transverse velocity thus enforce its larger deposit onto the cylinders.

Visualizing the result (Figure 52) shows that while  $C_d$  and  $St$  gradually decrease as the gap increases,  $C_l$  magnitude drops sharply during  $T/D < 7$  signifying a strong

influence from such span of gap size in modifying the flow stream in the transverse direction.

It is interesting to see that the characteristic frequency increases as the gap decreases. A possible hypothesis is that the converging-diverging gap channel accelerates the flow in between the cylinders, that induces rapid vortex shedding. The attempt in explaining this phenomenon is, however, beyond the scope of this study.

*Table 5 Drag coefficients ( $C_d$ ) of the flow past two side-by-side circular cylinders at various gap width*

T	Drag coefficient ( $C_d$ )		
	1 <sup>st</sup> cylinder	2 <sup>nd</sup> cylinder	Average
1.5D	1.46	1.49	1.475
3D	1.52	1.51	1.515
4D	1.49	1.49	1.49
5D	1.44	1.44	1.44
7D	1.40	1.40	1.40
9D	1.395	1.395	1.1395
12D	1.375	1.375	1.375
15D	1.356	1.356	1.356
20D	1.351	1.351	1.351
Single cylinder	1.350		

Table 6 Lift coefficients ( $C_l$ ) of the flow past two side-by-side circular cylinders at various gap width

T	Lift coefficient ( $C_l$ )		
	1 <sup>st</sup> cylinder	2 <sup>nd</sup> cylinder	$C_{l(R.M.S.)}$
1.5D	-0.4558	4.667	-
3D	-0.13 $\pm$ 0.45	0.13 $\pm$ 0.46	0.3506
4D	-0.0729 $\pm$ 0.3907	0.731 $\pm$ 0.3906	0.2864
5D	-0.048 $\pm$ 0.353	0.048 $\pm$ 0.353	0.2543
7D	-0.02585 $\pm$ 0.3291	0.0258 $\pm$ 0.3289	0.2336
9D	-0.0164 $\pm$ 0.3226	0.0163 $\pm$ 0.3277	0.2293
12D	-0.00605 $\pm$ 0.3161	0.0088 $\pm$ 0.3161	0.2258
15D	-0.0028 $\pm$ 0.3138	0.0088 $\pm$ 0.3138	0.2243
20D	-0.0088 $\pm$ 0.3192	-0.0088 $\pm$ 0.3192	0.2220
Single cylinder	$\pm$ 0.313		0.2164

Table 7 Strouhal numbers ( $St$ ) of the flow past two side-by-side circular cylinders at various gap width

T	Strouhal number ( $St$ )		
	1 <sup>st</sup> cylinder	2 <sup>nd</sup> cylinder	centerline
1.5D	-	-	-
3D	0.1812	0.1812	0.1812
4D	0.1812	0.1812	0.1812
5D	0.1812	0.1812	0.1812
7D	0.1721	0.1721	0.1721
9D	0.1761	0.1761	0.1761
12D	0.1642	0.1642	0.1642
15D	0.1642	0.1642	0.1642
20D	0.1642	0.1642	0.1642
Single cylinder	0.1636		



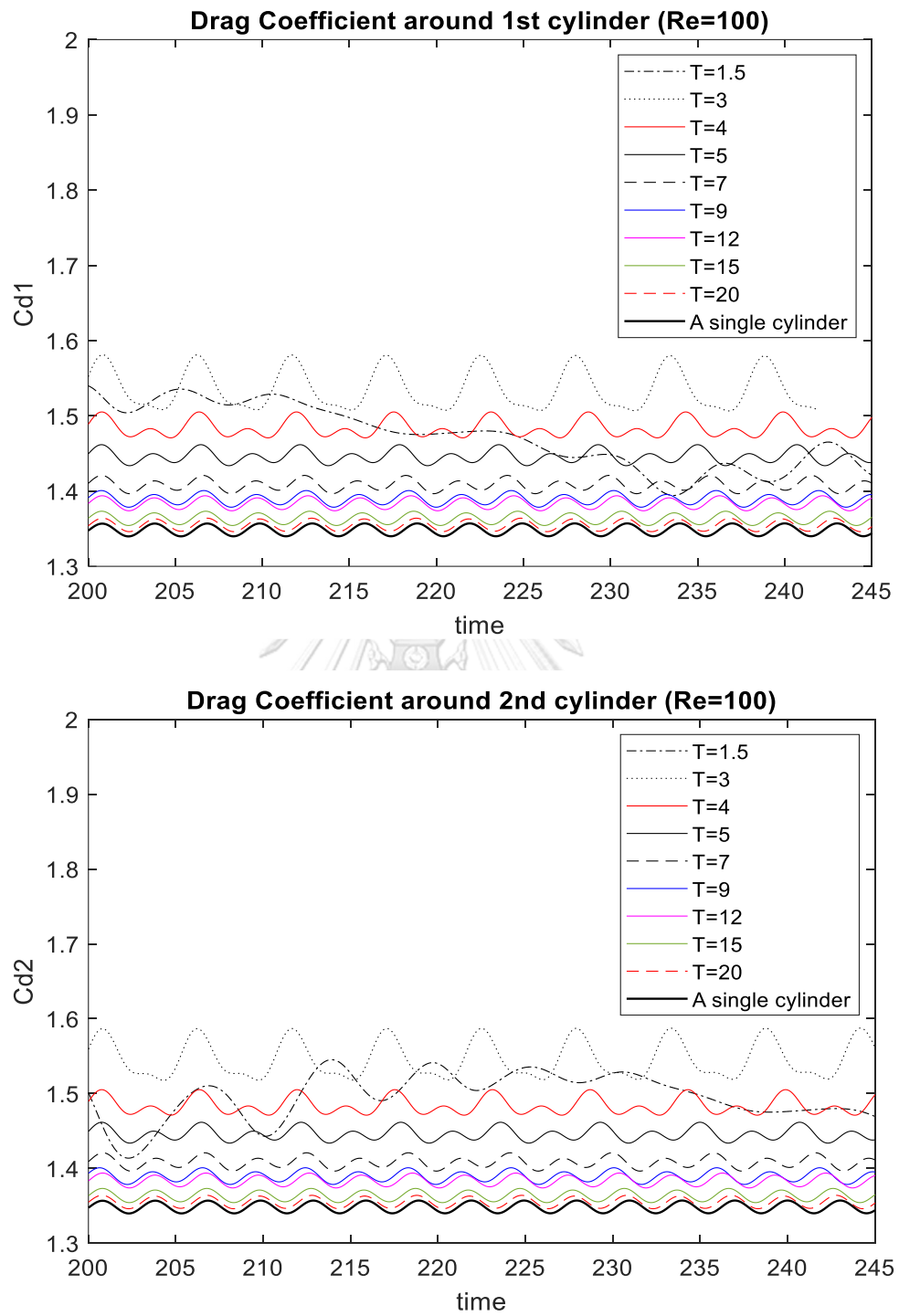


Figure 50 Drag coefficient ( $C_d$ ) with time around 1<sup>st</sup> and 2<sup>nd</sup> side-by-side circular cylinders at  $Re=100$

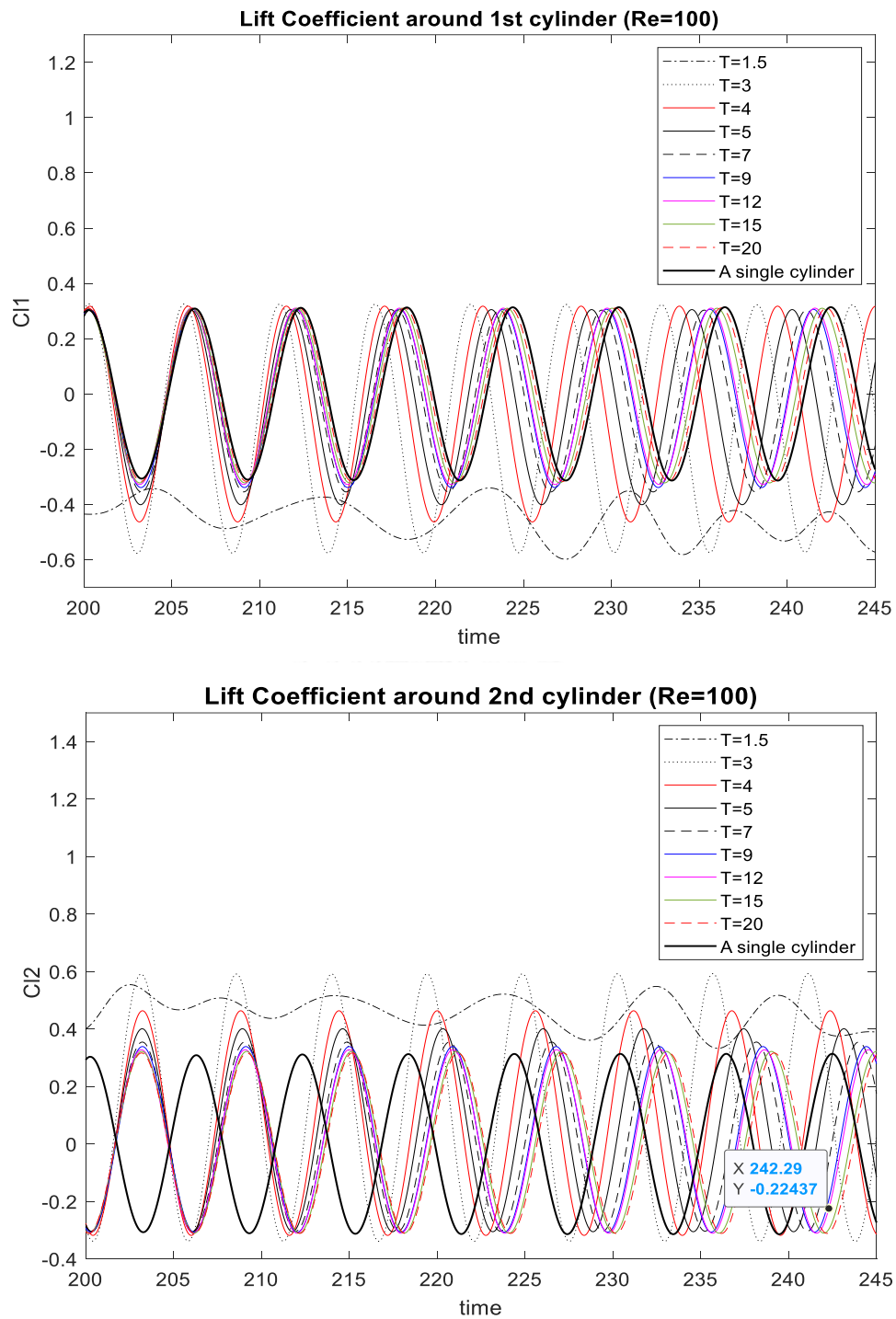


Figure 51 Lift coefficient ( $C_l$ ) with time around 1<sup>st</sup> and 2<sup>nd</sup> side-by-side circular cylinders at  $Re=100$

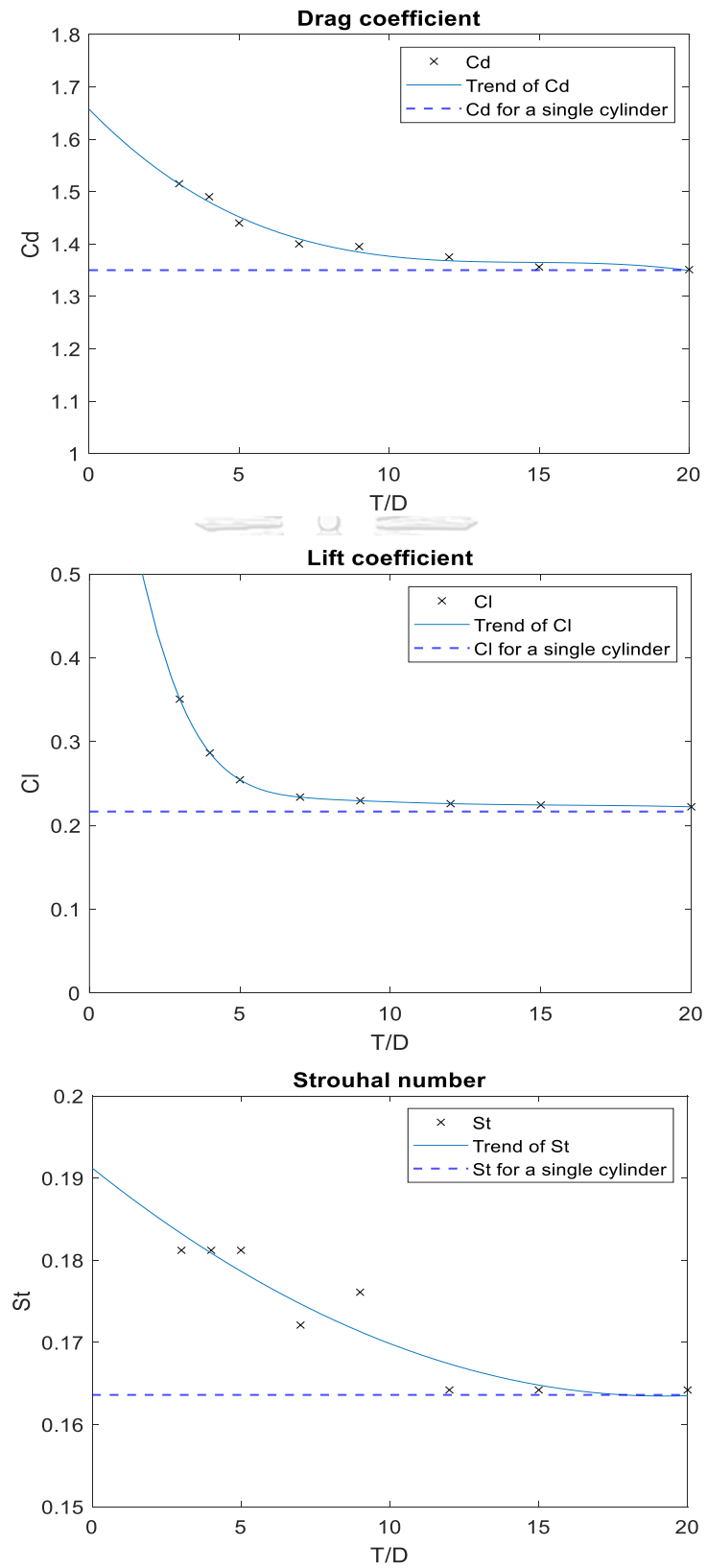


Figure 52 Results compared with a single cylinder at  $Re=100$

## CHAPTER 5

### RESULTS

From the prior part of result, we studied the behavior of computational flow past a stationary cylinder and the resultant force coefficient (drag and lift) on the cylinder at low Reynolds. Additionally, the study included a pair of pair of cylinders placed side-by-side with varying the transverse gap (the space between cylinder). In these simulations, we found out that the resultant force coefficient of each cylinder and the characteristic frequency of flows were influenced by the transverse gap. The result of force coefficient increased when the cylinders are closer to each other. On the other hand, the result decreased and converged to values of flow past a single cylinder as expansion of the transverse gap between cylinders.

In this part, the geometrical configurations of the arrangement are more resemble to what is used in the real world. The geometry of arrays of cylinders are designed to mimic the breakwater made of bamboo, called bamboo-fencing, along the muddy shoreline in front of the Gulf of Thailand. The detail of blueprints of bamboo-fencing in figure 7 and figure 8 from the department of marine and coastal resources (DMCR), built for prevention of coastal erosion. The geometrical configurations of array of cylinders in our study are categorized into 2 types, 1) staggered and 2) aligned arrangement.

#### 5.1 Mesh

The set of simulations for arrays of cylinder is conducted on a computational domain of size  $H=30D$  (height) and  $L=45D$  (length), shown in Figure 53 (a). The number of meshes is approximately 800,000 to 2,000,000, depending on the amount of cylinders. However, meshes are clustered around the surface of cylinders to capture boundary layers. The details of mesh for both arrangements are shown figure

53 (b) and 53 (c). The Reynolds is set for 100 at time step size of 0.01 for all cases. In this part, the all-time result is counted in steady time of flow that the time begins at  $t=0$ .

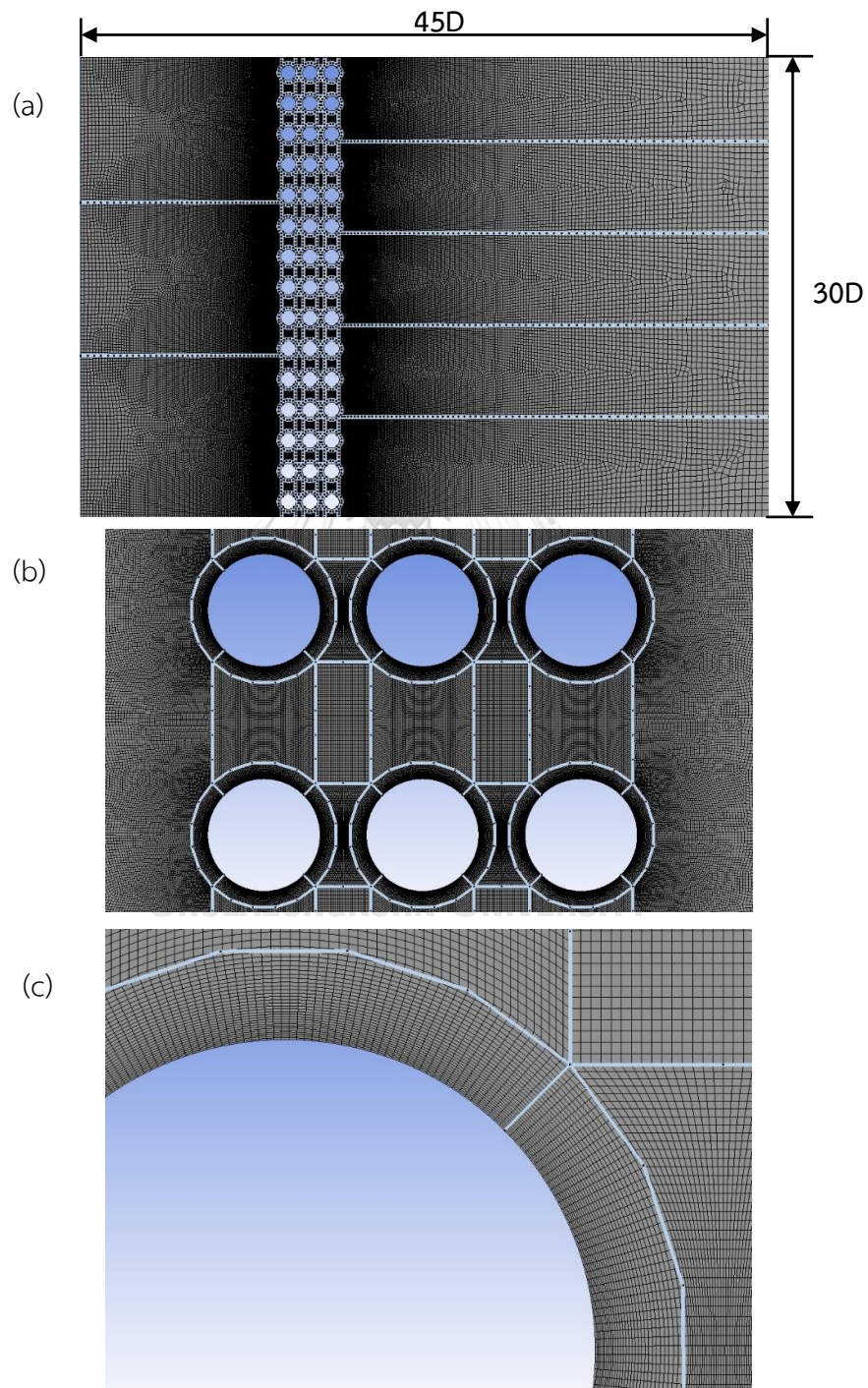


Figure 53 Computational domain: (a) full domain, (b) zoom-in, (c) near-cylinder

## 5.2 Comparison: Staggered and aligned arrangements

### 5.2.1 Velocity vector

The figure 54-56 show velocity vector of the bundle of cylinders, which depict the curling velocity of flow, for staggered and aligned arrangements. It is observed that the staggered arrangement induces significant changes in the arrangement of the vectors after flow past cylinders. The appearance of curl of velocity vector is not difference when columns of cylinders are added. It is quite clear that the additional columns do not significantly affect to the vortex behind cylinders in both arrangements.

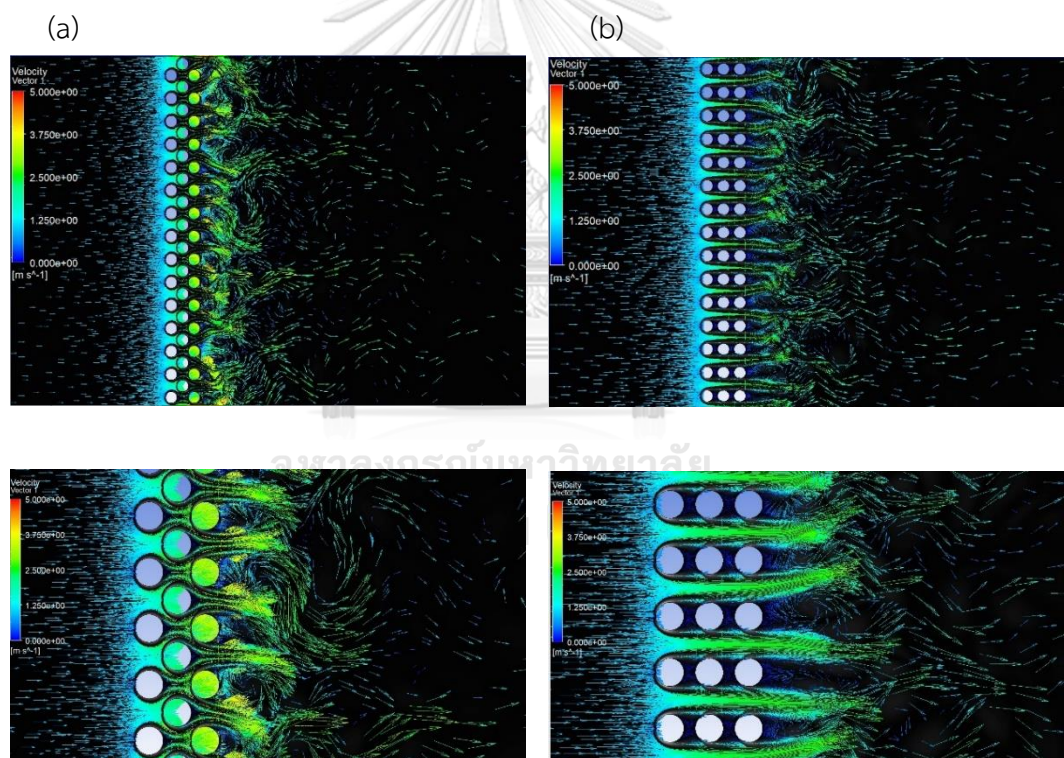


Figure 54 Vorticity for 3 columns of array: (a) staggered arrangement (Top) and zoom-in (bottom), (b) aligned arrangement (Top) and zoom-in (bottom)



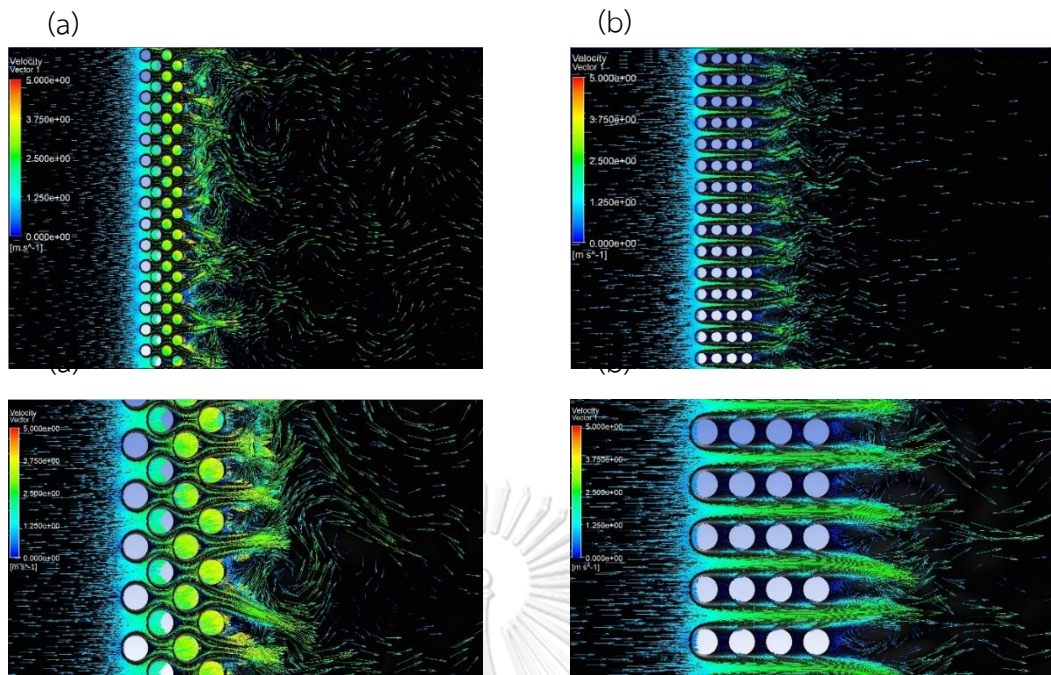


Figure 55 Vorticity for 4 columns of array: (a) staggered arrangement (Top) and zoom-in (bottom), (b) aligned arrangement (Top) and zoom-in (bottom)

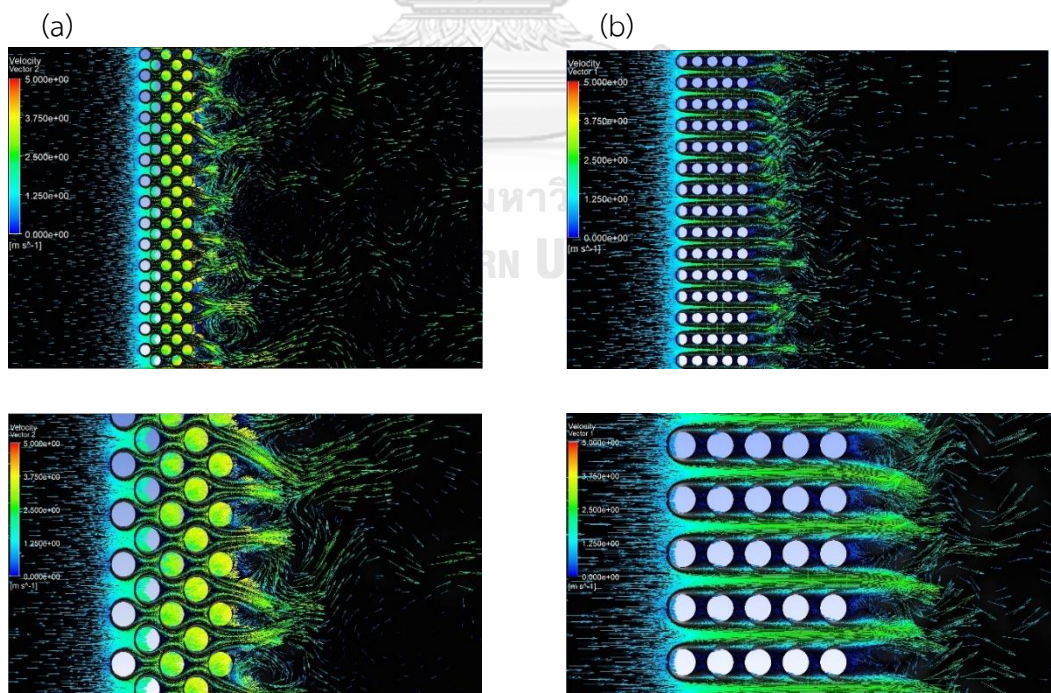


Figure 56 Vorticity for 5 columns of array: (a) staggered arrangement (Top) and zoom-in (bottom), (b) aligned arrangement (Top) and zoom-in (bottom)

## 5.2.2 Drag coefficient and drag force

### 5.2.2.1 Drag coefficient on a cylinder

The column number indicator in the arrays of cylinders for both types of arrangement are ordered from left to right, indicated as shown in figure 57.

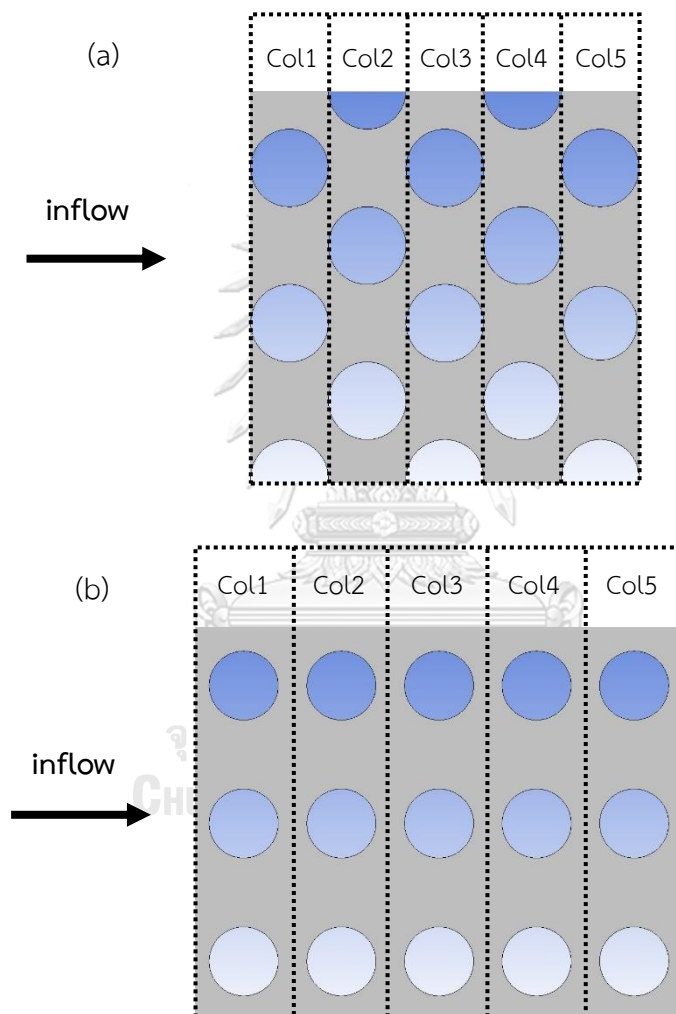


Figure 57 Order of columns: (a) staggered arrangement, (b) aligned arrangement



From table 8, the drag coefficient,  $C_d$  in short term, is drag force normalized with dynamic pressure and project area that  $C_d$  is overwhelmingly larger than that of the flow past a single cylinder or a pair of cylinders that we presented previously on preliminary results because in this part, the group of cylinders are placed tightly, and top and bottom boundary of domain are set as periodic condition. So, the tightened group of cylinders obtains high pressure and it gains large drag force on a cylinder. The drag coefficients on cylinders are different for each column of the same arrangement. The coefficients of cylinders at the same column number on the two arrangements differ. As the two arrangement patterns are designed such that each row is simply a spanwise replicate of one another,  $C_d$  on cylinders for each row should theoretically be identical. This is also the case, shown in table 8.

According to table 8, The drag coefficient of each cylinder from staggered arrangement is much higher than the values from the aligned one in overall. In the staggered arrangement, the drag coefficients of all columns except the last are interestingly of similar values. The  $C_d$  of the last column of cylinders is significantly smaller than those in their front. The reason of it being so is the inexistence of a body that obstructs wake formation in the rear, allowing the existence of the low-pressure region in the wake.

In terms of the aligned arrangement, the table shows that the time-averaged drag coefficient is markedly large only for the first column. The coefficients drop onward from the next columns and stay in the same range. This is because the cylinders in first column operates themselves as the barriers for the others at their back. It is clear from the results in figure 58 in which it shows the time-averaged drag coefficient for the two types of arrangement with respect to the number of columns. Figure 59 shows the drag coefficients with time. Although, cylinders are supplemented in the horizontal direction for 1 or 2 more columns, there is no massive difference of drag coefficient on cylinders added in the arrangement of

aligned type. On the other hand, the drag coefficients from each cylinder in staggered type stay in the same range even if more column is added.

Table 8 Drag coefficient from cylinder in each column

Type of arrangement	No. of column	Drag Coefficient ( $C_d$ )				
		Column 1	Column 2	Column 3	Column 4	Column 5
Staggered	3	8.3803	8.3855	5.1221	-	-
aligned		4.4197	1.2636	1.076	-	-
Staggered	4	8.5133	8.5264	8.6540	5.7341	-
aligned		4.4306	1.3063	1.2964	1.3804	-
Staggered	5	8.4685	8.4534	8.6798	8.5669	5.4880
aligned		4.4198	1.3084	1.2978	1.2131	1.1729

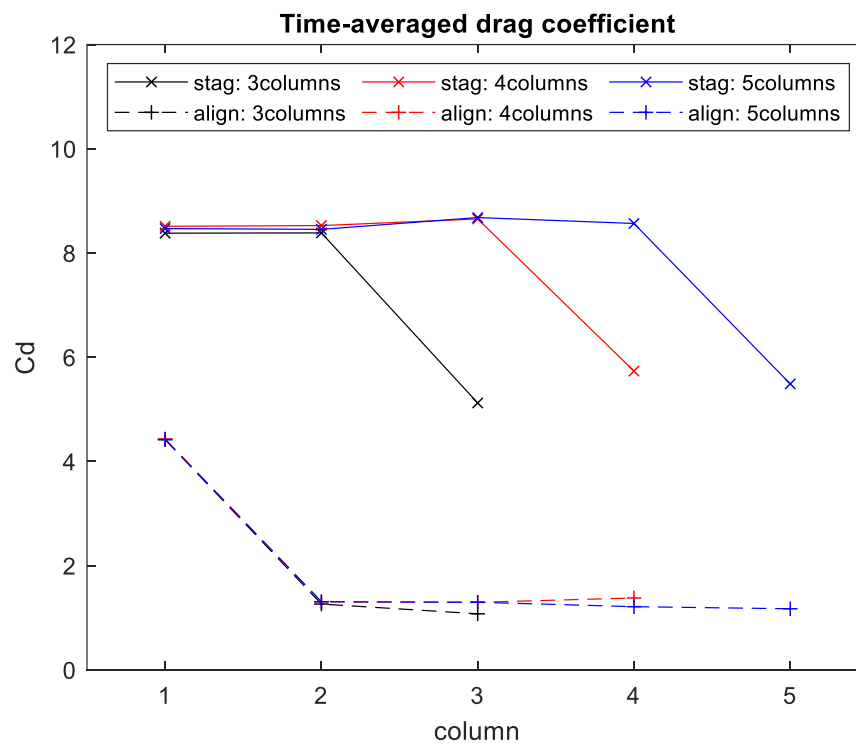
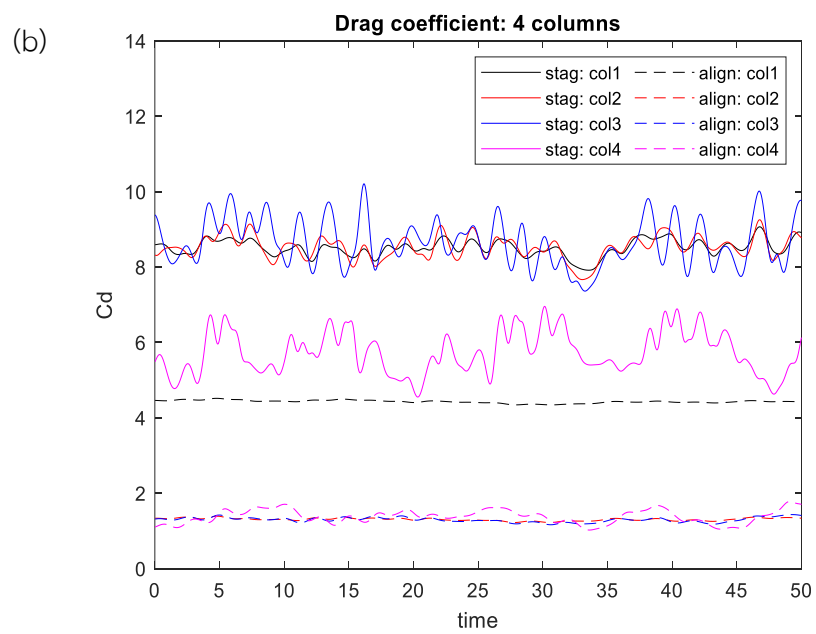
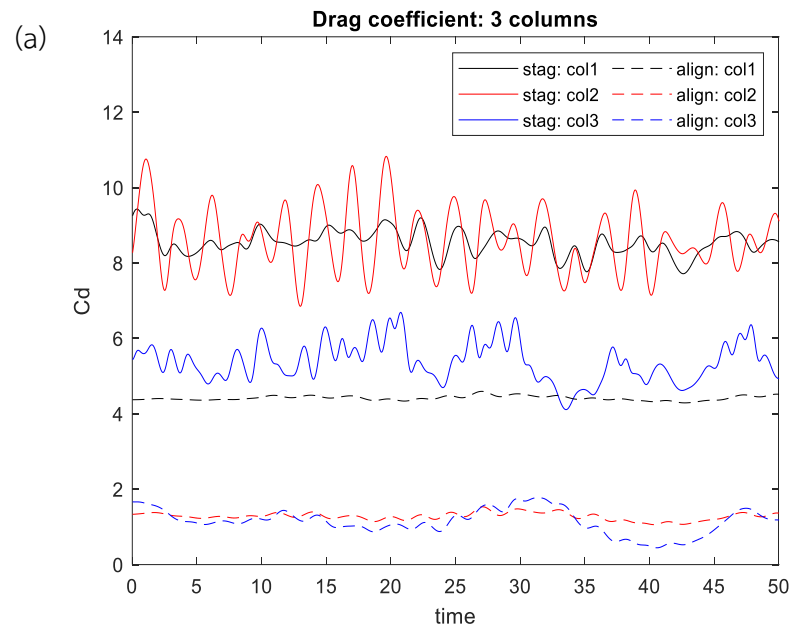


Figure 58 Time-averaged drag coefficient for each cylinder



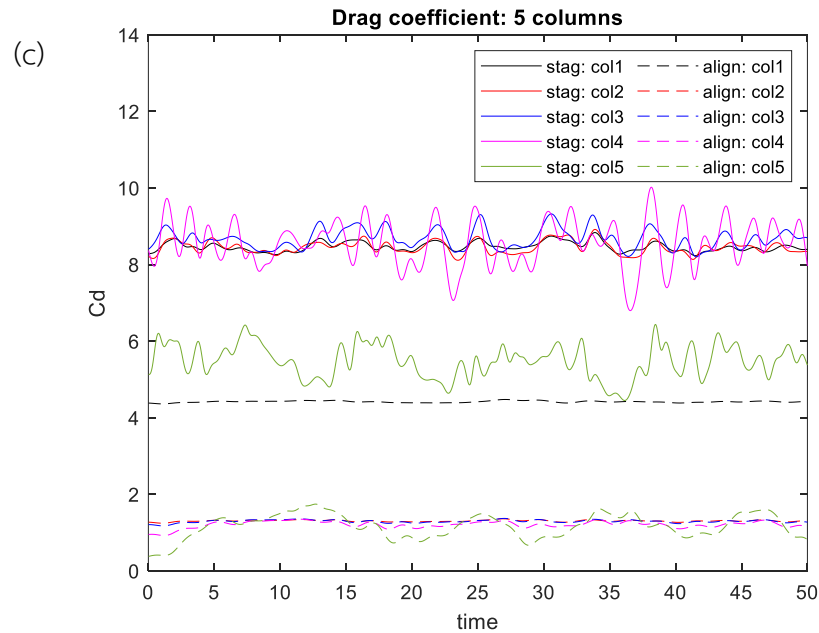


Figure 59 Drag coefficient ( $C_d$ ) with time on cylinders for each column, both arrangement: (a) 3 columns, (b) 4 columns, (c) 5 columns

#### 5.2.2.2 Drag force

Summation of drag forces on all the cylinders plotted with respect to time for staggered and aligned arrangements are shown as figure 60. The staggered arrangement experiences drag force much larger than the aligned case. The aligned type with additional 1 or 2 columns does not experience significantly higher summation of drag force.

Figure 61 shows the time-averaged summation of drag force for both arrangements. It insists that the staggered type produces approximately 3 times, 3.75 times and 4.2 times larger drag force than aligned type in 3 columns, 4 columns and 5 columns respectively. It can be seen from the slope of the fitting lines that additional added columns for staggered type have a larger effect on the summation

of drag force than the aligned configuration. Practically due to the larger drag force, the cylinders of staggered arrangement must relatively be more durable.

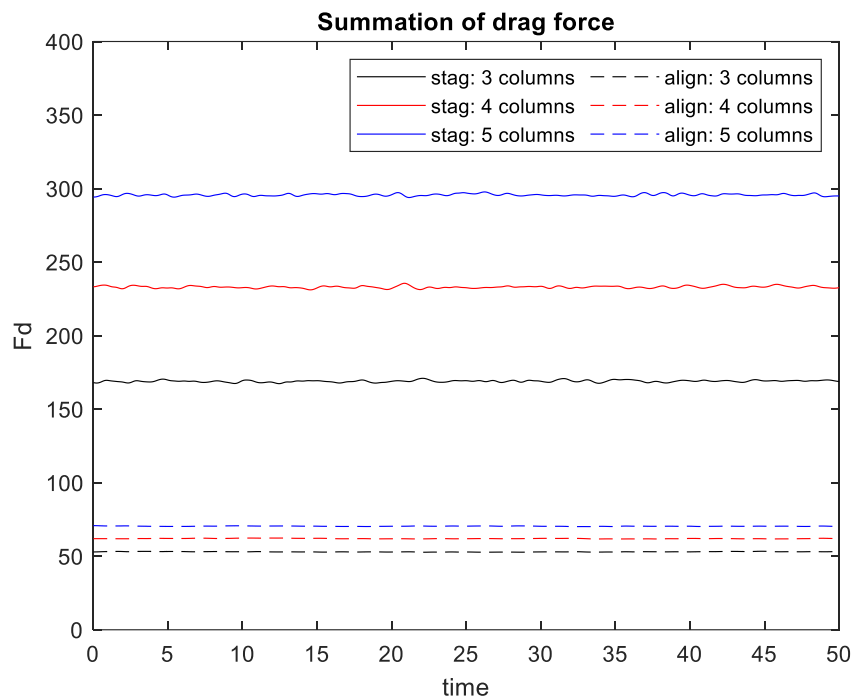


Figure 60 Summation of drag force with time

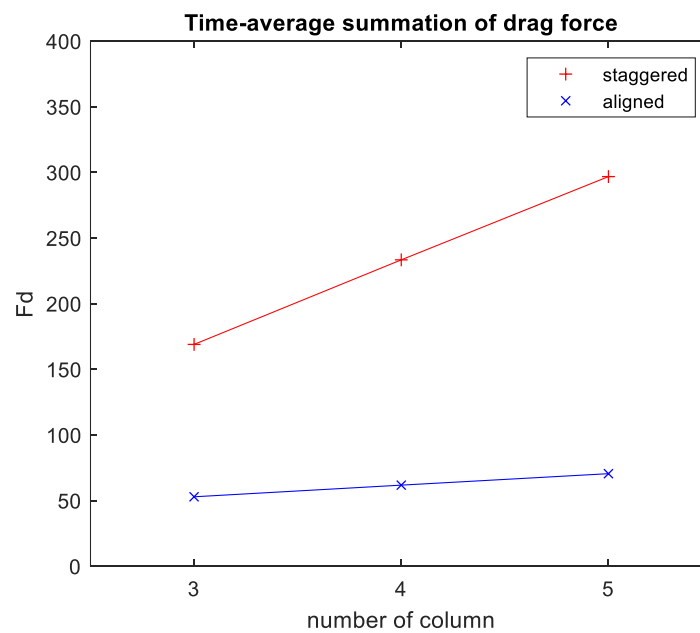


Figure 61 Time-averaged summation of drag force

### 5.2.3 Pressure

In the previous section, the summation of drag force and drag coefficient on a cylinder are considered for the two types of arrangement. In this part, the property of fluid flow in terms of pressure, while briefly discussed previously, will be investigated. In particular, we consider the distribution of pressure field, with the emphasis on the difference between that in the computational domain inlet and at the outlet.

#### 5.2.3.1 Pressure contour

Figure 62-64, show pressure contours of the 3, 4 and 5 columns respectively, of the staggered and aligned arrangements at instantaneous time = 50.00. The pressure drop, along the streamwise direction, is established in all of the arrangements during the period of consideration (steady state). From here on, unless otherwise stated, the word ‘pressure drop’ refers to the difference of pressures at the inlet and at the outlet. The pressure drop from staggered arrangement is much higher than that of the aligned arrangements in any number of columns. From the visualization (fig. 50-52), field pressure is decreased largely across the group of bodies.

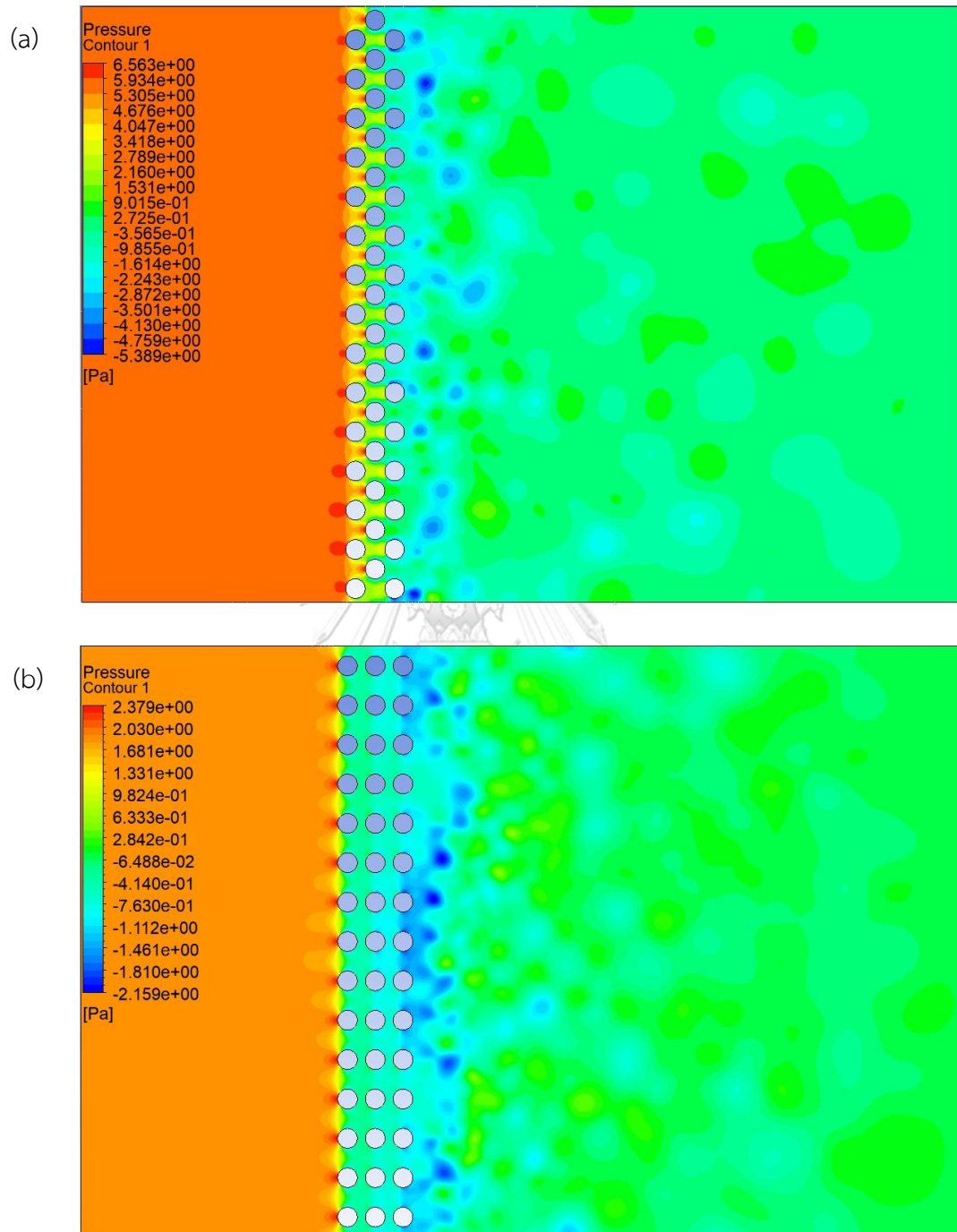


Figure 62 Pressure contour  $t = 50.00$ , 3 columns: (a) staggered, (b) aligned

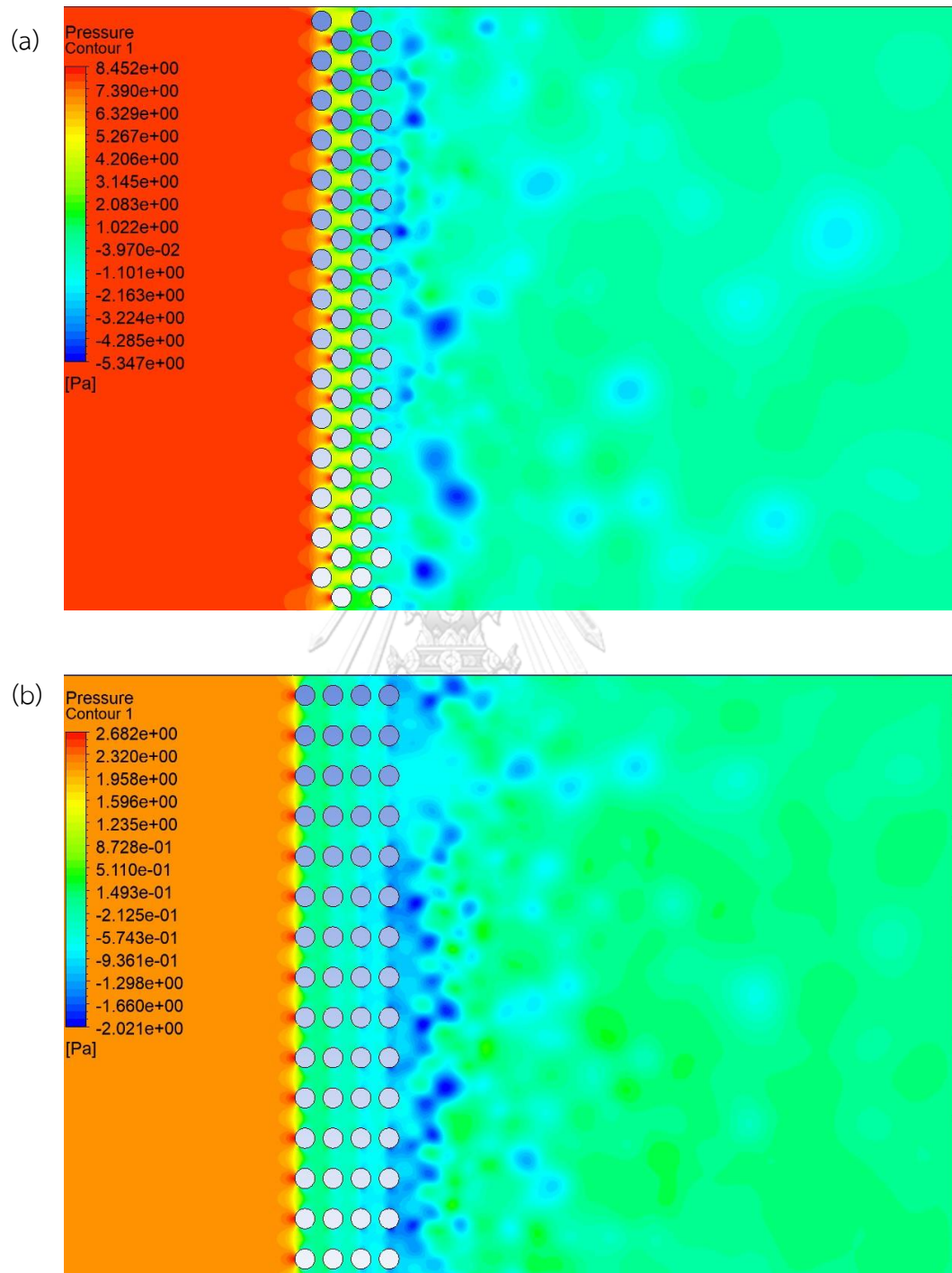


Figure 63 Pressure contour  $t = 50.00$ , 4 columns: (a) staggered, (b) aligned



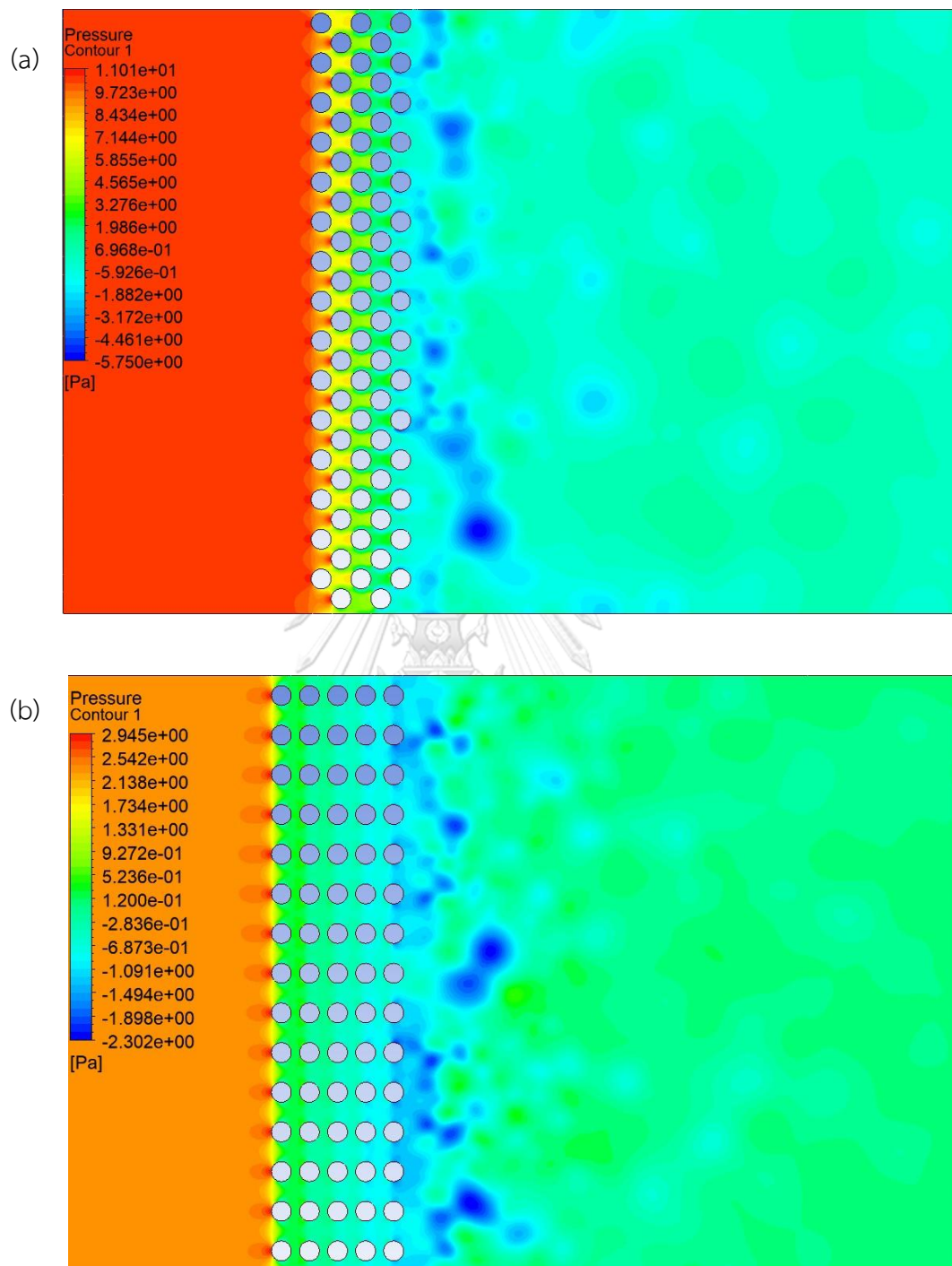


Figure 64 Pressure contour at  $t= 50.00$ , 5 columns: (a) staggered, (b) aligned

The coordinate is set that the line,  $y=0$  is on the middle of domain in horizontal axis and the line,  $x=0$  is across the center points of cylinders from last column, shown in figure 67. From here, we consider instantaneous pressure distribution in the streamwise direction plotted along the horizontal lines across the domain at  $y= -0.5$  (slightly below the middle of the domain to avoid the presence of cylinders), shown in figure 65. From figure 66, the pressure has dropped significantly across the group of cylinders. The pressure drop from staggered arrangement is much more than the aligned type.

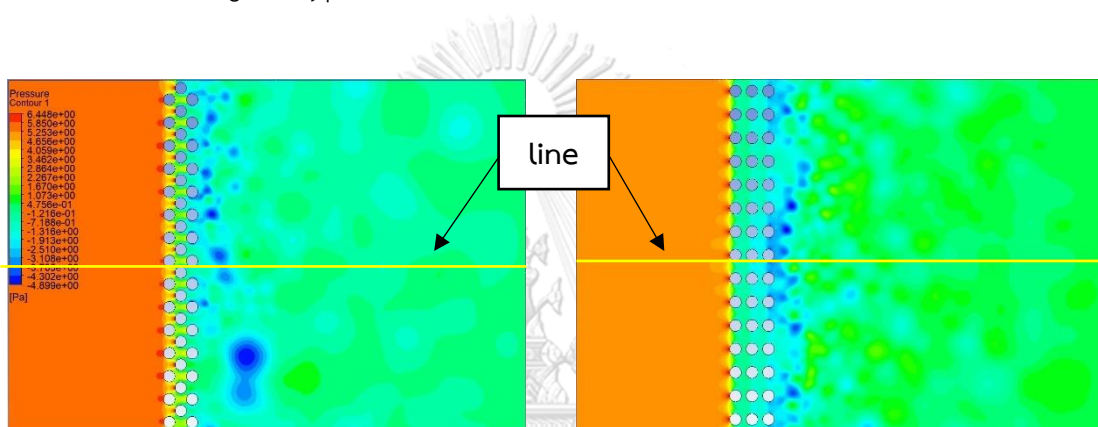
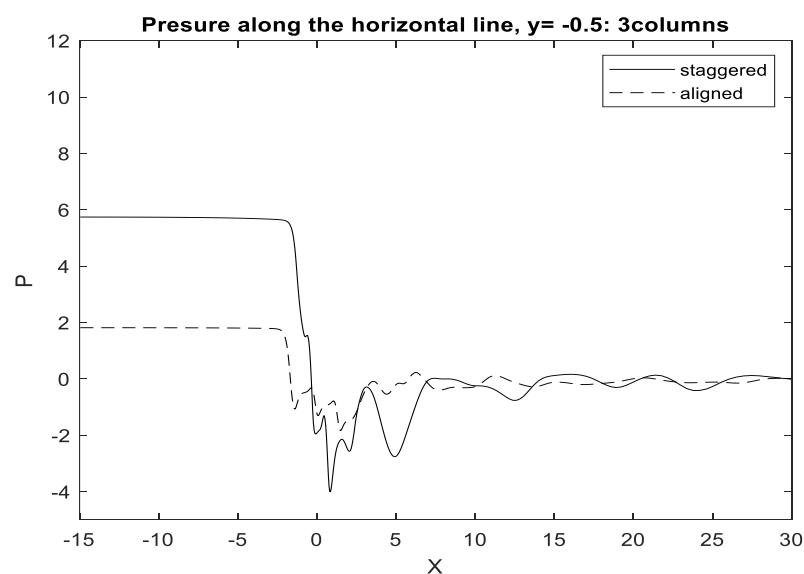


Figure 65 Pressure contour at  $t= 50.00$  with horizontal line  $y= -0.5$



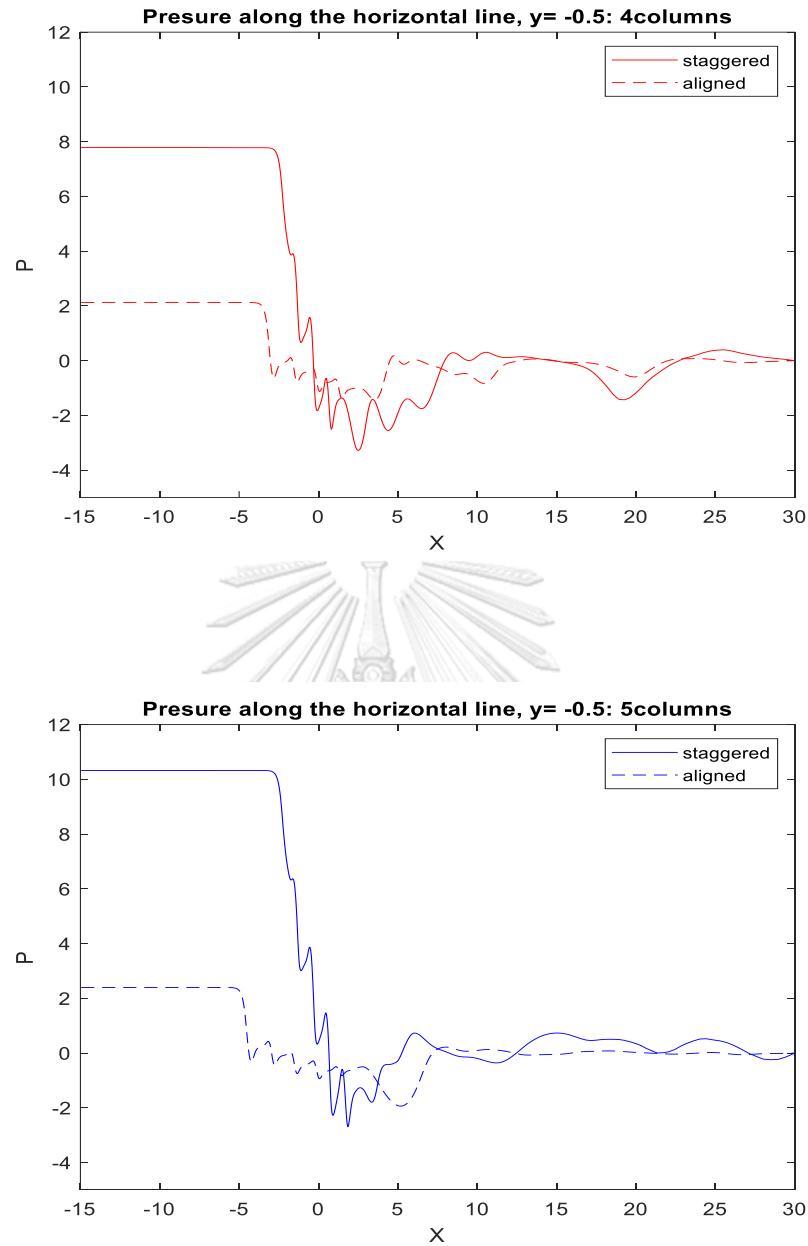


Figure 66 Pressure at  $t= 50.00$  along the horizontal line  $y=- 0.5$

### 5.2.3.2 Area-weighted averaged pressure

Averaged pressure in the entire spanwise ( $y$ ) direction is considered. It is done simply by taking the summation of pressure (at an instance of time, in this context) on a specified area (in the  $x$ - $z$  plane, given that the domain depth is 1) divided by that total area. In our study, consider the averaged pressure across the 9 particular spanwise at  $x=-10$  (inlet), 0.5, 1, 1.5, 2.5, 5, 10, 15 and 25 on the computational

domain. The area-weighted average pressure will be calculated over these lines. The reference line ( $x=0$ ) is shown in figure 67.

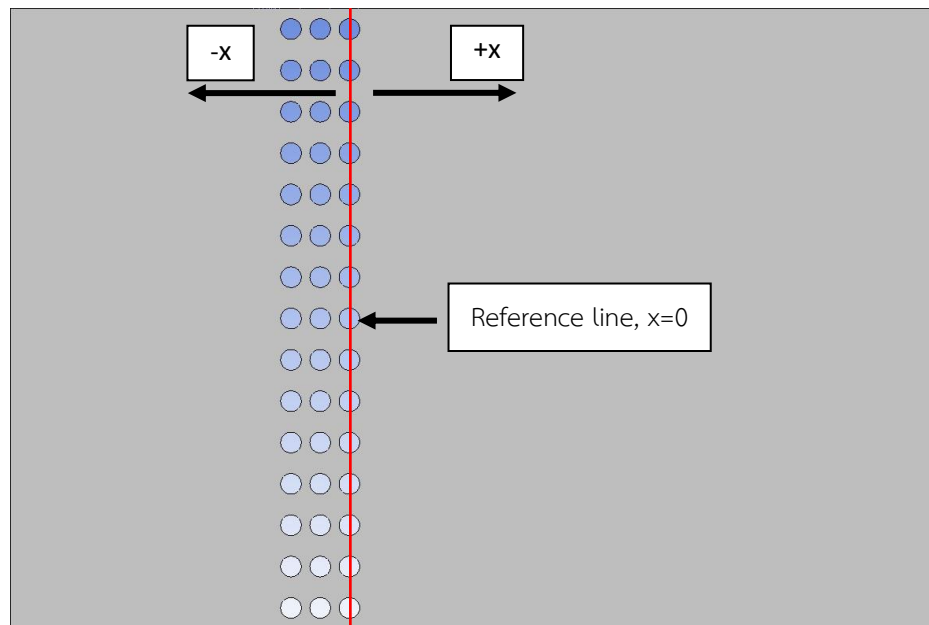


Figure 67 The domain with reference line

The results of area-weighted average pressure are shown figure 68, 69 and 70. As can be deduced, the distribution of spanwise-averaged instantaneous pressure is expected to be similar to what is shown in the previous subsection, albeit a 'smoother version'. Pressure is relatively high in the front, experience a significant drop across the cylinder, and reaches the Dirichlet condition ( $P=0$ ) at the domain exit.

For the staggered arrangement, pressure on inlet side are approximately 6 for the 3-column, 8 for the 4-columns and 10 for the 5-column arrangements. The results in aligned type are approximately 1.8, 2.1 and 2.4 for 3, 4 and 5 columns respectively. The minimum pressure is found just behind the last column of cylinder, measured to be almost -2 in staggered type and -1 in aligned type (see Fig. 56).

Again, the pressure gradually recovers toward the Dirichlet outlet condition at  $P=0$  for both of the arrangements.

The staggered arrangement experiences larger pressure drop than aligned arrangement. For columns added, pressure drop from staggered type are almost 4 times higher than aligned type for 4 columns and it increases to 5 times higher for 5 columns.

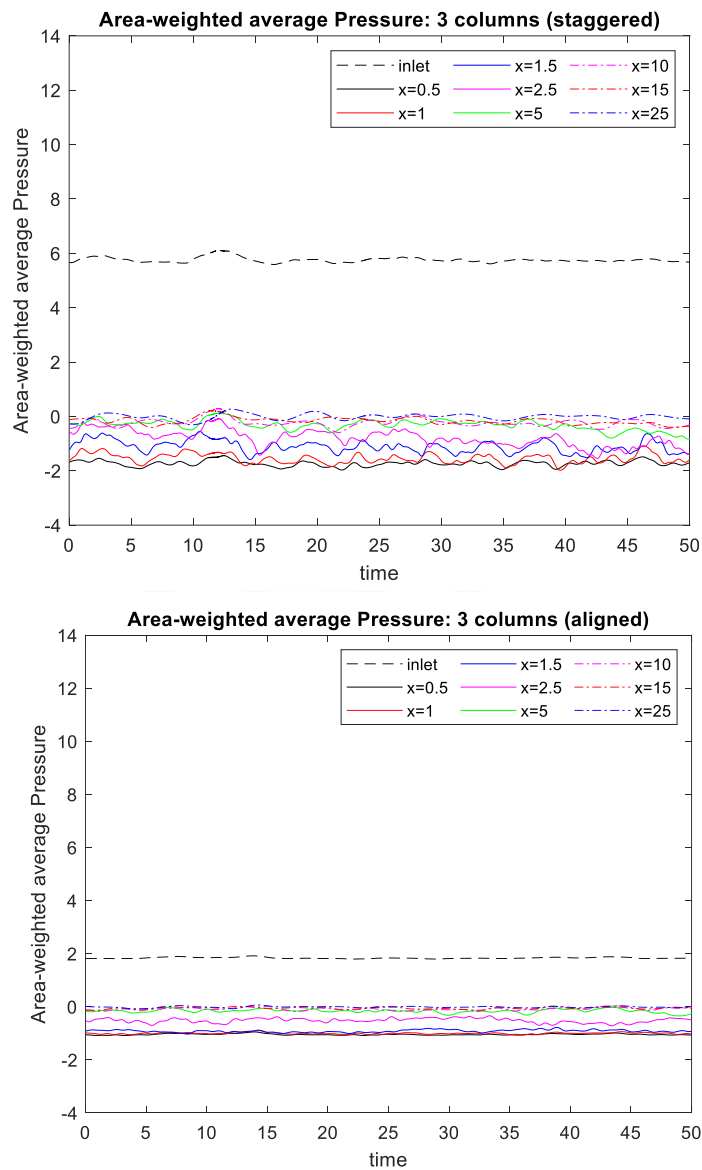


Figure 68 Area-weighted average pressure for 3 columns: staggered arrangement (top), aligned arrangement (bottom)

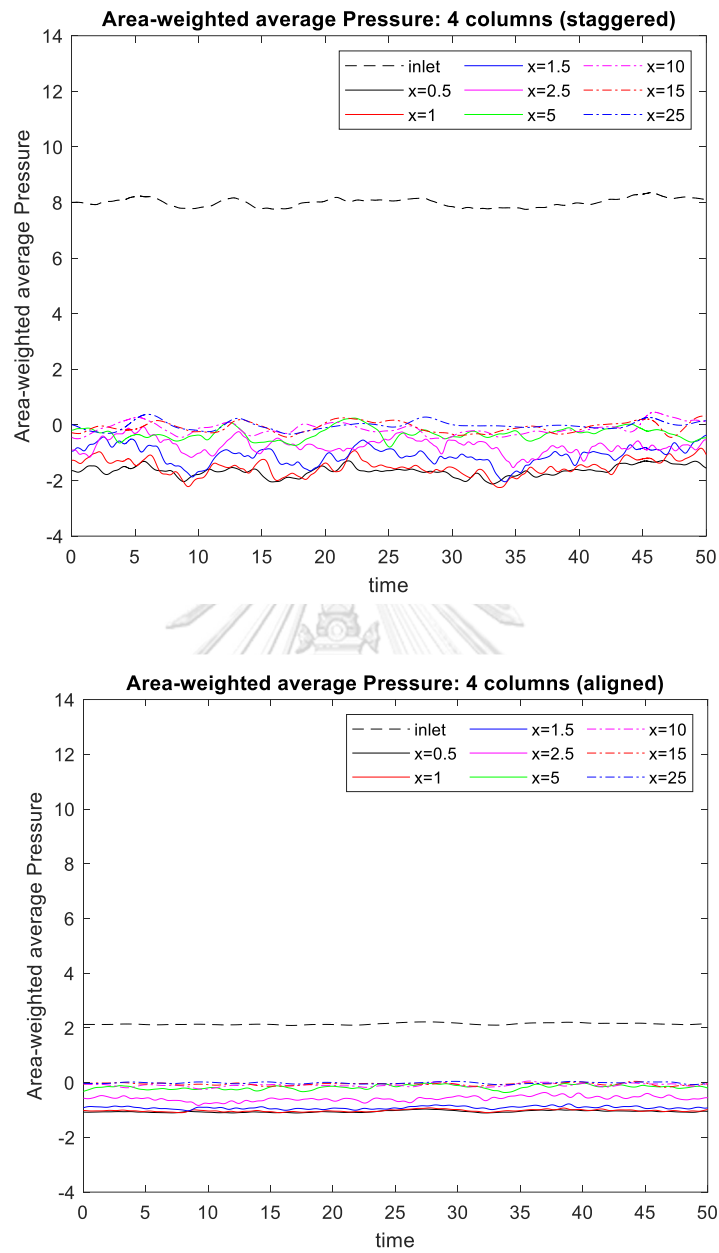


Figure 69 Area-weighted average pressure for 4 columns: staggered arrangement (top), aligned arrangement (bottom)

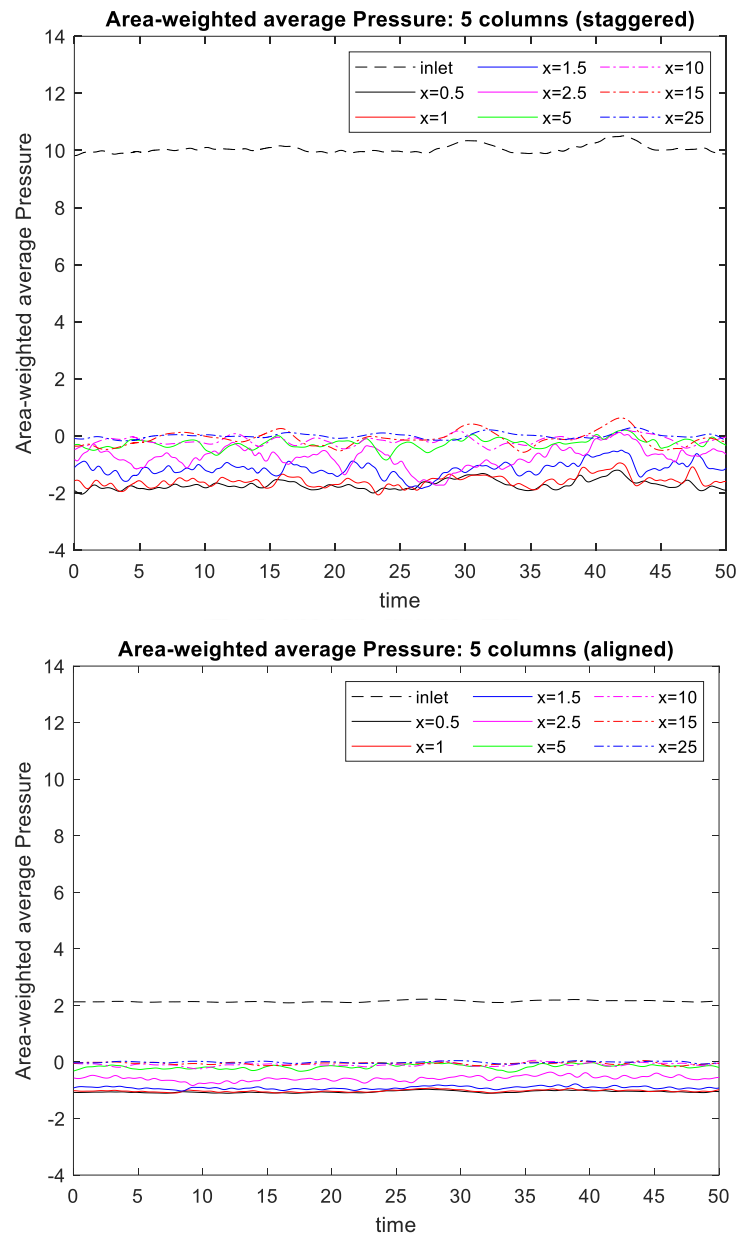


Figure 70 Area-weighted average pressure for 5 columns: staggered arrangement (top), aligned arrangement (bottom)

Additional post-processing is done to average the previous, area-weighted, averaged pressure in time. This shows in figure 71. An array of cylinders in staggered arrangement is better at pressure reduction than aligned arrangement. The larger in pressure reduction is observed across cylinders ( $x \leq 0$ ), where the staggered type does not restrict the existence of cylinder's wake; unlike the aligned arrangement. The region behind body (wake) is of relatively lower pressure with respect to cylinder's frontal flow area, thus promotes the pressure drag.

The additional averaging in time (figure 71) provides a clearer picture than that of the instantaneous time (figure 67).

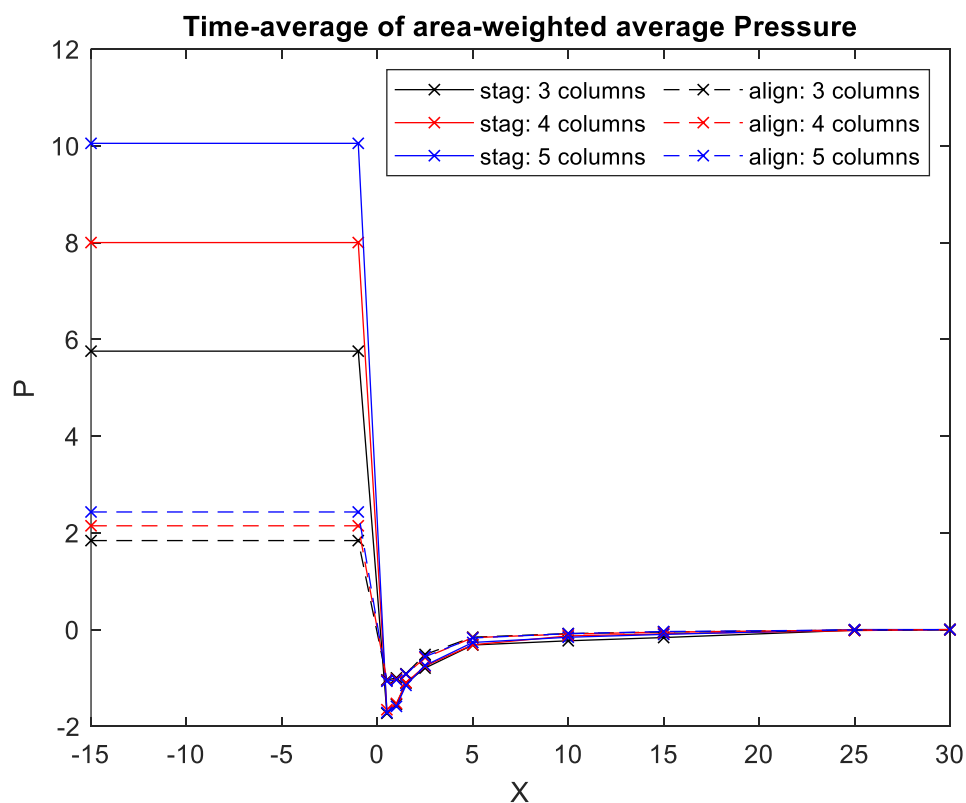


Figure 71 Time-average of area-weighted average pressure



Figure 72 shows the time-averaged pressure drop, inlet-outlet pressure difference, for both arrangements. The staggered type gains larger pressure drop than aligned one. From the slope of the fitting lines, additional columns for staggered type have the larger effect of pressure reduction than aligned arrangement. Figure 72 is similar to figure 61 which shows average of drag force.

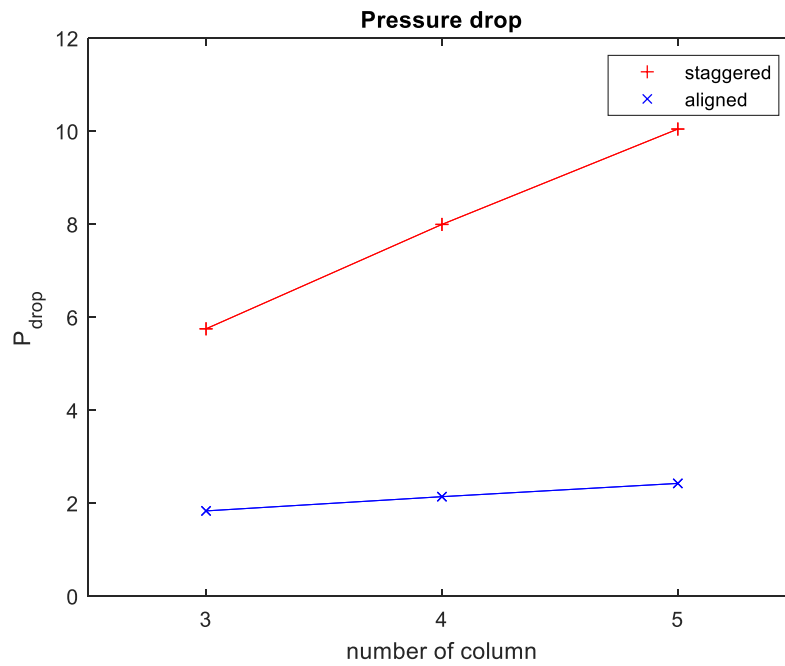


Figure 72 Pressure drop across the computational domain

#### 5.2.4 Relation of drag force and pressure

The equation (21) from chapter 2 explains the energy equation applied with first law of thermodynamics and Bernoulli equation, shown below:

$$\frac{p_{out}}{\rho} + \frac{v_{out}^2}{2} + gz_{out} = \frac{p_{in}}{\rho} + \frac{v_{in}^2}{2} + gz_{in} + \dot{w}_{int} \quad (38)$$

Consider the equation (38) in its temporal-average form. In our simulation of array of cylinders conducted in the horizontal plane, the potential energy term of

equation,  $g(z_{out}-z_{in})$ , is zero. The inlet velocity and outlet velocity are on average in time and space, identical due to the conservation of mass. Thus,  $(v_{out}^2-v_{in}^2)/2$ , is theoretically zero. The equation is rearranged as:

$$\frac{p_{out}}{\rho} - \frac{p_{in}}{\rho} = \dot{w}_{int} \quad (39)$$

Since in our boundary condition, there is no wall friction because the top and bottom boundaries are set as periodic. Therefore, the internal work,  $\dot{w}_{int}$ , only occurs as a result of drag force ( $F_d$ ) that cylinders act on the fluid. So, the equation above can be rewritten as:

$$\dot{w}_{int} = \frac{F_d}{A\rho} \quad (40)$$

Where  $A$  is the entire cross-sectional area ( $A = lD$ )  
 $l$  is the domain width  
 $D$  is the domain depth ( $D = 1$ )

The relation of pressure and drag force is:

$$p_{out} - p_{in} = \frac{F_d}{l} \quad (41)$$

The relation of drag force and pressure can be written as the equation (41). Our result is presented for both, summation of drag force of cylinders and pressure drop across cylinders. The equation (39) can be used as a guidance to consider if the result is sensible.

In the figure 73, the solid lines show pressure and the dashed lines show the summation of drag force on cylinders: for 3, 4 and 5 columns in staggered and aligned arrangements. According to the figure 74, the resulting pressure drop and the summation of drags align well with respect to equation (41).

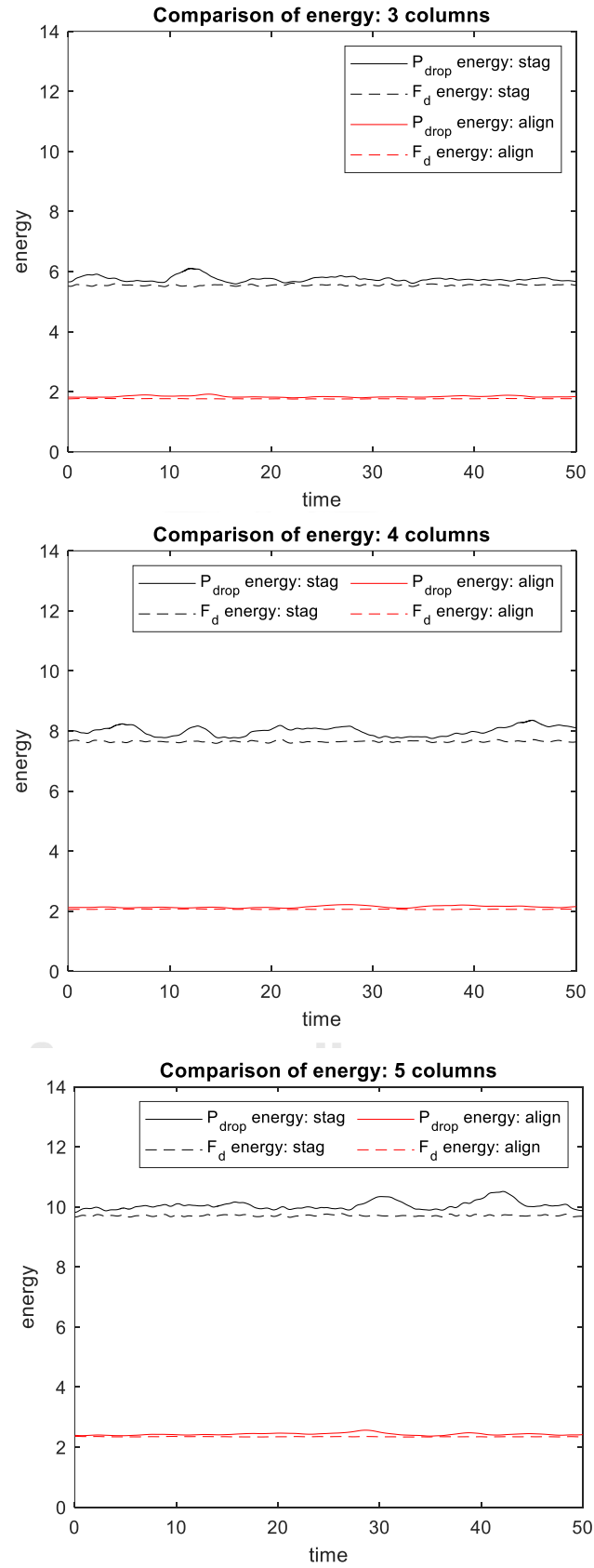


Figure 73 Comparison of energy from pressure drop and drag force

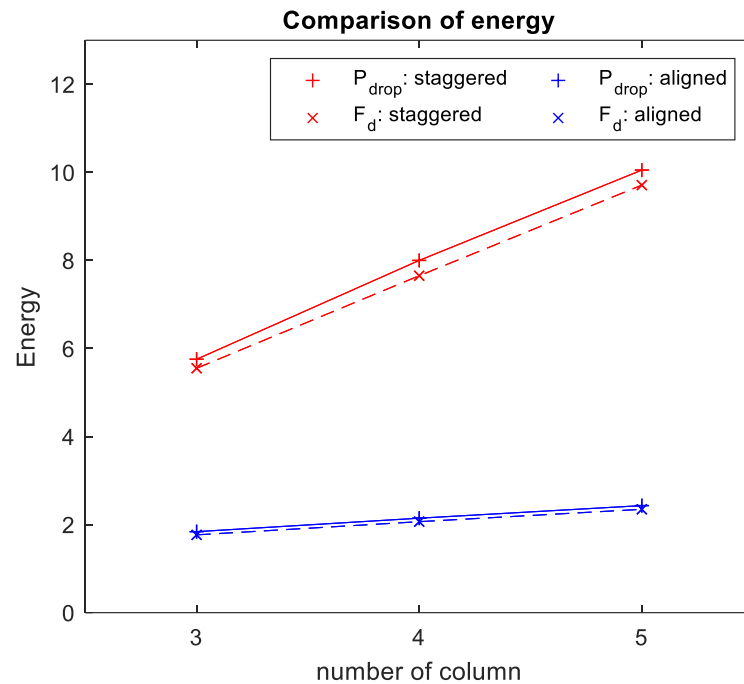


Figure 74 Comparison of time-average energy from pressure drop and drag force

### 5.3 Additional columns for staggered arrangement

The result of previous part confirms the resulting pressure drop and the summation of drags align well with respect to equation 41. Again, the pressure drop and summation of drag force from the staggered arrangement are much higher than aligned arrangement in spite of additional columns.

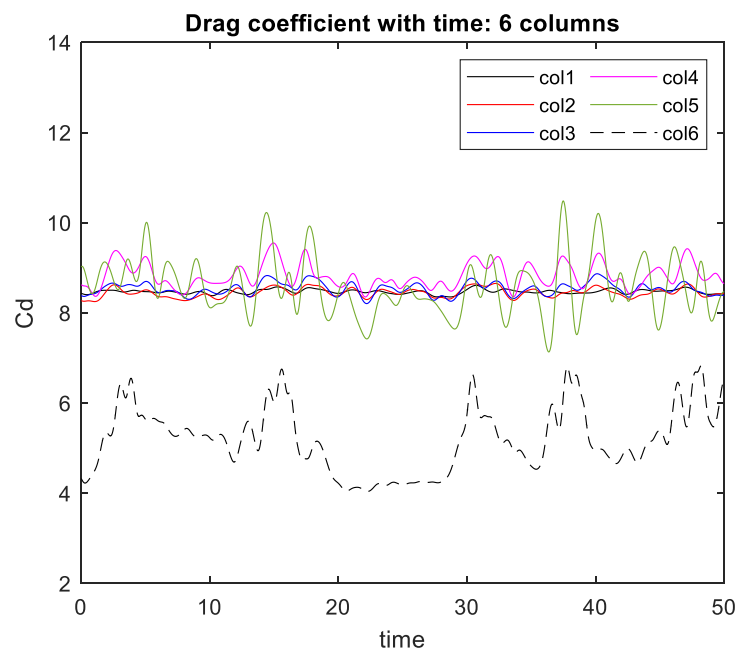
In this section, the numerical simulation of flow past array of cylinder for the staggered arrangement is further performed for additional cylinder columns, up to 13 columns. The numerical simulation is only carried out with the same Reynolds number of 100. The time step and the order of column for staggered arrangement are also set the same as in the previous study.

### 5.3.1 Drag coefficient and drag force

#### 5.3.1.1 Drag coefficient on a cylinder

The effect of additional columns to drag coefficient on a cylinder at various locations in the staggered arrangement are considered. New simulations for the staggered arrangement are done up to 13 columns.

Drag coefficients on a cylinder on each column plotted vs time are shown in figure 75 and 76. The resulting drag coefficient remain in the same range, except the value on the cylinder at last column that drops significantly. The time average of drag coefficient on a cylinder in staggered arrangement for 3 to 13 columns is shown in figure 77. Figure 77 emphasizes the interesting finding where the drag coefficient of the last-column cylinder drops.



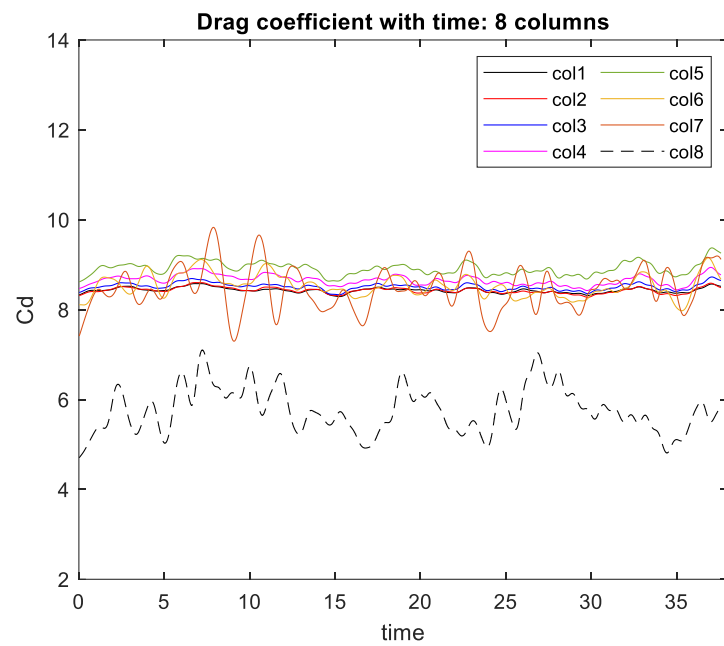
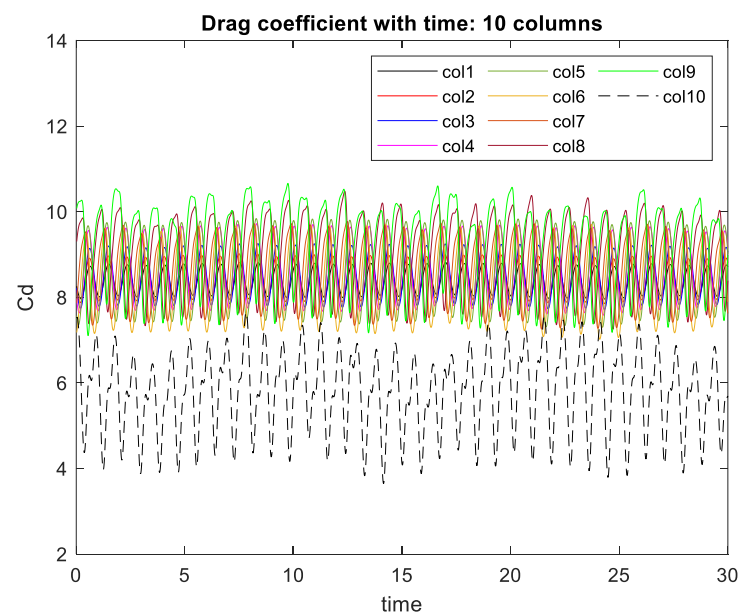


Figure 75 Drag coefficient for each cylinder for 6 and 8 columns



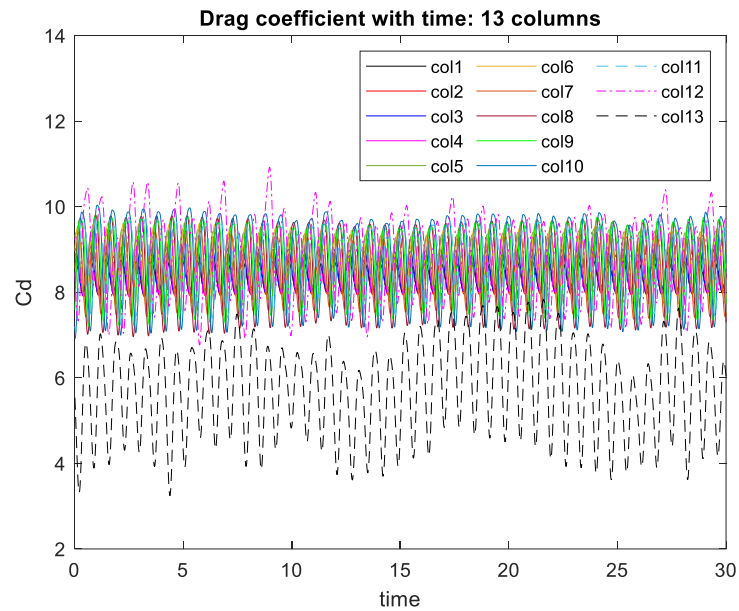


Figure 76 Drag coefficient for each cylinder for 10 and 13 columns

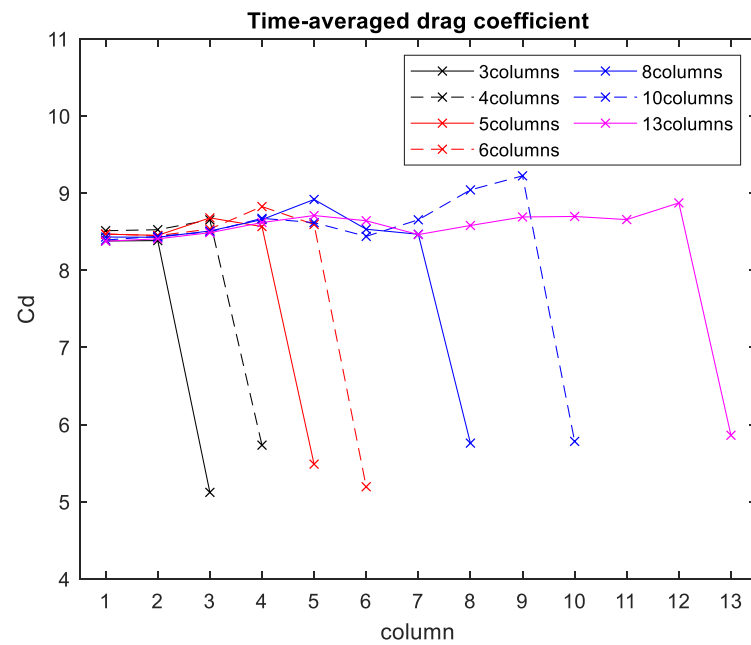


Figure 77 Time-averaged drag coefficient for each cylinder up to 13 columns

### 5.3.1.2 Drag force

Figure 78 shows the summation of drag force with history of time for 3 to 13 columns. The resulting drag remains to be directly proportional to the number of cylinders. The time-averaged summation of drag force from 3 to 13 columns have a trend line as linear line, shown as figure 79.

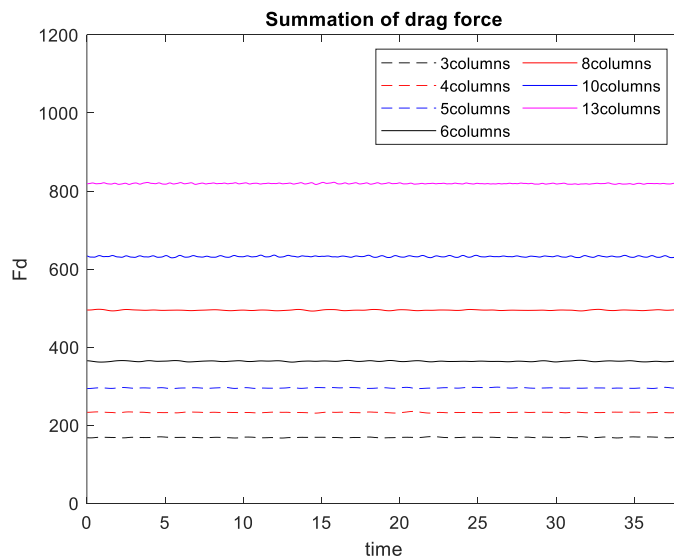


Figure 78 Summation of drag force with time up to 13 columns

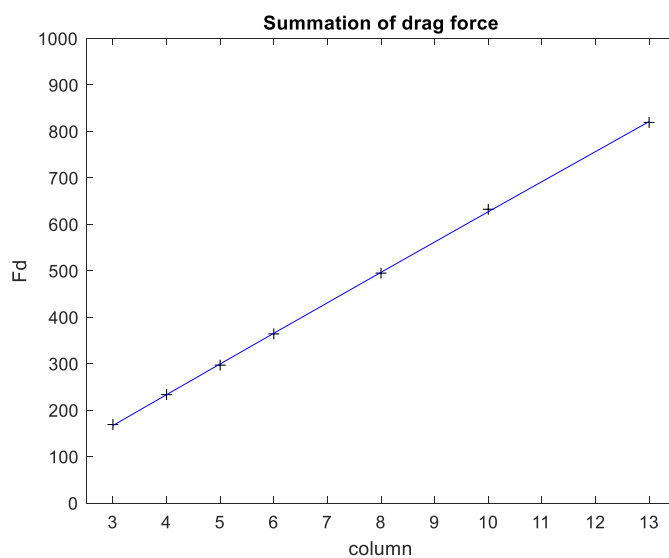


Figure 79 Time-averaged summation of drag force up to 13 columns



### 5.3.2 Pressure

The pressure drop for staggered arrangement is also observed more for 6 to 13 columns. The increasing pressure drop linearly depending on the additional columns, shown in figure 81, same as the summation of drag force (figure 79).

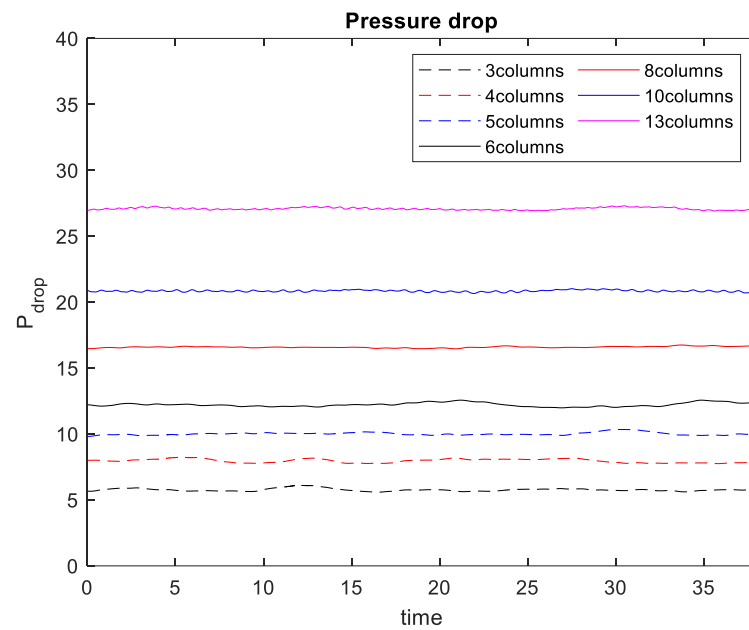


Figure 80 Pressure drop with time up to 13 columns

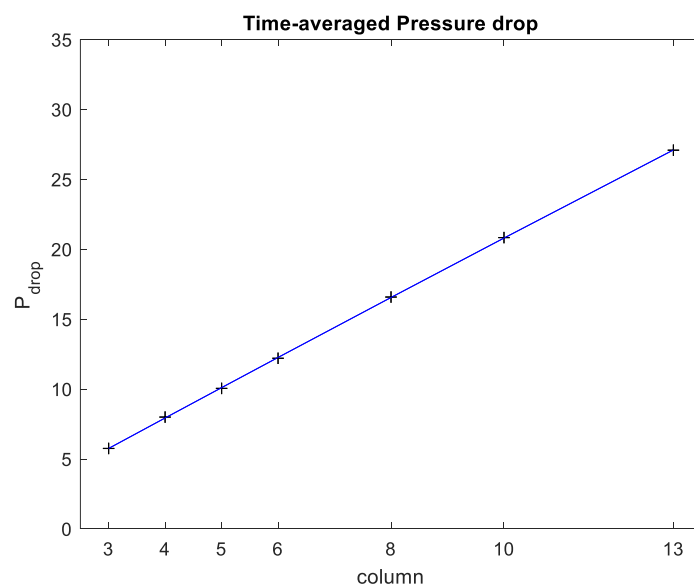


Figure 81 Time-averaged pressure drop up to 13 columns

## 5.4 Other types of arrangements

Breakwaters are often built to prevent or absorb energy from incoming flow of ocean to shorelines as a specific primary purpose, but they can cause many different and often unanticipated changes to the landscape such as environmental impact. So, they have been modified in various pattern for compatibility of character of the coastal landscape. In this section, we apply the same investigate method for a variety of breakwater designs, as we have done to our group of cylinders.

### 5.4.1 Zigzag arrangement

Walls or fences are employed not only for purpose of prevention of flows on shorelines but also for sand-trapping in the western world. They have been modified into several patterns and the one of form of pattern can be often seen is “zigzag arrangement” (also known as split-rail fence), the example is depicted in figure 82.

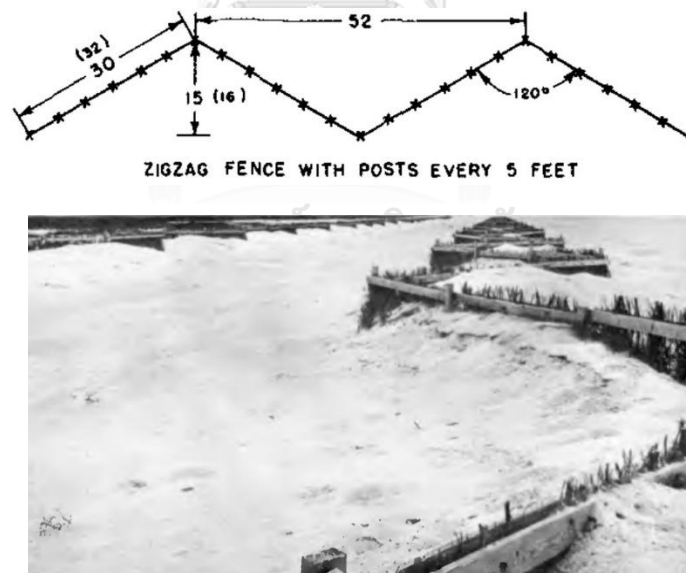


Figure 82 Zigzag arrangement of sand fence [31]

#### 5.4.1.1 Computational domain of zigzag arrangement and its position

combine the zigzag sand fencing with the 3 columns of array of cylinders in staggered arrangement. The domain of array of cylinders in zigzag arrangement are shown in figure 83 (a). Top and bottom boundary are set as periodic condition. The positions of cylinder are allocated as figure 83 (b). The result of this study will be demonstrated below.

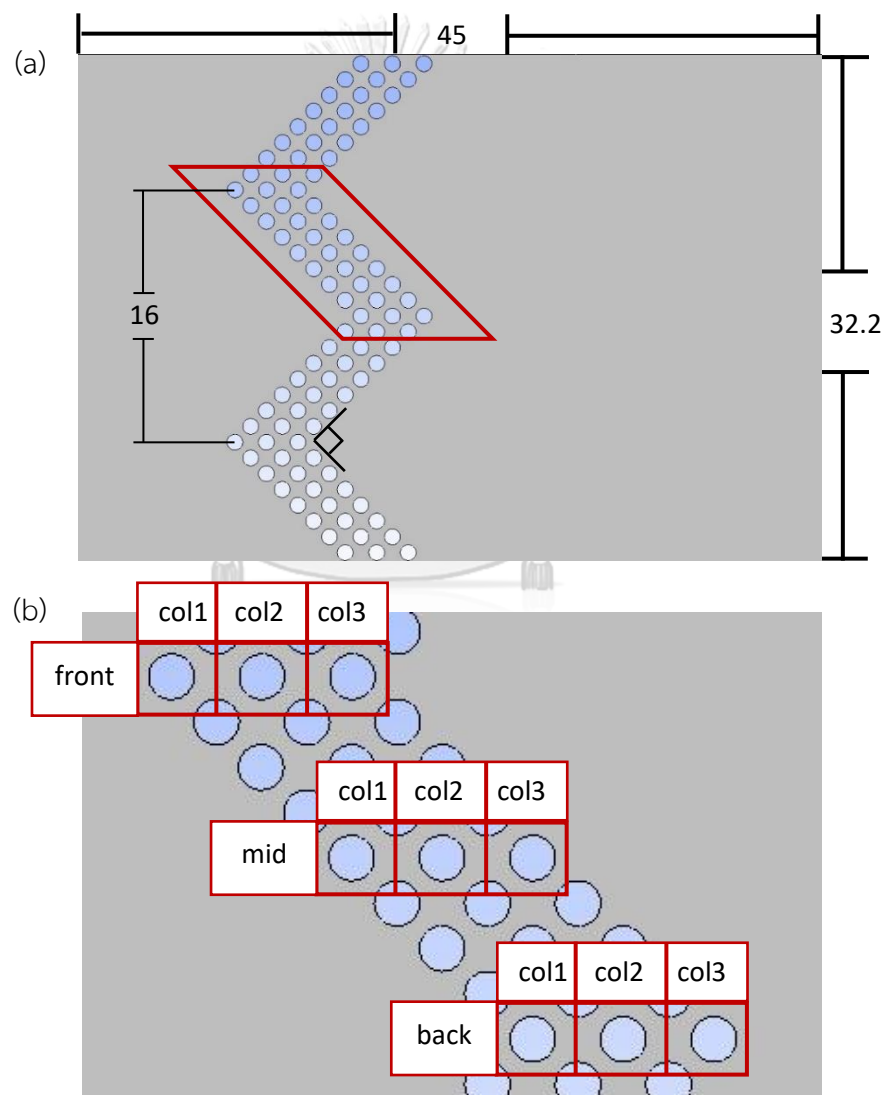


Figure 83 (a) Computational domain of zigzag arrangement, (b) its position

#### 5.4.1.2 Velocity vector

Figure 84 (a) velocity vector of flow past array of cylinders in zigzag arrangement at instantaneous non-dimensional time  $t=50.00$ . It is observed in figure 84 (b) that the flow regime behind cylinders at front position goes along as straight direction due to restricted and narrow area. In the other hand, the flow at back position has a swirling form.

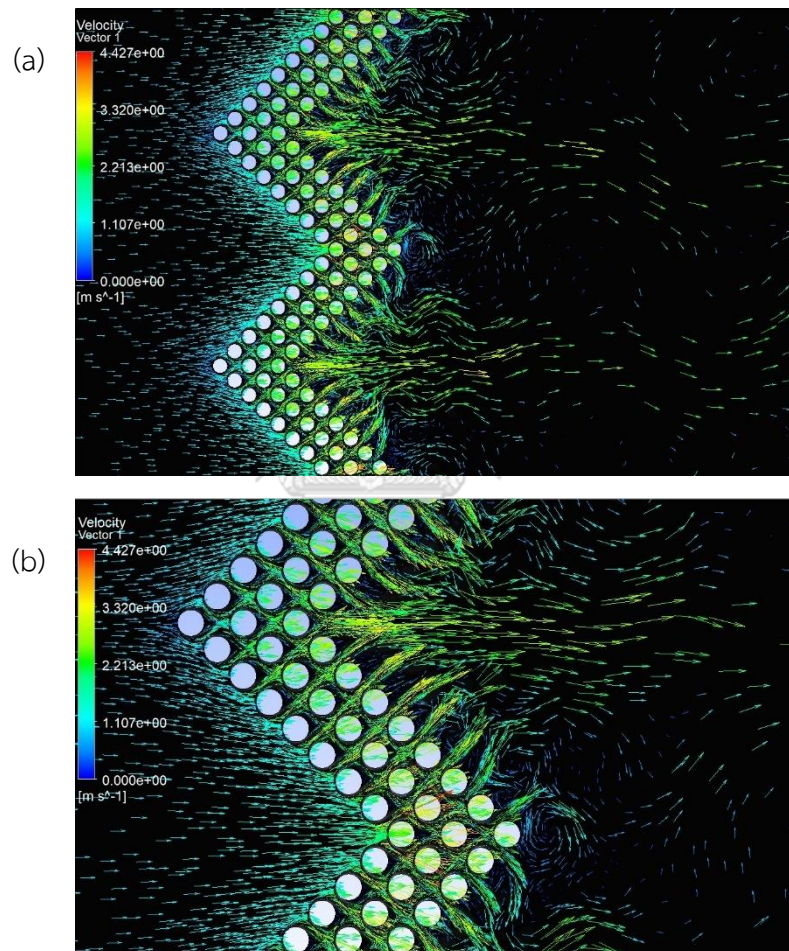


Figure 84 Velocity vector of zigzag arrangement: (a) the whole domain, (b) zoom-in

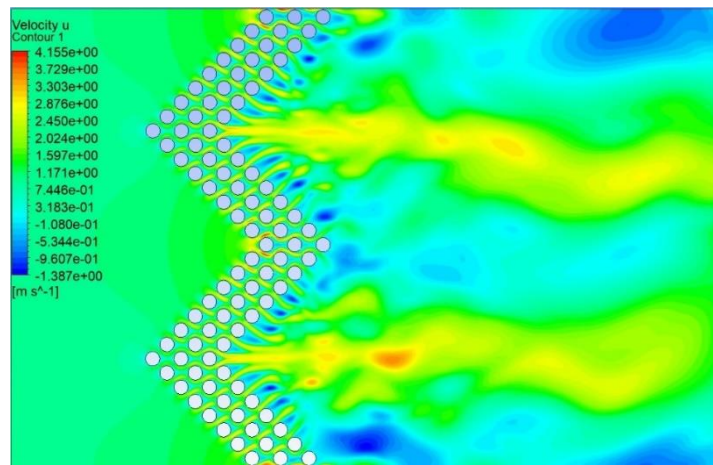
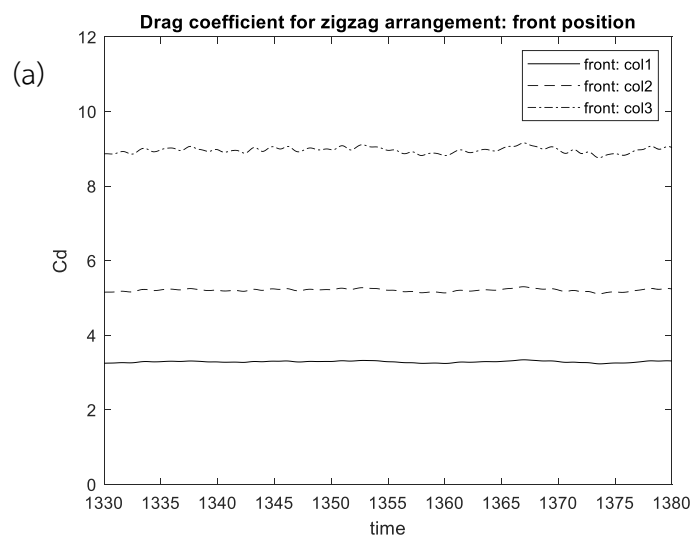


Figure 85 Streamwise velocity for zigzag arrangement

#### 5.4.1.3 Drag coefficient on a cylinder

Temporal histories of drag coefficient on a cylinder are shown as in figure 86 (cylinders' position as figure 83 (b)). The drag coefficient on the cylinder from 1<sup>st</sup> column in the front position is found to be the lowest value and the value on the cylinder from 3<sup>rd</sup> column is found to be highest as figure 86 (a). Whereas, in the back position, drag coefficient on the cylinder from 1<sup>st</sup> column is the highest and the value on the cylinder from the 3<sup>rd</sup> column is the lowest, shown in figure 86 (c). The drag coefficients in the mid position, shown as figure 86 (b) have similar value for all of columns.



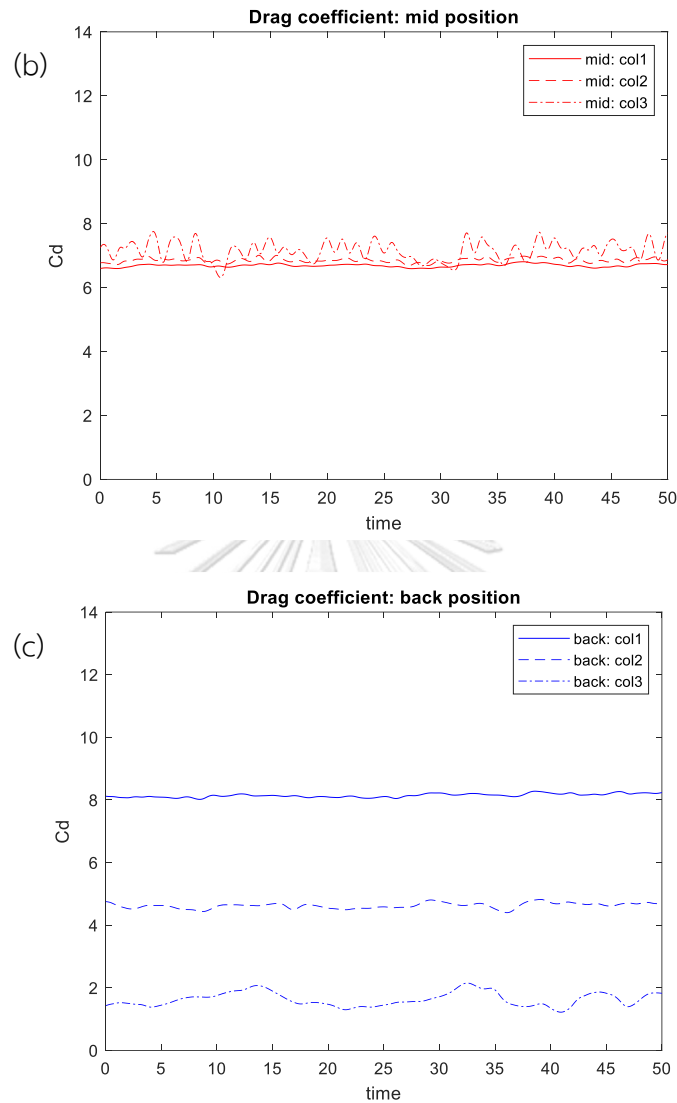


Figure 86 Drag coefficient for each cylinder from zigzag arrangement: (a) front position, (b) mid position, (c) back position

#### 5.4.1.4 Summation of drag force

The summation of drag force from flow past an array of cylinders in zigzag arrangement is compared with drag force from staggered arrangement. According to figure 87, the drag force from zigzag arrangement is close to that of the 5 columns of

staggered arrangement. However, the mean drag force from zigzag arrangement in our simulation is 317.5 with 96 cylinders, but the mean of drag force from staggered one is 295.7 with only 75 cylinders. So, drag force per one cylinder is approximately 3.94 for staggered type but only 3.31 for zigzag type.

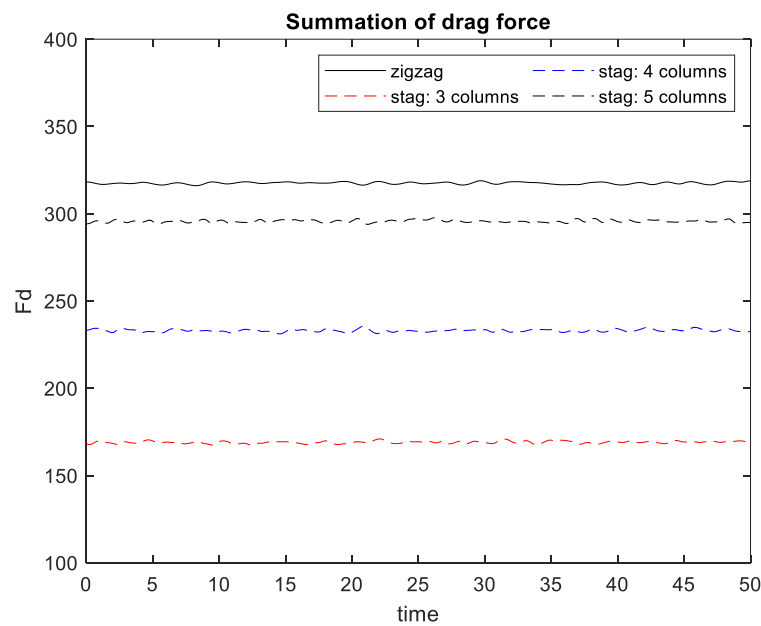


Figure 87 Comparison of summation of drag force

#### 5.4.1.5 Pressure contour and pressure drop

Pressure contour from zigzag arrangement is shown in figure 88. The pressure from inlet side is approximately 10 and it decreases to a value between -2.8 to 1.3 behinds cylinders depending on the location considered. The pressure gradient across the cylinder of 1<sup>st</sup> column in the front position is similar in value, but the color between back and front of the cylinder of 3<sup>rd</sup> column has the different value of pressure, shown in figure 88 (b). On the other hand, cylinder of 3<sup>rd</sup> column in the back position has the same shade all around it, shown in figure 88 (c).



The area-weighted average pressure across inlet and behind cylinders, shown in figure 89, refers to pressure drop approximately 10.2 and the value is also close to that of the 5 columns of staggered arrangement as well as summation of drag force.

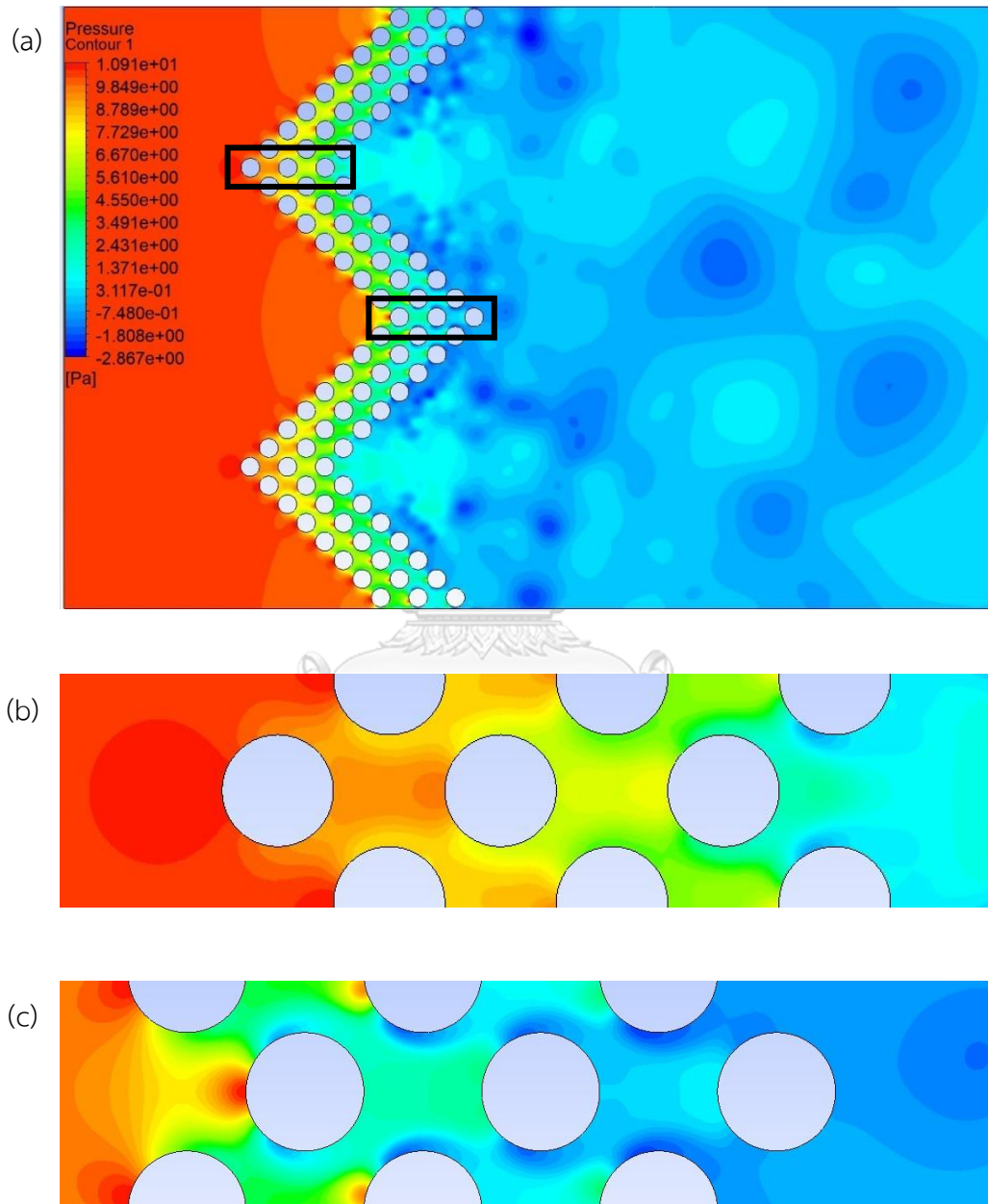


Figure 88 Pressure contour from zigzag arrangement: (a) the whole domain, (b) front position, (c) back position



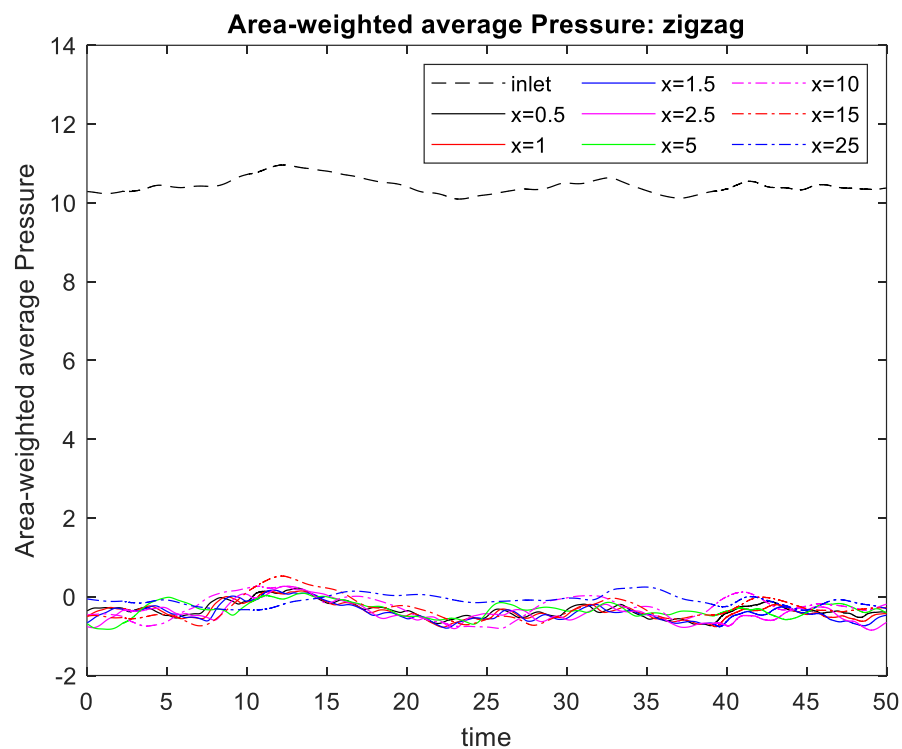


Figure 89 Area-weighted average pressure from zigzag arrangement

#### 5.4.2 Triangular and diamond modules

The triangular breakwater modules made of bamboo was experimentally studied [32]. This experiment was located 500 m far from inshore at area of Bang Khun Thian shoreline, upper Gulf of Thailand, southern Bangkok. The picture of bamboo breakwater in triangle module are shown in figure 90.

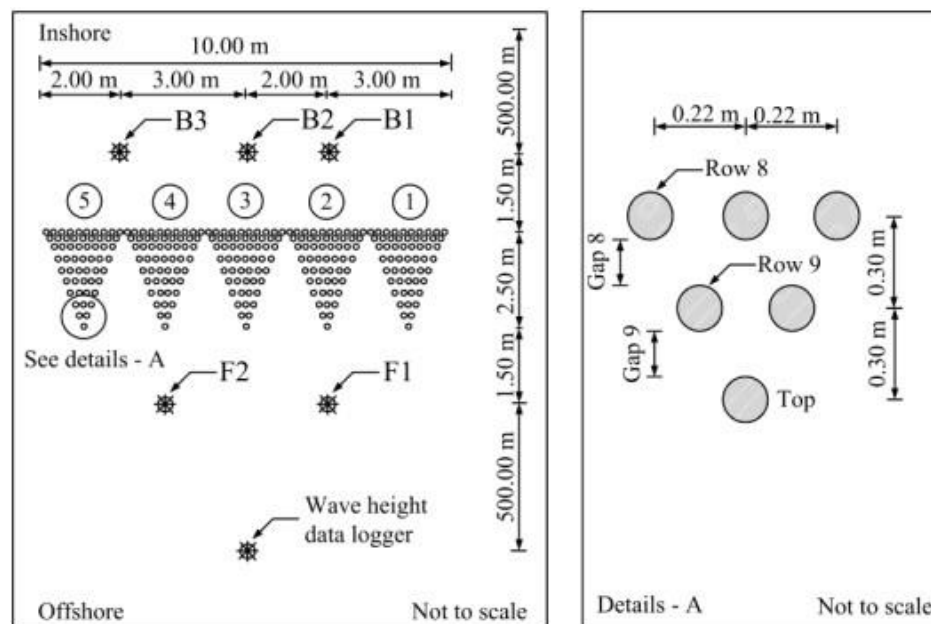


Figure 90 The set of triangular modules of the breakwater [32]

#### 5.4.2.1 Computational domains of triangular and diamond module and their position

The triangular module presented above are combined with the staggered arrangement that is shown in figure 91 (a). Another type of module supplemented by bundle of cylinders to the back parts of the triangular module and named as diamond module, shown in figure 91 (b). The positions of both modules are also shown in figure 91.

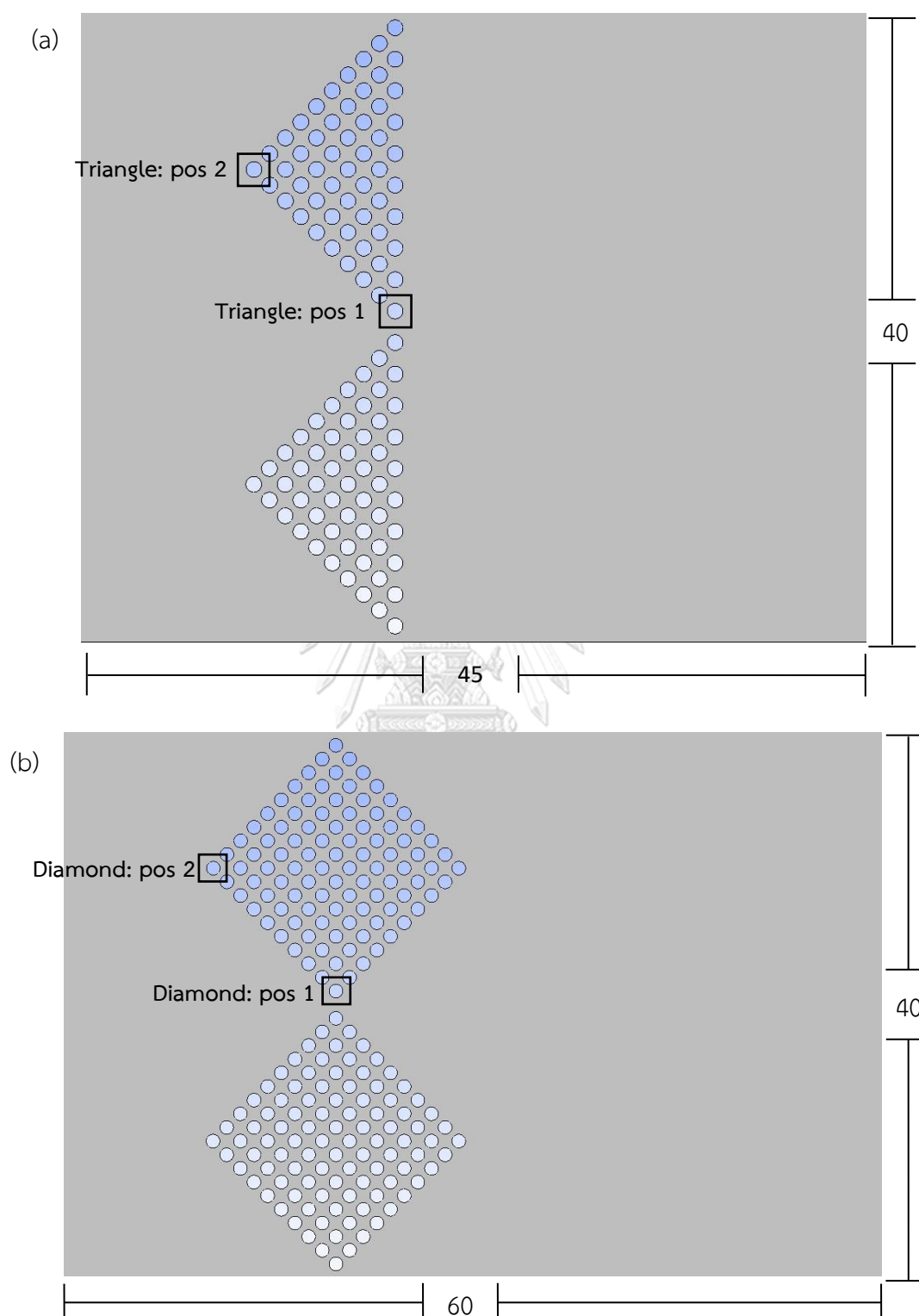


Figure 91 The computational domains: (a) Triangular module, (b) Diamond module

#### 5.4.2.2 Velocity vector

Figure 92 illustrates instantaneous velocity vector at non-dimensional time  $t=50.00$ . In the middle between module of diamond arrangement (figure 92 (a)), longer velocity vector in comparison with that of the triangular module (figure 92 (b)) is observed indicating larger streamwise transport taking place at the middle gap. Moreover, overall appearance of both types of arrangement seems not very much different.

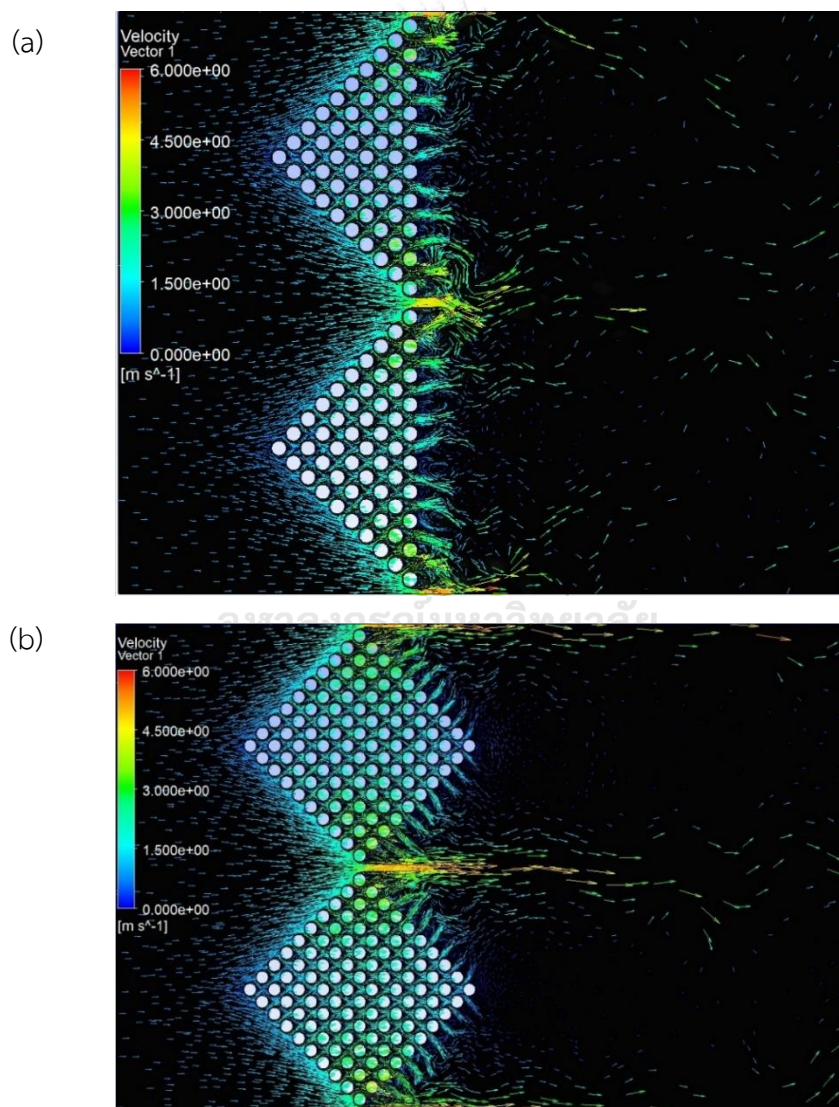


Figure 92 Vorticity and streamline: (a) Triangular module, (b) Diamond module

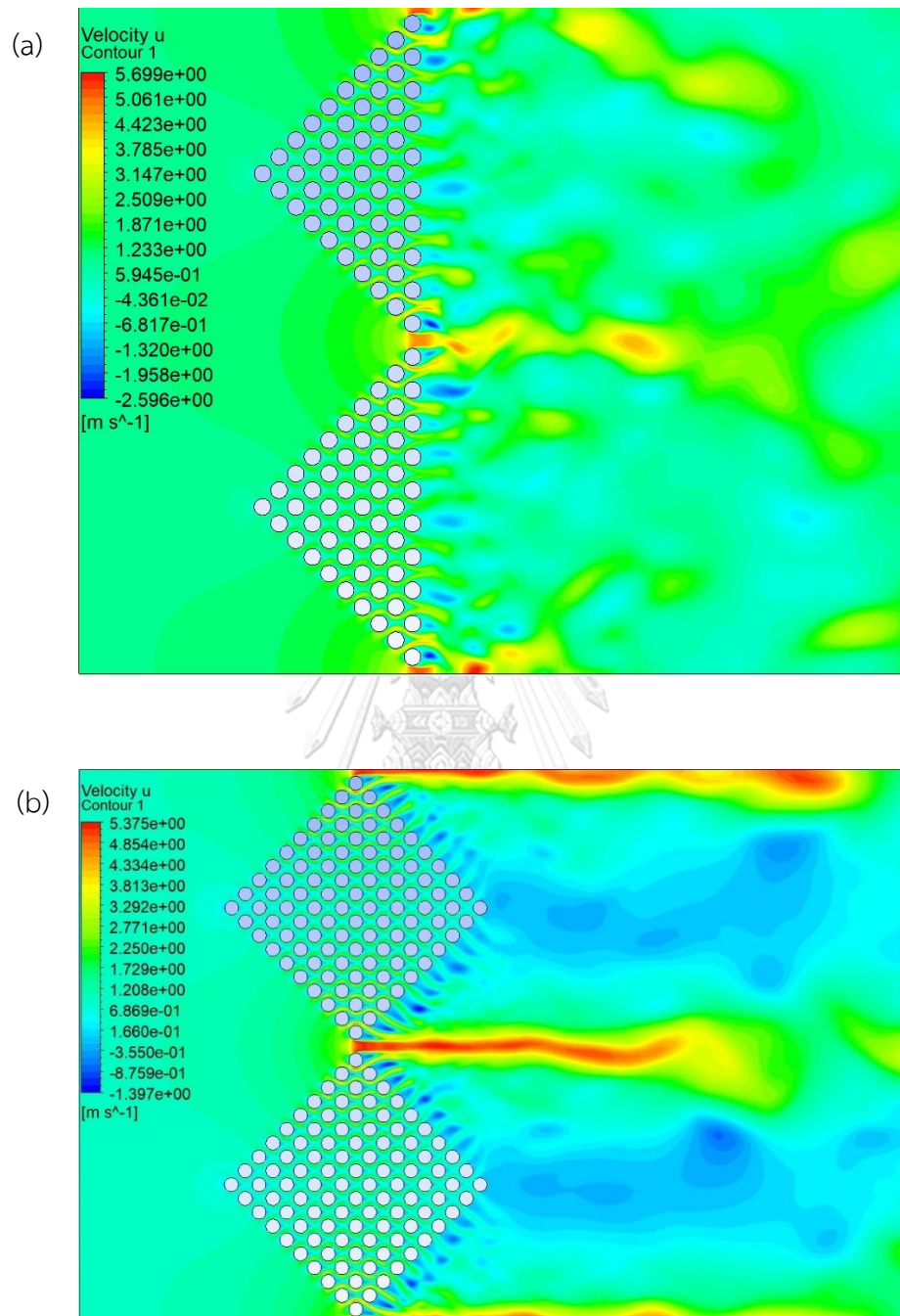


Figure 93 Horizontal velocity: (a) triangular, (b) diamond modules

### 5.4.2.3 Drag coefficient on a cylinder

The comparison of drag coefficient with respect of time on cylinders in position 1 and 2 for both modules are shown in figure 94. The drag coefficients on the cylinders of position 2, the tip of both modules in frontal side, are significantly less than the values from position 1 in both modules. The cylinders of position 1, the position of top and bottom of module, experience the highest  $C_d$  because they are solitary cylinders facing the incoming flow. The drag coefficient on cylinder of position 1 from diamond module are a bit higher than the value from the triangular module in the same position.

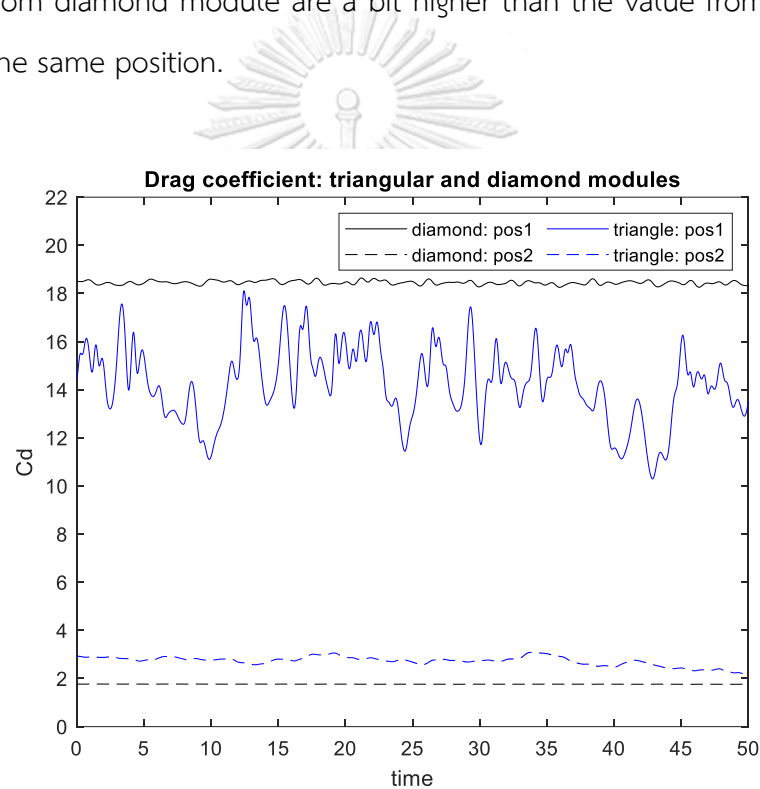


Figure 94 Drag coefficients on cylinders from triangular and diamond modules

### 5.4.2.4 Summation of drag force

From figure 95, it is obvious that the diamond module obtains the summation of drag force higher than the triangular configuration. Although, the time average of drag force from the diamond module values approximately 501.6 but only 293.0

from triangular module, with the percentage of difference is 41.6%. The diamond configuration contains 200 cylinders but the other contains 110 cylinders. The drag force is 2.51 per a cylinder for diamond module yet 2.66 per one for triangular module.

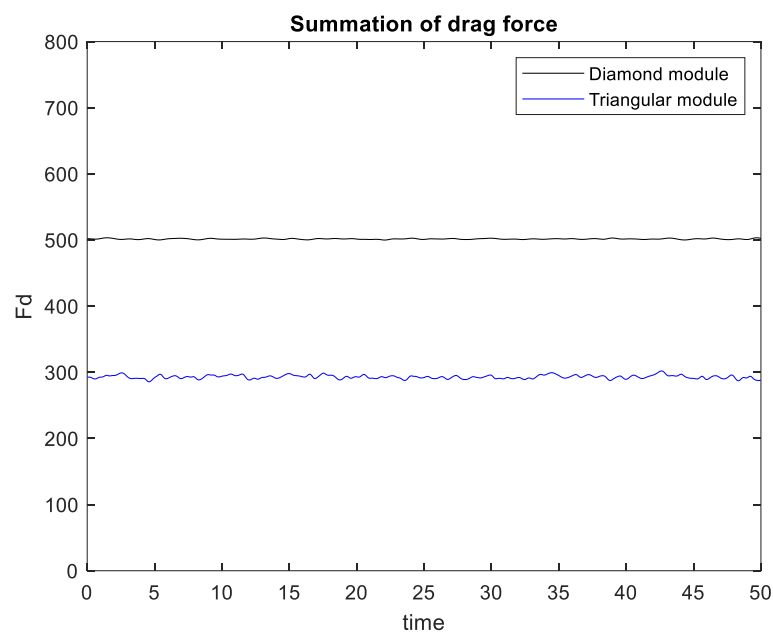


Figure 95 Summation of drag force from triangular and diamond modules

#### 5.4.2.5 Pressure contour and pressure drop

Figure 96 (a) and figure 96 (b) illustrate pressure contour of flow past triangular and diamond modules respectively. The pressure of inlet for triangular and diamond modules is approximately 8.1 and 13.7 respectively. The cylinders on position 2, tip position, on both modules have similar pressure distribution around them Figure 97 (a) and figure 97 (b) show area-weighted average pressure of both modules. The pressure drop from the diamond module are about 14 on average, almost 2 times larger than the triangular one as well as summation of drag force.



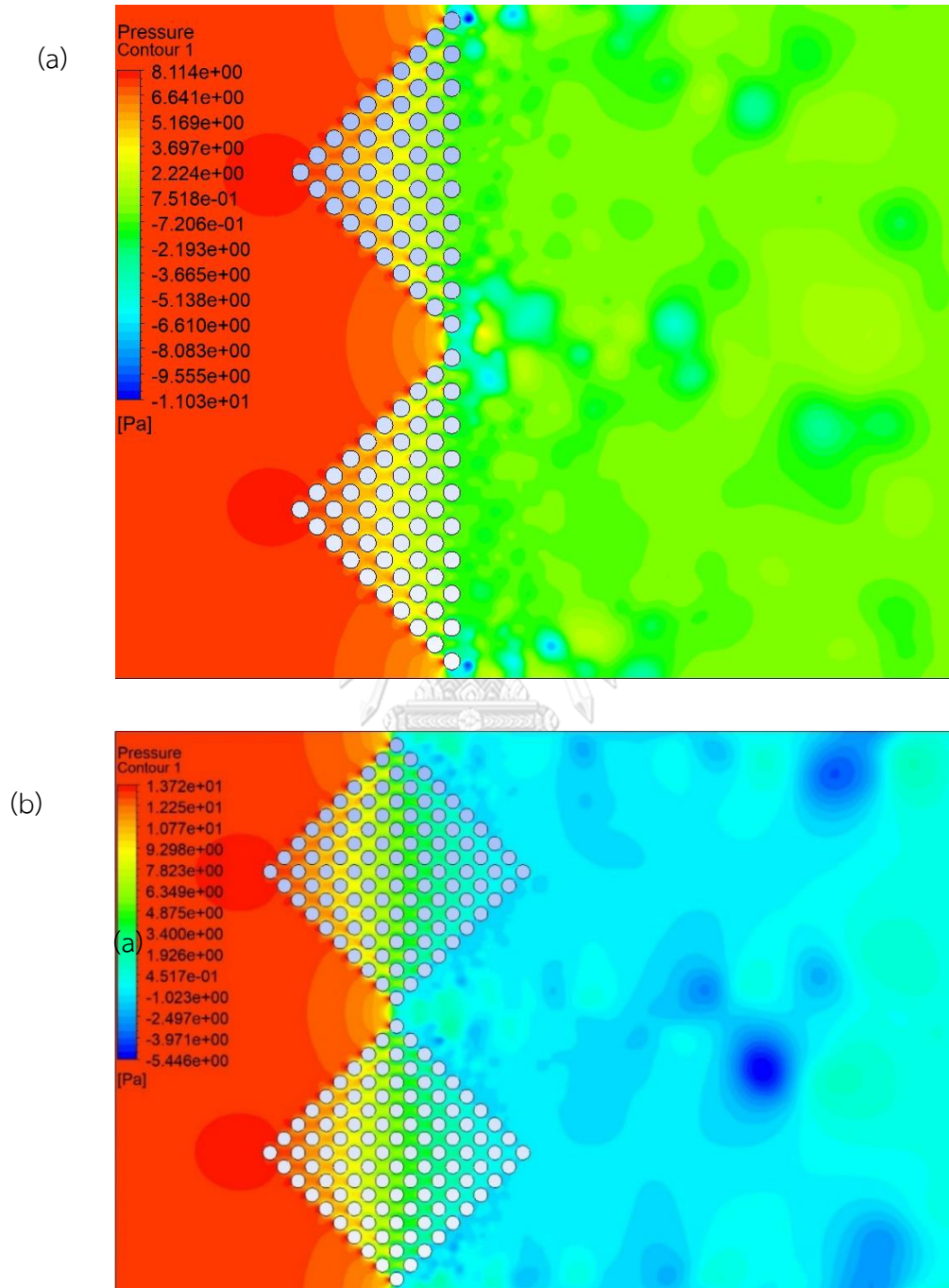


Figure 96 Pressure contour at time = 50.00: (a) the triangular module, (b) the diamond module



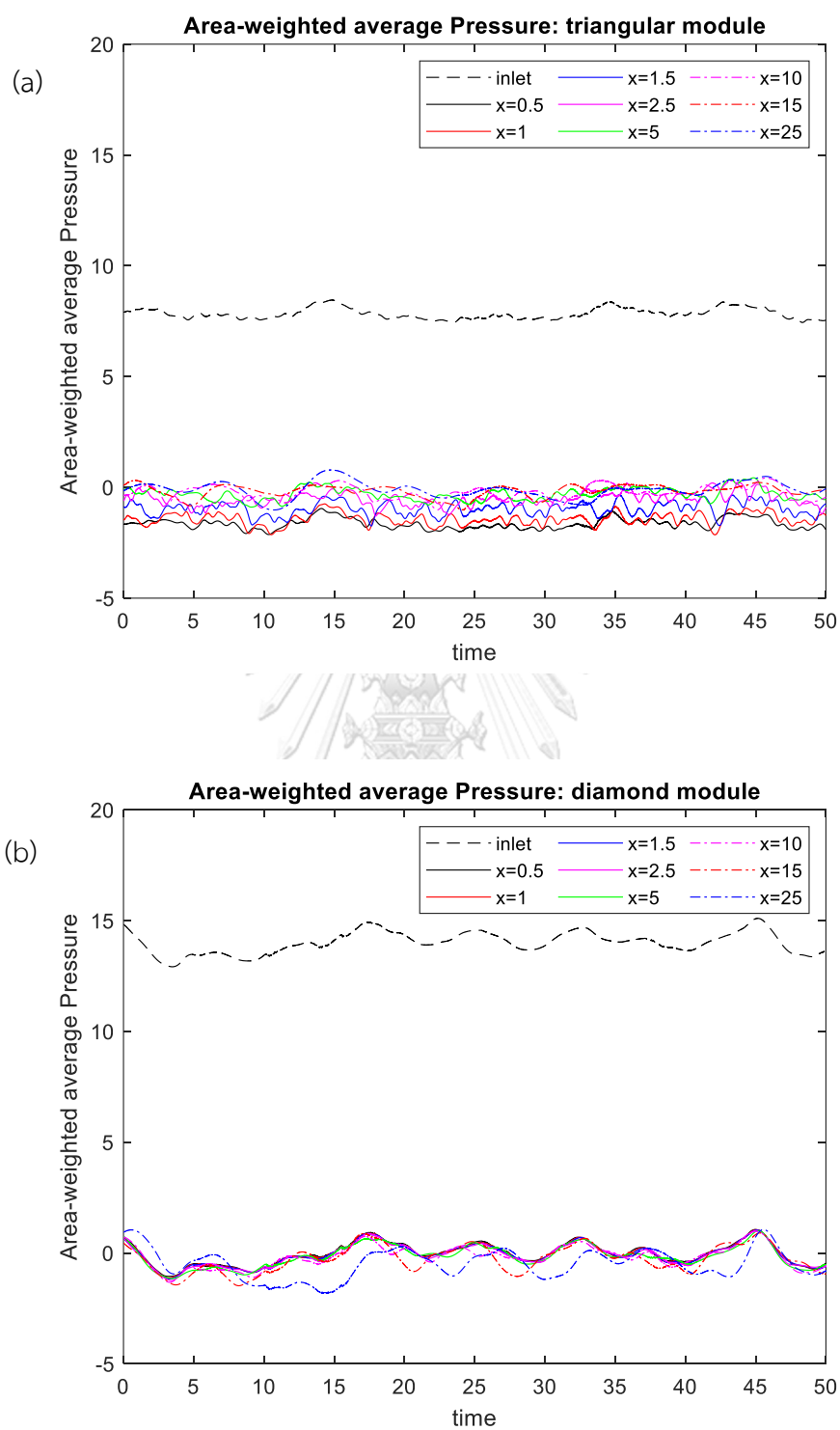


Figure 97 Area-weighted average pressure: (a) the triangular module, (b) the diamond module

### 5.4.3 T-shape and line-shape models

Line-shape breakwaters, shown in figure 98, can be often seen even around shoreline of Thailand that most of them are made of stacks of rocks which are located on offshore so we will apply this kind of breakwater to the staggered arrangement with 4 columns.

Another type of breakwater model is similar to the line-shape breakwater with tail, called T-shaped module. Dr. Thorsten Albers [33] built the T-shaped module with bamboo as bamboo-fencing and located them in the muddy coastal zone of the lower Mekong Delta in Vietnam. The pictures of bamboo-fencing in T-shaped arrangement are shown in figure 99.



*Figure 98 Line-shape breakwater*

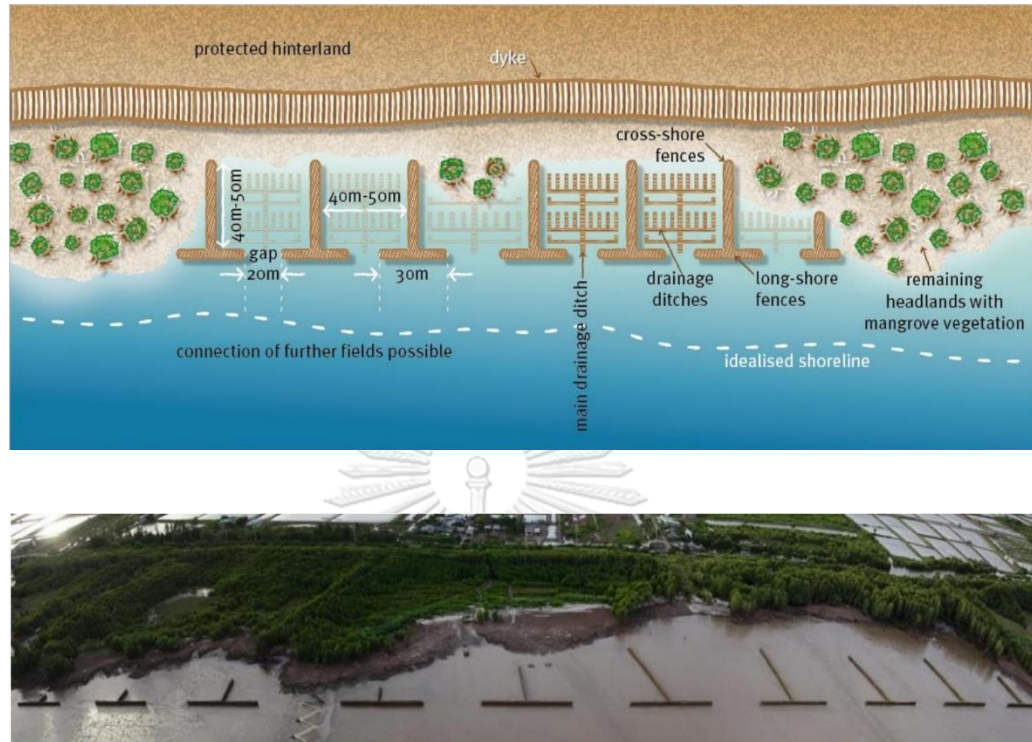


Figure 99 The model of T-shaped bamboo-fencing and its actual placement in the coastal zone of the lower Mekong Delta in Vietnam [33]

#### 5.4.3.1 Computational domains of T-shape and line-shape and their positions

Figure 100 presents computational domains of T-shape and staggered arrangement with 2 sides of space which is applied from 4 columns of staggered arrangement we studied before. The prescribed positions of these computational domains consist with top position, mid position and tail position for only T-shape model. Top and bottom of domains are set as periodic condition for both models.

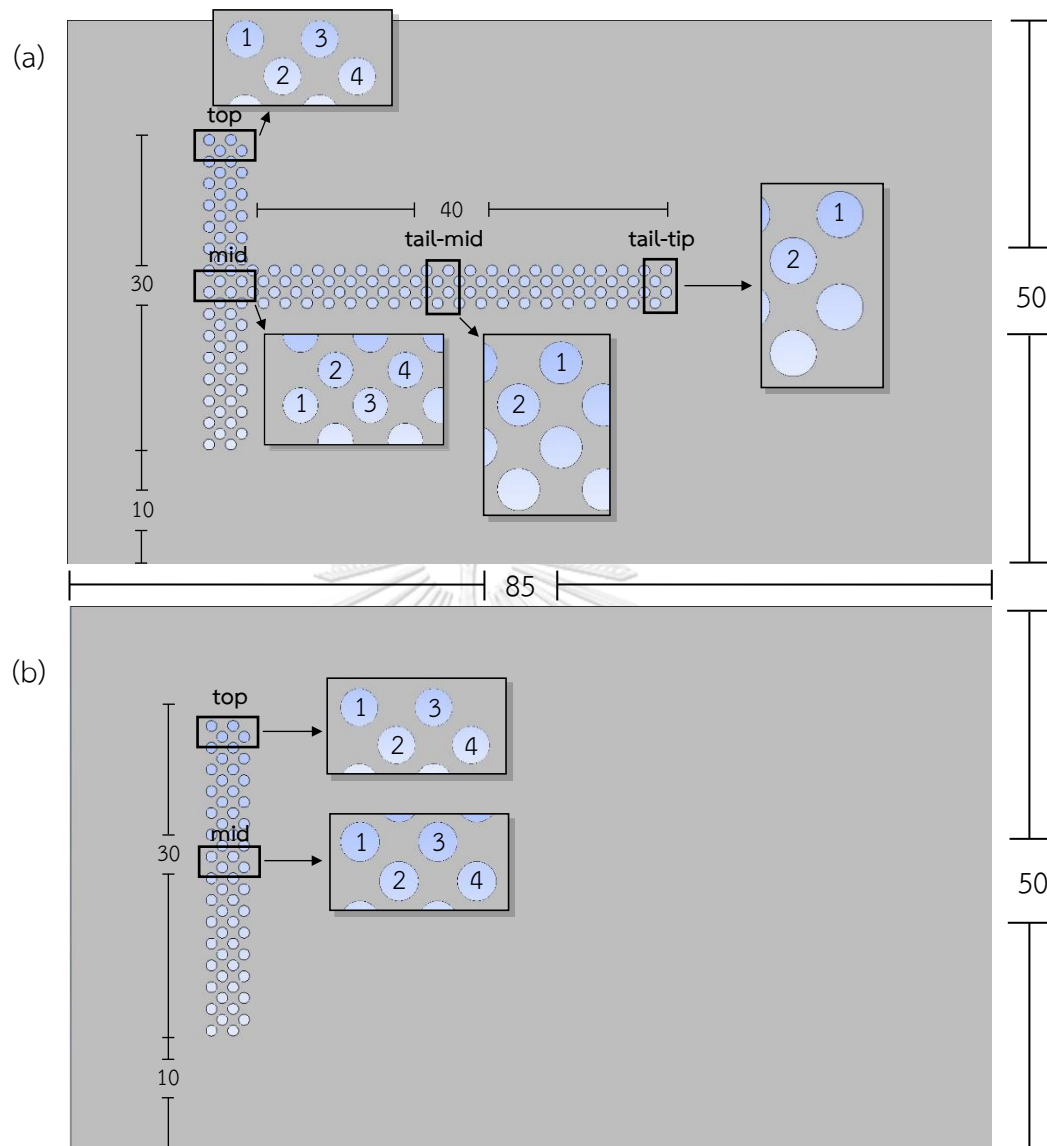


Figure 100 The computational domains: (a) T-shape, (b) line-shape

#### 5.4.3.2 Velocity vector

Velocity vector of T-shape and line-shape are shown in figure 101 in color-legend scale of 0-3. The velocity vector in free space area at the top and bottom is longer than that accumulated in the area behind the breakwater. However, the velocity vector in space of T-shape is lower than line-shape due to the tail of T-shape. The velocity vector around the tail slightly curls especially its tip.

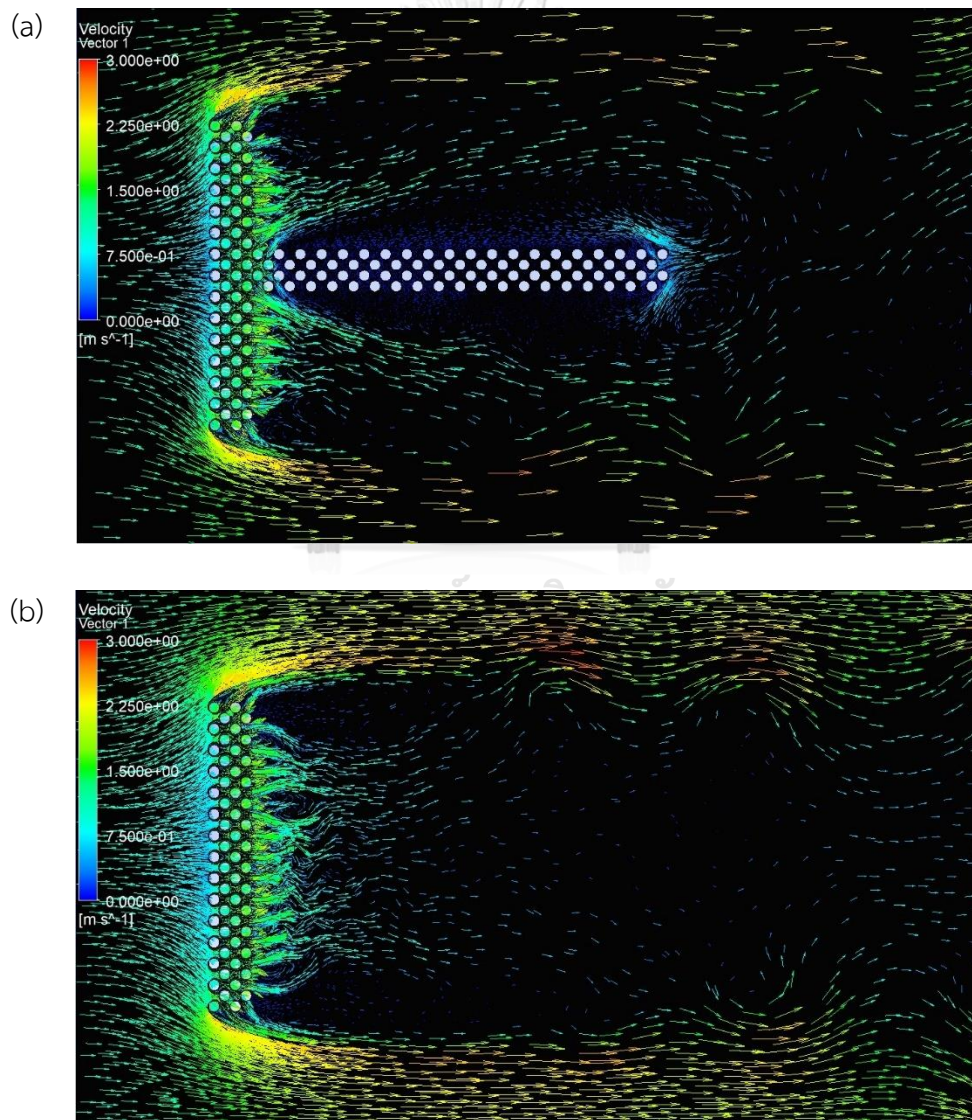


Figure 101 Velocity vector: (a) T-shape, (b) line-shape



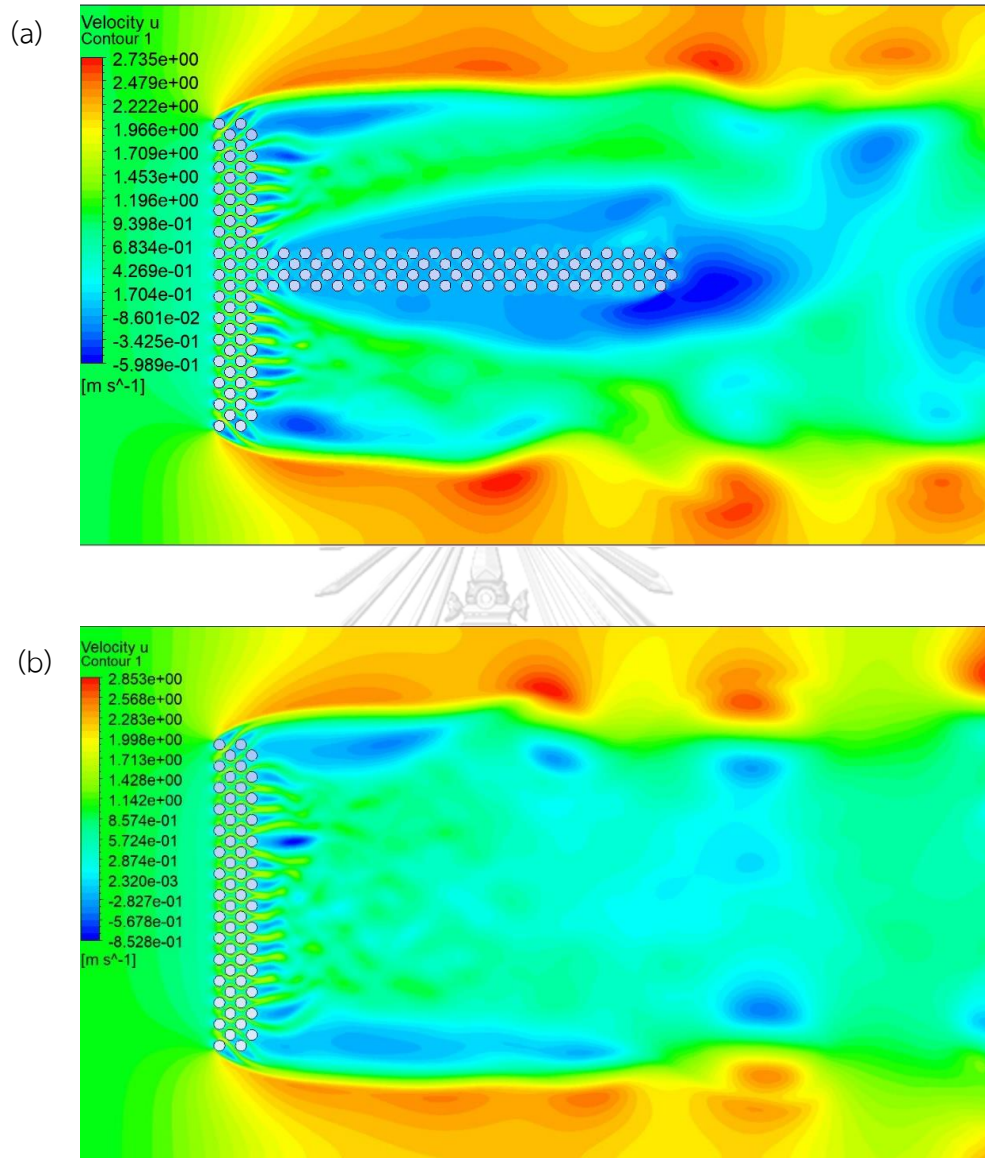


Figure 102 Horizontal velocity: (a) T-shape, (b) line-shape

### 5.4.2.3 Drag coefficient on a cylinder

According to figure 103, drag coefficients from all 4 cylinders of top position for both models are almost equal, approximately 3.3 to 3.5. Nevertheless, the drag coefficient from cylinders of mid position from T-shape decrease to 2 – 2.5, However, the results of mid position from line-shape are the same range of cylinders on top position.

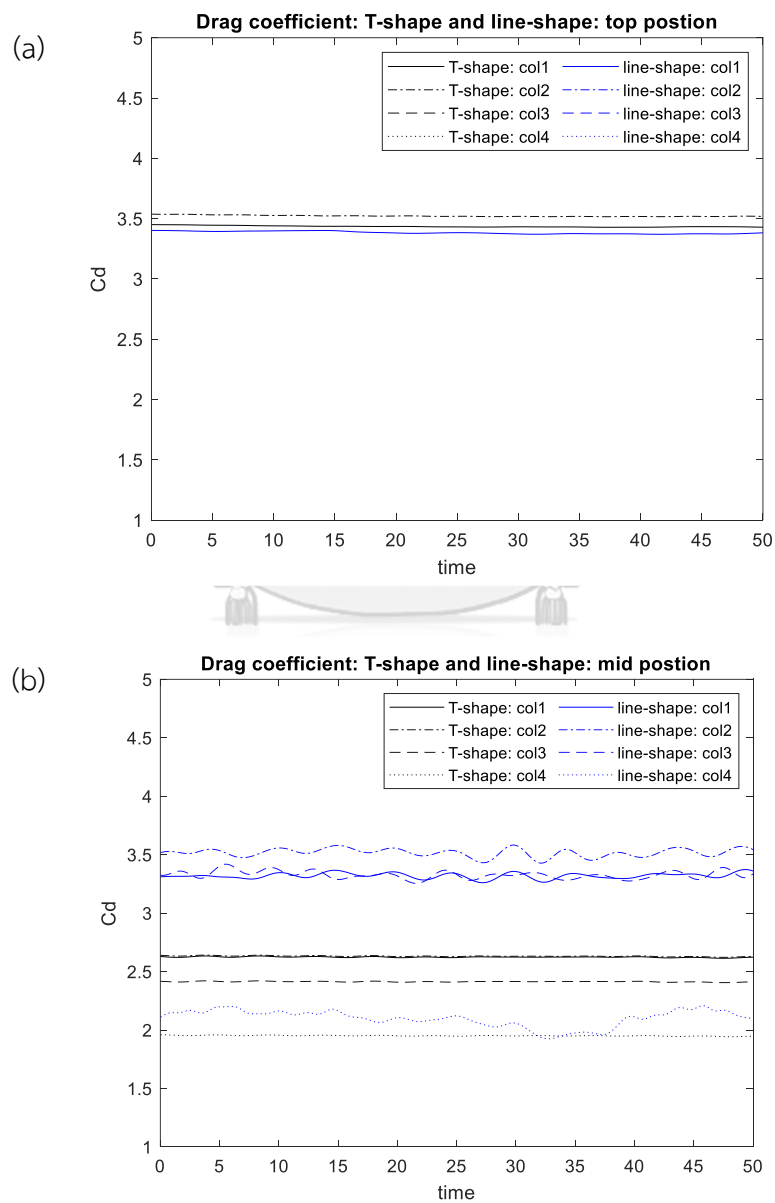


Figure 103 Drag coefficients from both models: (a) top position, (b) mid position

Drag coefficients from tail position on T-shape model, shown in figure 104, are very small not only the mid of tail but also at the tip.

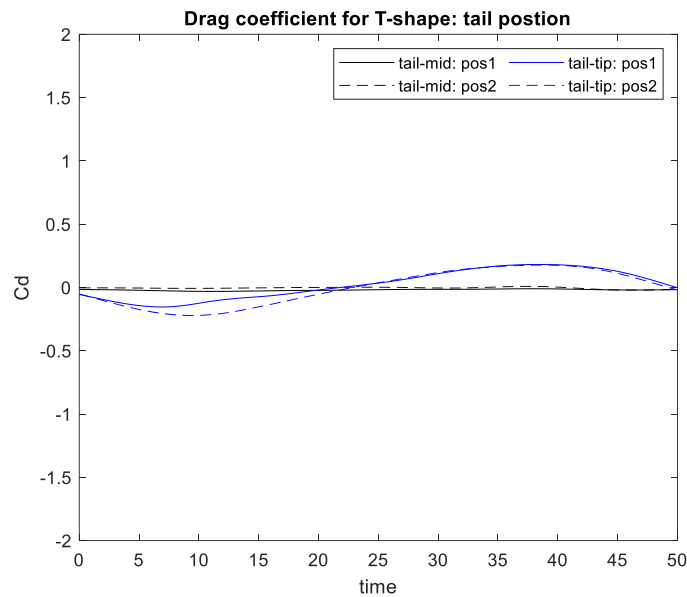


Figure 104 Drag coefficients from tail position

#### 5.4.3.4 Summation of drag force

Summations of drag force from both T-shape and Line-shape, shown in figure 105, are in the equal value range, around 78 to 80. The tail of T-shape does not significantly affect the summation of drag force. As seen in the figure 104, the tail of the T-shape configuration does not play a big part in contributing to the summation of the module's drag.



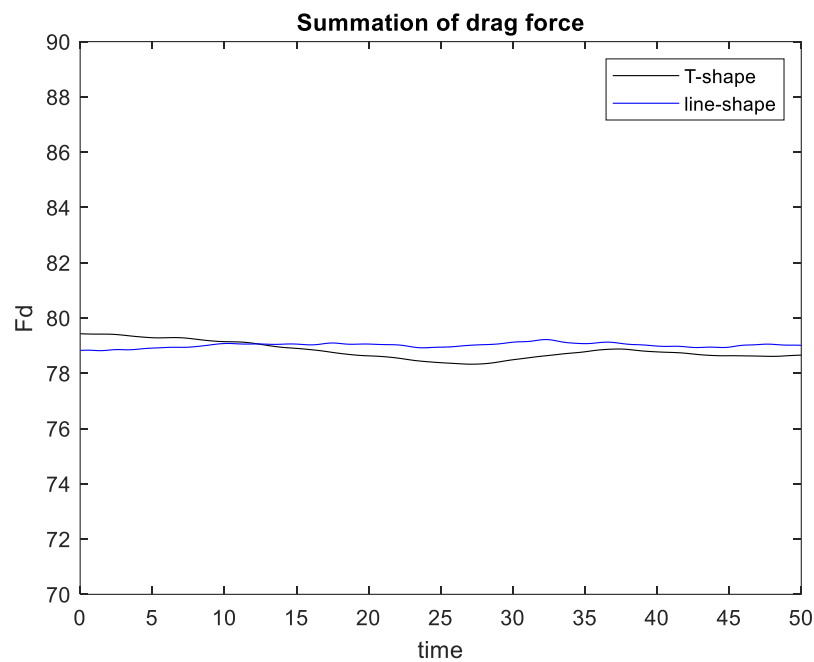


Figure 105 Summation of drag force from T-shape and line-shape

#### 5.4.3.5 Pressure contour and pressure drop

Figures 106 shows the instantaneous pressure contour at time = 50.00 and for T-shape and line-shape models. As shown in both figures, the pressure gradients from inlet side for both models are almost the same. The pressure decreases to approximately 1.2 nearby the models. The pressure from T-shape and line-shape models behind cylinders in time average are around 0 to -1 and 0 to -0.7 respectively. Figure 107 shows area-weighted average pressure with time for both models and the results of pressure drop are around 2 to 2.7.

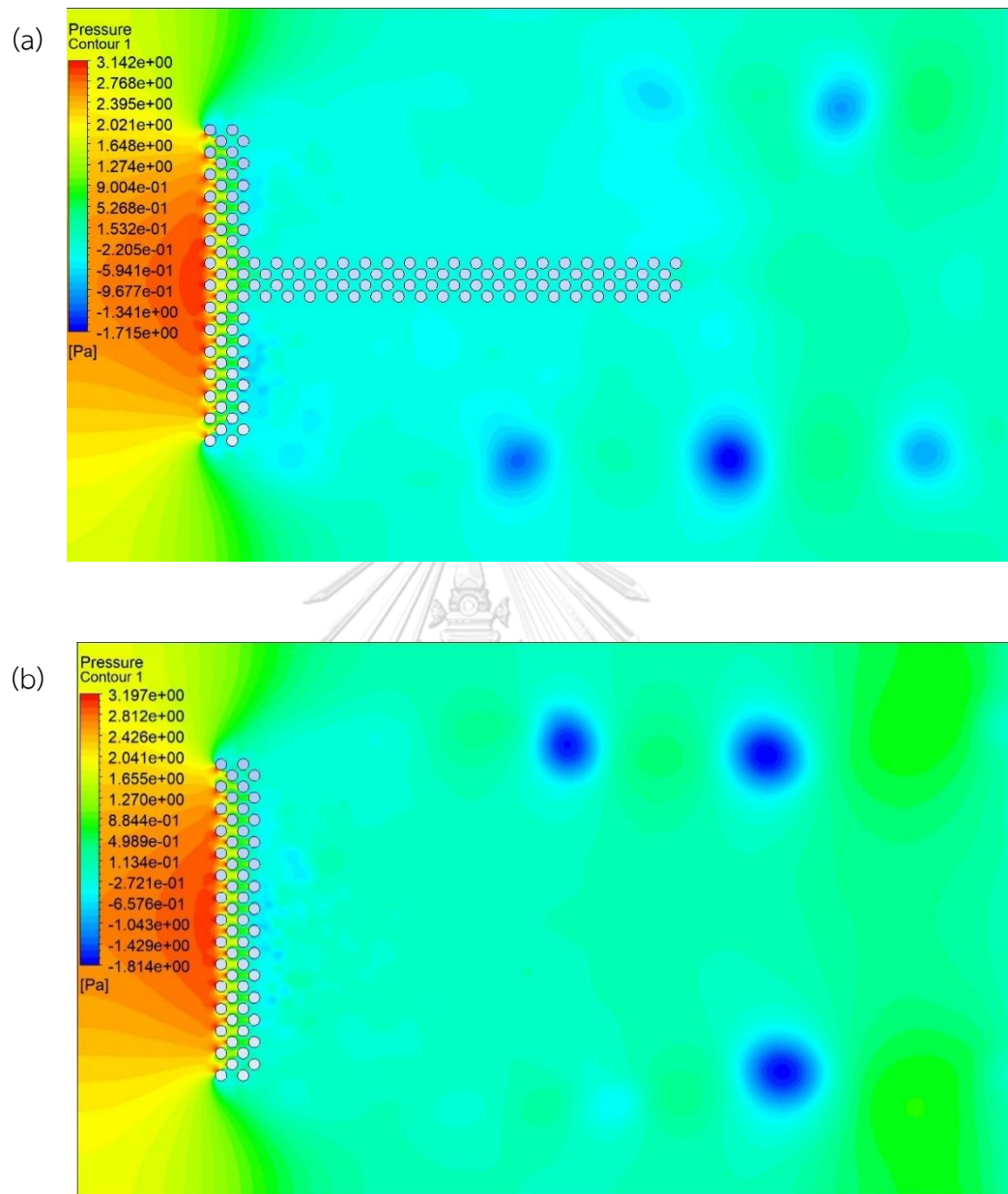


Figure 106 Pressure contour at time = 50.00: (a) T-shape, (b) line-shape

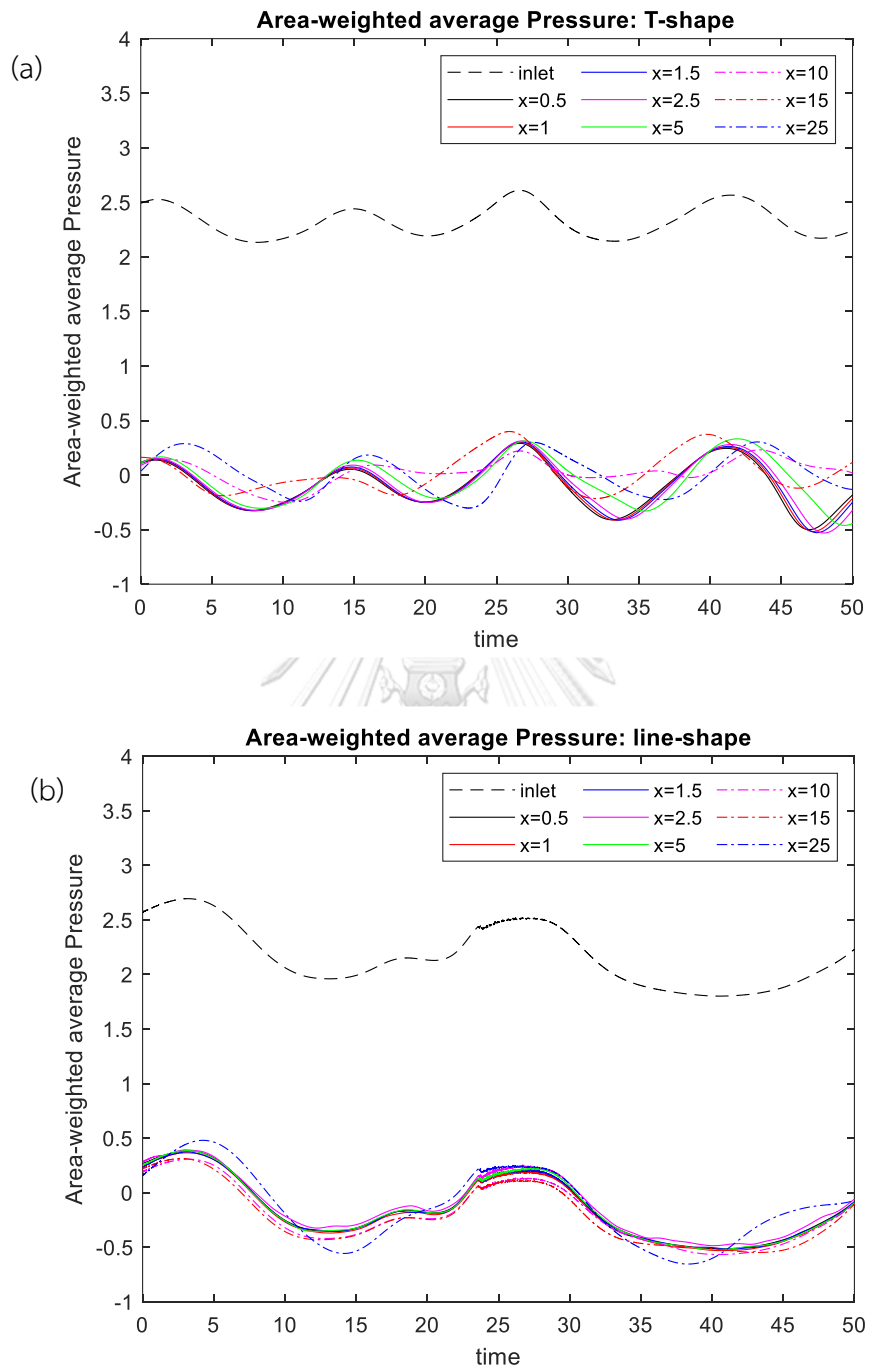


Figure 107 Area-weighted average pressure: (a) T-shape, (b) line-shape

### 5.4 Summary result

Table 9 shows the summary from the results of flow past array of cylinders in various arrangements. The diamond model unites with 200 cylinders but the summation of drag force and drag coefficient of model are 501.60 and 25.08, not the highest values. The 13 columns staggered arrangement have 195 cylinder that experiences the top rank of summation of drag force, drag coefficient of model and it reduces the most pressure across the cylinders. The aligned arrangement with 3 columns has the smallest results and the values from T-shape and line-shape are very small as well because of the space nearby the model.

*Table 9 Summary result of arrays of cylinders*

Type of arrangement	No. of cylinders	spanwise width, l	$P_{drop}$	$F_d$	$F_d$ per a cylinder	$C_{d(model)}$
Staggered: 3 columns	45	30.4	5.76	169.04	3.76	11.12
Staggered: 4 columns	60	30.4	8.00	233.46	3.89	15.36
Staggered: 5 columns	75	30.4	10.05	296.86	3.96	19.53
Staggered: 6 columns	90	30.4	12.21	364.13	4.05	23.96
Staggered: 8 columns	120	30.4	16.59	494.91	4.12	32.56
Staggered: 10 columns	150	30.4	20.85	632.35	4.22	41.60
Staggered: 13 columns	195	30.4	27.09	819.21	4.20	53.90
Aligned: 3 columns	45	30	1.84	52.98	1.18	3.53
Aligned: 4 columns	60	30	2.15	61.85	1.03	4.12
Aligned: 5 columns	75	30	2.43	70.58	0.94	4.71
Zigzag	96	32.2	10.44	317.33	3.31	19.71
Triangular module	110	40	7.84	292.48	2.66	14.62
Diamond module	200	40	14.00	501.60	2.51	25.08
T-shape	136	50	2.33	78.97	0.58	3.156
Line-shape	58	50	2.16	79.02	1.36	3.16

Figure 108 shows the summation of drag force vs number of columns. the 13 columns in staggered arrangement have the highest drag force and the aligned arrangement with 3 columns has the lowest one. This figure demonstrates that summation of drag force does not depend on only number of columns, but geometrical configurations of arrangements are also important.

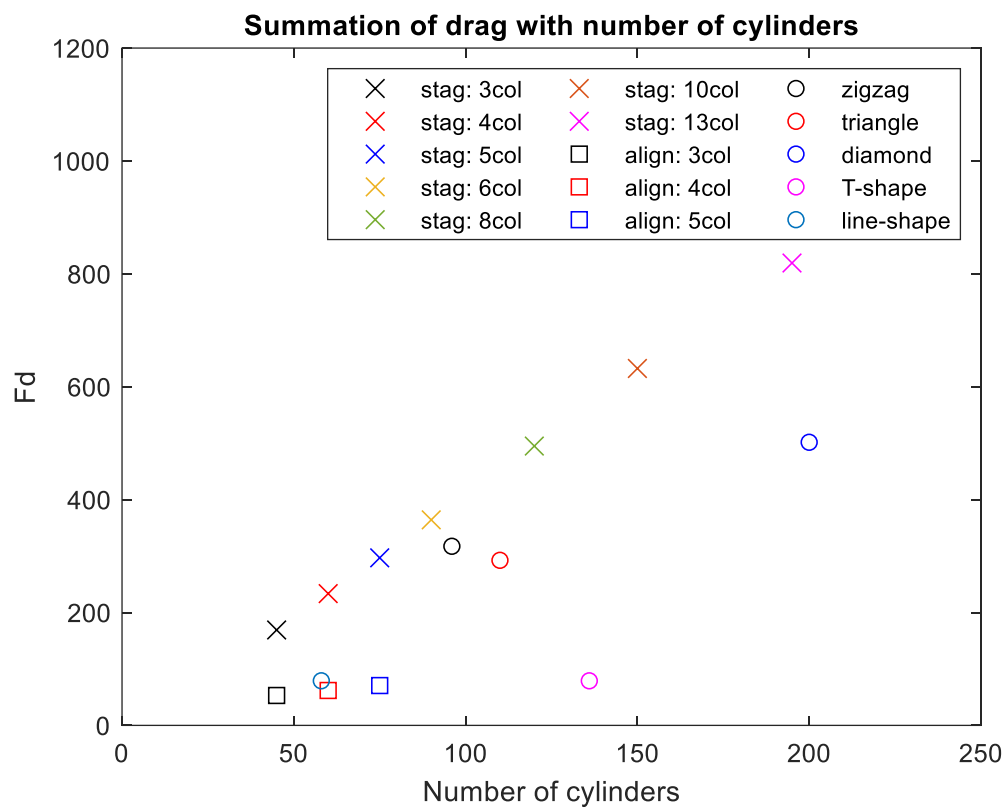


Figure 108 Summation of drag force vs number of cylinders

## CHAPTER 6

### CONCLUSION

Solid object immersed in fluid flow are prevalent in nature. The phenomenon of flow past a body or a group of obstacles has both benefits and has caused damages for human. Either which human has studied and taken benefits for centuries. Understanding the phenomenon allows us to prevent problems such as flood and drought, as well as creating innovations such as sailing and aviation. In Thailand, the coastal erosion along shorelines of lower central to southern region has increasingly been prevalent for decades. A popular method for preventing this problem is using breakwaters, typically in Thailand are made of bamboo, known as “bamboo fencing”.

Realizing the important of such problem, the thesis presents an investigation of flow past several geometrical configurations of bamboo fencings. Array of cylinders is used in place of bamboo sticks in the study as a convenient model. Simplification is also done for the near-shore flow where an incoming flow, toward shoreline, is taken to be steady and of low velocity. While the model represents, to some degree, the real event of flow past bamboo fencing, we realize several features that are not taken into account, such as larger velocity and the presence of underwater wave. The investigation is conducted via a set of numerical simulations, using ANSYS®-Fluent, a commercial software capable of setting up and solving general fluid flow problems.

The investigation consists of 4 parts whose fencing configuration differ. For the first geometrical configuration (part 1), two cylinders are placed side-by-side and the effect of gap size upon drag force, lift force, and wake frequency is studied. The rest of the configurations (part 2-4) consider realistic fencing arrangements. For all

configurations, the Reynolds number based on incoming flow velocity ( $U_\infty$ ), cylinder diameter ( $D$ ), and fluid kinematic viscosity is set at  $Re = 100$ . The mesh density (near cylinder's surface and in the wake region) is kept as similar as possible for all of the configurations. To determine an optimal mesh density and time-step size, as they are designed/chosen similarly for all of the cylinder arrangements, validation is done for mesh convergence and also of time-step size for the two-dimensional flow past a circular cylinder. The results of drag coefficient, lift coefficient and Strouhal number are in very good agreement with previous literatures. The results for all of the geometrical configuration are listed in Table 9.

For part 1 (chapter 4), a pair of cylinders in side-by-side arrangement with transverse gap width between cylinders,  $T/D = 1.5$  to 20 are considered. With respect to a single cylinder, placing cylinders side-by-side increases drag on both objects; enhances lateral outward (away from the other cylinder) force; as well as triggers a higher wake dominant frequency. The effects slowly diminish as the gap widens and becomes negligible for  $T/D$  about 15. It is found that as the gap width decreases, the characteristic wake frequency; denoted by Strouhal number, increases with the rate close to being linear, the drag coefficient increases quite quadratically, and the magnitude of lift coefficient increases exponentially, especially during which  $T/D$  is < 7.

For part 2 (chapter 5.2), staggered and aligned cylinder arrangements with 3 to 5 columns are studied. For the staggered configuration, cylinders located at any position experience similar value of drag coefficient except for those located at the rear of the pack (last column) whose drag coefficient is relatively much smaller. For the aligned configuration, the result is interestingly in reverse, cylinders at the first column experience largest drag while the drag forces for rest are of similar, lower value. The combined drag force from all cylinders of the staggered arrangement is larger than that from the aligned arrangement, for the same number of columns. The pressure drop across the fence is found to be of the similar trend as it is directly

proportional to the combined force. Lastly, an additional cylinder column that is added to the staggered arrangement has a large effect on the summation of drag.

For part 3 (chapter 5.3), staggered arrangements with up to 13 columns are considered. Drag coefficients are found to be of the same pattern, the values are in the same range except only those of the cylinders in last column that decrease significantly. The summation of drag force, and consequently pressure drop, increases linearly as more column is added.

For part 4 (chapter 5.4), additional five configurations derived from what are found in real-world fencing are considered: zigzag, triangular, diamond, T-shape, and line-shape. The zigzag type is taken from the straight 5-column staggered configuration, done previously, but with 90 degrees zigzag pattern. The zigzag arrangement has drag summation and pressure reduction that are only slightly larger than the 5-column staggered arrangement, while consists of a larger number of cylinders. For the triangular and diamond modules, cylinders at the far left and far right of both arrangements experience largest drag. The summation of drag force and pressure drop of the diamond module are almost twice as much as those of the triangle. For the T-shape and line shape, the drag summation and pressure drop are significantly smaller than the other 3 modules. This is due to the free space in the lateral direction outside of the module; that allows fluid to pass through the least resistance path. It is also found that the tail of the T-shape module does not significantly have an effect upon the summation of drag force and pressure drop.



## APPENDIX

### CONFERENCE PROCEEDING

This chapter shows part of the work which has been submitted for the upcoming conference of the mechanical engineering network of Thailand at Mida Grande Hotel Dhavaravati Nakhon Pathom between 20 - 23 July 2021.

#### Numerical study of flow past a pair of cylinders at a low Reynolds number

Woraphon Wannaviroj<sup>1</sup> and Karu Chongsiripinyo<sup>1\*</sup>

<sup>1</sup>Department of Mechanical Engineering, Faculty of Engineering, Chulalongkorn University, Bangkok 10330, Thailand

\*Corresponding Author: Karu.C@chula.ac.th

#### **Abstract**

The objective of this study is to help adding to our understanding of two-dimensional flow past a pair of side-by-side arranged cylinders at low Reynolds number. In particular, the dependency of drag coefficient ( $C_d$ ), lift coefficient ( $C_l$ ) and characteristic frequency ( $St$ ) on the gap size ( $T$ ) between the two objects. The Reynolds number is 100, based on velocity of the free stream and cylinder diameter ( $D$ ). It is found that placing cylinders side-by-side increases drag on both objects, enhances lateral outward force (away from the other cylinder), as well as triggers a higher wake dominant frequency. As the gap width decreases the characteristic wake frequency, denoted by Strouhal number ( $St$ ), increases with the rate close to being linear, the drag coefficient increases quite quadratically, and the magnitude of lift coefficient increases exponentially, especially during which  $T/D$  is  $< 7$ . The influence from the other cylinder slowly diminishes as the gap widens and becomes negligible at about  $T/D = 15$ .

**Keywords:** Numerical simulation, flow past a cylinder, Drag, Lift, Strouhal number

## 1 Introduction

One of the classical problems in fluid mechanics concerns flow past a bluff body. This canonical flow appears in a wide range of engineering application such as coastal breakwater, offshore drilling rig, heat exchanger tubes and cooling towers, for example. Body structures immersed in such type of flow experience large drag force or flow-induced vibration that, under severe environments, can cause structural failure. The ability in foreseeing if the structure that obstructs a flow can withstand the stream without breaking down is undoubtedly thus important.

An extensive number of studies have been conducted for flow past a single object. Examples of the earlier studies are very briefly introduced as follows. [1] dealt with calculations and experiments on the flow past a stationary circular cylinder. [2] experimentally investigated the problem of drag and shedding frequency of many types of bluff body. [3] experimentally measured drag on a circular cylinder and investigated vortex street transition in its wake for the Reynolds number ranging 0.5-100. [4], among the very first numerical investigation, presented the finite-difference solutions of the equations of motion for unsteady incompressible flow around a circular cylinder for a range of Reynolds numbers from 5-100, revealing drag coefficient; angle

of separation; pressure and vorticity distribution on the cylinder surface. [5] used a numerical approach and focused on the pressure and velocity fields in the near wake.

A relatively smaller number of studies are conducted for flow past multiple bluff bodies. Among experimental studies, [6] visualized the wake behind two side-by-side circular cylinders and its evolution at Reynolds number of 25,000. [7] focused rather on the interaction between wake vortices with the similar multi-body arrangement as in [6] but at much lower Reynolds numbers ranging 50 – 200. Flows past various types of two cylinders configuration, such as side-by-side and tandem, was tackled by [8] who classified them into multiple regimes. Based on the works of [6-8], there exists a so-called critical gap between two side-by-side cylinders in which the slight parameter changes causes significant modification in the flow behavior. [9] numerically investigated incompressible flow past a cylinder pair, both tandem and side-by-side arrangements.

One of the remaining questions is the dependency of not only the characteristic wake frequency but body drag and lift coefficients upon the transverse gap, that also expands to a much larger degree. To

tackle such question, the objective of this study is to obtain and study the dependency of drag coefficient ( $C_d$ ), lift coefficient ( $C_l$ ) and characteristic frequency ( $St$ ) upon the gap size ( $T$ ) between the two objects that ranges from  $T/D = 1.5$  to 20.

## 2 Methodology

The investigation is conducted via a set of numerical simulations using ANSYS®, a commercial software capable of setting up and solving a variety of problems.

### 2.1 Problem setup

The computational domain, depicted in Fig. 1, consists of two cylinders of diameter  $D$ , placed apart at a transverse distance  $T$ , that obstruct the incoming free stream of velocity  $U_\infty$ . Reynolds number defined by  $Re = \rho U_\infty D / \mu$ ; where  $\rho$  is fluid density and  $\mu$  is fluid viscosity, takes the value of 100. Future study has been planned to increase  $Re$  to match those of real-world applications. Meanwhile, the rationale behind using  $Re = 100$  is to validate our results mainly against [10, 11].

The two-dimensional problem is set up and solved numerically in the dimensionless manner, where length is scaled by  $D$ ; velocity by  $U_\infty$ ; and time by  $D/U_\infty$ . Dirichlet boundary condition is applied on the left (inflow) edge of the computational domain for all velocity components and on the right

edge for pressure. Rests of the edges are restricted by the Neumann condition for all flow variables.

Statistical data is collected during the steady states, determined by inspecting the instantaneous vertical velocity signals at downstream far-end locations (not shown). To reach the steady states, the flows are allowed to march for about 4.5 flow throughs. This was guided by [8] where it took a non-dimensional time of approximately 150 (about 3.3 flow throughs in corresponding to our computational domain).

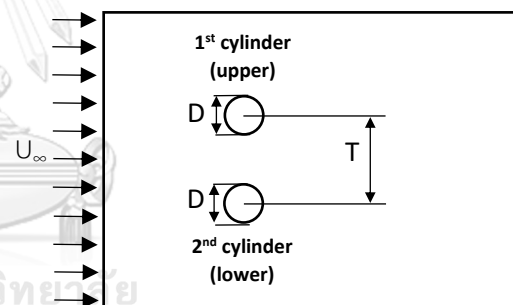


Fig. 1 Problem schematic description

### 2.2 Dependent variables

Fluid stream distributes force upon the surface of a bluff body it engulfs, as a result from both pressure and viscous shear stress. The resultant forces in the streamwise direction, called drag force ( $F_d$ ), and normal to streamwise direction, called lift force ( $F_l$ ), can be normalized by the  $D^2$  multiples of

dynamic pressure, resulting in the drag and lift coefficient:  $C_d = \frac{2Fd}{\rho U_\infty^2 D^2}$ ,  $C_l = \frac{2Fl}{\rho U_\infty^2 D^2}$ .

Strouhal number ( $St$ ) is used as a measure of characteristic frequency of the Von Karman type wake oscillation. It is defined by:  $St = f_s D / U_\infty$ ; where  $f_s$  is the wake dominant oscillation frequency, i.e., that corresponds to the largest energy content of the transverse velocity fluctuation.

### 3 Validation

Before we present the results of the primary problem stated above, a set of simulations of flow past a single cylinder at  $Re = 100$  is performed to obtain an optimal mesh (number and distribution), time step size, as well as to validate the setup by comparison against literatures for the baseline case, denoted R3, shown in Table 1. The data from [5, 10-13] came from numerical simulations and those from [3, 14] were measured experimentally. The set of simulations is conducted on a computational domain of size  $H=30D$  (height) and  $L=45D$  (length), shown in Fig. 2 (a).

#### 3.1 Baseline case

The baseline case (R3) is performed first to establish if the mesh and the time step size used can yield results that lie within the acceptable ranges (bounded by the reference values). The number of mesh

and time step size for this case are selected based solely on the availability of our computational resource. The result is shown in Table 1. and Fig. 3.

The obtained mean drag coefficient very well agrees with the previous computational studies [5, 10-12], where the maximum difference is about 1%, and differs from both experimental results [3, 14] within 2.2%. The amplitude of lift coefficient differs significantly from the numerical studies of [11] by 11.18% and [5] by 20.13%. However, the difference is found to be smaller as compared to the more recent numerical investigation of [10] (8.3%) and the experimentation of [12] (7.7%).

The calculated Strouhal number lies within 0.16-0.165, the range suggested by [2] and differs from the references for no more than about 2%.

**Table 1** Reference results for section 3

Cases	$C_d$	$C_l$	$S_t$
R3	1.350	$\pm 0.313$	0.164
Ding, H. [10]	1.356	$\pm 0.287$	0.166
Harichandan, A. [11]	1.352	$\pm 0.278$	0.161
Braza, M. [5]	1.364	$\pm 0.250$	0.160
Liu, C. [12]	1.350	$\pm 0.339$	0.165
Qu, L. [13]	1.317	-	0.165
Tritton, D. J. [3]	1.320	-	0.160
Wiesenberger, C. [14]	1.326	-	0.161

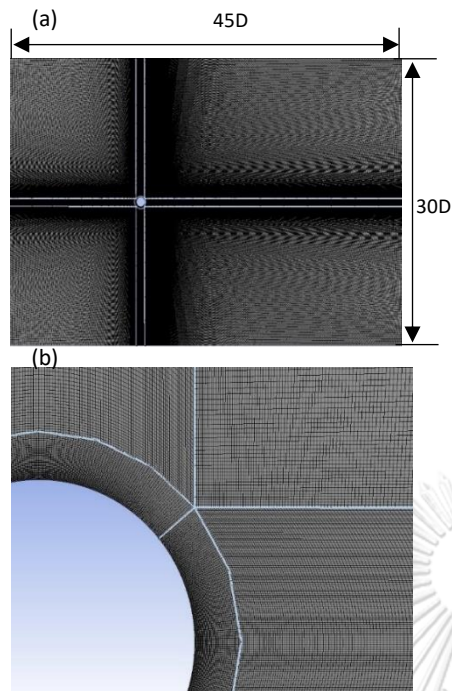


**Fig. 2** Computational domain (a) and near-cylinder meshes (b)

**Table 2** Results for section 3

Cases	Elements	$\Delta t$	Cd	Cl	St
R1	300,000	0.1	1.306	$\pm 0.2711$	0.1
R2	300,000	0.05	1.325	$\pm 0.2733$	0.14
R3	300,000	0.01	1.350	$\pm 0.313$	0.1636
R4	300,000	0.005	1.357	$\pm 0.325$	0.162
M1	675,000	0.01	1.340	$\pm 0.302$	0.160
M2	130,000	0.01	1.3586	$\pm 0.3185$	0.1556
M3	55,000	0.01	1.343	$\pm 0.3191$	0.160
M4	10,000	0.01	1.1635	$\pm 0.3205$	0.1261
M5	2,500	0.01	1.1826	-	0.0667

### 3.2 Time step size

We trialed the time step size that will be suitable for our simulation. The results are shown in table 2. Significant changes in St are observed for  $\Delta t$  in the range 0.01 – 0.1 while Cl is also sensitive to  $\Delta t$ , but especially when  $\Delta t$  is decreased from 0.05 to 0.01. Interestingly, the difference

between calculated Cd from the largest and the smallest time step size is less than 5%. We choose  $\Delta t = 0.01$  for the two-cylinder simulations based on the evidence in which St that is close to the reference values (St approximates at 0.162), listed as in Table 1, can sufficiently be captured at  $\Delta t$  in the order of 0.01.

### 3.3 Mesh sensitivity

As well as the trial of time step size, mesh sensitivity study includes 6 cases (M1-M5, and R3) with mesh distribution, shown in Fig. 2 (bottom), being almost identical in all the cases but the number of elements is scaled according to a preset value that ranges from 2,500 (M5) to 675,000 (M1). All the mesh convergence cases are obtained using time step size of 0.01.

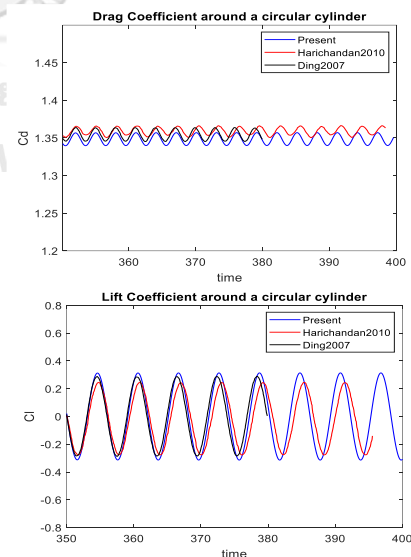


**Fig. 3** Drag and lift coefficients (Case R3)

The result in Table 2. indicates that a minimum number of elements is of the

order 55,000 (case M3) where the calculated  $C_d$ ,  $C_l$ , and  $St$  are close to the reference values (Table 1.). It is not clear why, in the M2 case,  $St$  deviates from the reference value (taken at 0.162) despite having more elements in comparison to the M3 case, providing that the mesh is distributed very similarly, while giving a better result in terms of  $C_d$  (reference value taken at 1.354) in comparison to the case M1 whose number of elements is larger by a factor of 5.

The number of elements in the order of 300,000-500,000 is chosen for the two-cylinder simulations based on the evidence that case R3, containing the number of elements being in the middle of M1 and M2, gives satisfactory results.

#### 4 Result

This section presents the results from simulations of flow past two side-by-side cylinders with the gap sizes  $T/D = 1.5$  and 3 in comparison to literatures, with the results shown in Table 3. and Fig. 5 (for  $T/D = 3$ ), as well as the dependency of  $C_d$ ,  $C_l$ , and  $St$  on the gap size ranging from  $T/D = 1.5$  to 20, with the results shown in Table 4.

##### 4.1 Case $T/D = 1.5$ and 3: comparison with literatures

As the problem is symmetric about a streamwise axis through the centerline between the two cylinders, the mean drag

coefficient must ideally be identical for both cylinders. Fig. 4 shows streamwise velocity contour for  $T/D = 3$ . This is however not the case from the present of result with  $T/D = 1.5$  as well as those of [10, 11]. Given that the temporal averaging is done for sufficiently long time during steady state, the difference seems to indicate a relatively large degree of  $C_d$  sensitivity upon how the simulation is setup, with respect to the trivial difference between the two  $C_l$  of both cylinders.

In fact, the expectation in capturing the ideal pair of  $C_d$  could be false and the sensitivity of  $C_d$  value can be partially numerical. There is a range of critical gap ( $1.1 < T/D < 2.2$ ) according to [8]. In this range, a complex interaction between two cylinders' wakes occurs resulting in a, if not almost, non-existent of the Karman-vortex streets (and thus a dominant frequency) and a problem that could only be marginally symmetric. Note that as the dominant frequency is not detected, Strouhal number is left blank in the Table 3. for the case with  $T/D = 1.5$ .

It is shown by [8] that the reappearance of the Karman-vortex streets once  $T/D > 2.2$ . At  $T/D = 3$ , the dominant frequency is detected and the Strouhal number is found to be at 1.81 that differs by less than 0.5% from the reference values

shown in Table 3. The drag coefficients are found to lie between that of [10, 11]. The lift coefficients are practically identical to [10] in the mean but not of their amplitudes.

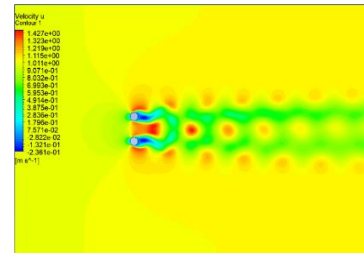


Fig. 4 Streamwise Velocity contour for case:  $T/D = 3$

Table 3 Drag Coefficient ( $C_d$ ), Lift Coefficient ( $C_l$ ) and Strouhal number ( $St$ ) comparison with the literatures

T	cases	Drag coefficient ( $C_d$ )		Lift coefficient ( $C_l$ )		Strouhal number ( $St$ )	
		1 <sup>st</sup> cylinder	2 <sup>nd</sup> cylinder	1 <sup>st</sup> cylinder	2 <sup>nd</sup> cylinder	1 <sup>st</sup> cylinder	2 <sup>nd</sup> cylinder
1.5D	Present Result	1.46	1.49	-0.46	0.47	-	-
	Ding, H. [10]	1.53	1.51	-0.46	0.47	-	-
	Harichandan, A. [11]	1.58	1.52	-0.41	0.41	-	-
3D	Present Result	1.52 $\pm 0.0345$	1.51 $\pm 0.0345$	-0.13 $\pm 0.45$	0.13 $\pm 0.45$	0.1812	0.1812
	Ding, H. [10]	1.56 $\pm 0.03$	1.56 $\pm 0.03$	-0.131 $\pm 0.253$	0.131 $\pm 0.253$	0.182	0.182
	Harichandan, A. [11]	1.45 $\pm 0.05$	1.45 $\pm 0.05$	-0.1 $\pm 0.25$	0.1 $\pm 0.25$	0.181	0.181

#### 4.2 Effects of the gap width

In this section, the coefficients and Strouhal number are considered for various gap widths. The result is shown in Table 4. and graphed in Fig. 6.

As  $T/D$  increases, all the interested dependent variables approach their corresponding values of the single cylinder. Placing cylinders side-by-side, at least for the  $T/D$  in the range studied here, increases drag; amplitude of lift force; as well as wake dominant frequency.

While obstructing a flow stream takes some streamwise momentum from it, obstructing and restricting the flow with an

additional object arranged as in the present study further removes streamwise momentum from the stream. The incoming flow that diverges transversely, while passing the cylinders, does not freely advect its own streamwise momentum away by its transverse velocity component that is restricted by the other cylinder. Such modification enforces the stream to deposit a larger amount of streamwise momentum to the cylinders resulting in the larger drag coefficient.

The increase of  $C_l$  magnitude can be explained in the similar manner. The transverse momentum of the incoming stream, while net-zero in total, distributes

into positive and negative portions as the flow goes around the object. Toward the centerline, the transverse momentum is not freely advected away by transverse velocity thus being enforced its larger deposit onto the cylinders.

Visualizing the result (Fig. 6) shows that while  $C_d$  and  $St$  gradually decreases as the gap increases,  $Cl$  magnitude drops sharply during  $T/D < 7$  signifying a strong influence from such span of gap size in modifying the flow stream in the transverse direction.

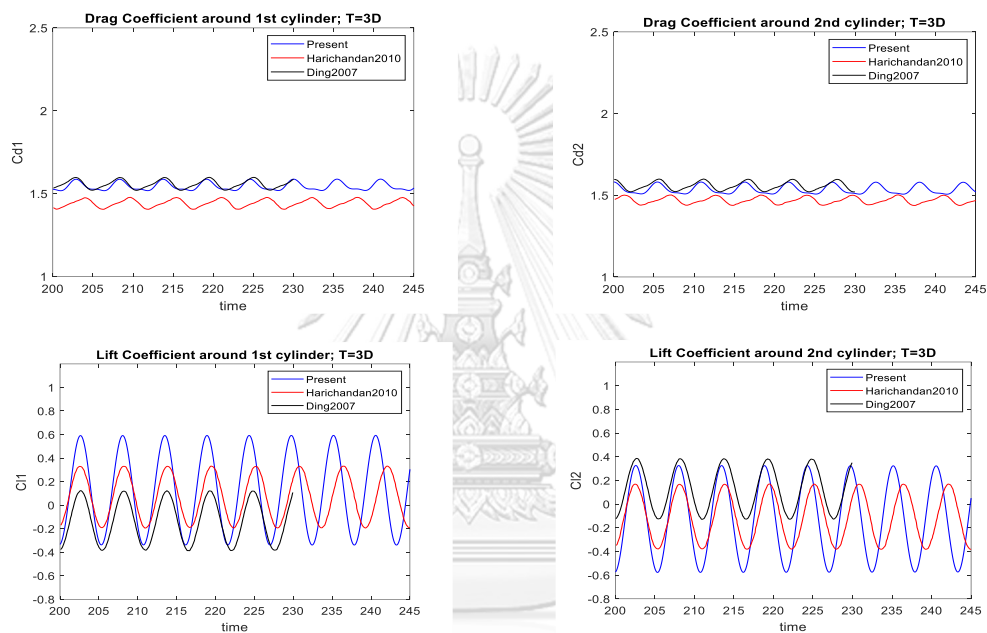


Fig. 5 Drag (top) and lift (bottom) coefficients of flow past two side-by-side cylinders for  $T/D = 3$

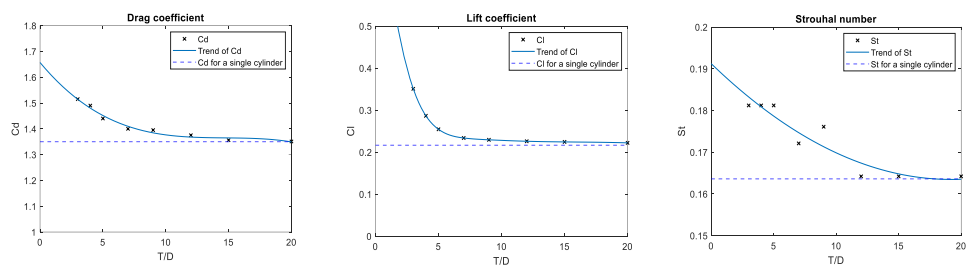


Fig. 6 Visualization of the results from Table 4. with trend lines



**Table 4** Results of the flow past two side-by-side circular cylinders at various gap width

T	Drag coefficient (Cd)			Lift coefficient (Cl)			Strouhal number (St)		
	1 <sup>st</sup> cylinder	2 <sup>nd</sup> cylinder	Average	1 <sup>st</sup> cylinder	2 <sup>nd</sup> cylinder	R.M.S.	1 <sup>st</sup> cylinder	2 <sup>nd</sup> cylinder	centerline
1.5D	1.46	1.49	1.475	-0.4558	4.667	-	-	-	-
3D	1.52	1.51	1.515	-0.13 ±0.45	0.13 ±0.46	0.3506	0.1812	0.1812	0.1812
4D	1.49	1.49	1.49	-0.0729 ±0.3907	0.731 ±0.3906	0.2864	0.1812	0.1812	0.1812
5D	1.44	1.44	1.44	-0.048 ±0.353	0.048 ±0.353	0.2543	0.1812	0.1812	0.1812
7D	1.40	1.40	1.40	-0.02585 ±0.3291	0.0258 ±0.3289	0.2336	0.1721	0.1721	0.1721
9D	1.395	1.395	1.1395	-0.0164 ±0.3226	0.0163 ±0.3277	0.2293	0.1761	0.1761	0.1761
12D	1.375	1.375	1.375	-0.00605 ±0.3161	0.0088 ±0.3161	0.2258	0.1642	0.1642	0.1642
15D	1.356	1.356	1.356	-0.0028 ±0.3138	0.0088 ±0.3138	0.2243	0.1642	0.1642	0.1642
20D	1.351	1.351	1.351	-0.0088 ±0.3192	-0.0088 ±0.3192	0.2220	0.1642	0.1642	0.1642
Single cylinder	1.350			±0.313		0.2164	0.1636		

## 5 Conclusion

A set of numerical simulations is carried out using the commercial software ANSYS®-Fluent to help adding to our understanding of incompressible viscous flow past a pair of side-by-side arranged cylinders at Reynolds number of 100, based on free stream velocity ( $U_\infty$ ) and cylinder diameter (D). In particular, the dependency of drag coefficient (Cd), lift coefficient (Cl) and characteristic frequency (St) upon the gap size (T) between the two objects are obtained and analyzed.

Validation is done via simulations of flow past a single cylinder at  $Re = 100$ . An approximate number of optimal mesh and time step size are obtained via mesh convergence and temporal resolution

studies. Simulations of flow past a pair of side-by-side arranged cylinders with  $T/D = 1.5$  and 3 are also validated with satisfactory result.

With respect to the flow past a single cylinder, for the gap width  $T/D < 20$  considered in this work, placing cylinders side-by-side increases drag on both objects, enhances lateral outward (away from the other cylinder) force, as well as triggers a higher wake dominant frequency. The effect slowly diminishes as the gap widens and becomes negligible for  $T/D$  about 15. It is found that as the gap width decreases, the characteristic wake frequency; denoted by Strouhal number, increases with the rate close to being linear, the drag coefficient increases quite quadratically, and the

magnitude of lift coefficient increases exponentially, especially during which  $T/D$  is  $< 7$ .

## 6 Acknowledgement

This work received financial support from Chulalongkorn University (CU-GR 63-34-21-02), and Micro/Nano Electromechanical Integrated Device Research Unit, Faculty of Engineering, Chulalongkorn University.

## 7 Reference

- [1] Thom A. (1933). Flow past cylinders at low speed, *Proceeding the Royal of Society*, vol.141, April 1933, pp. 651 – 669.
- [2] Roshko, A. (1954). On the development of turbulent wakes from vortex streets, National Advisory Committee for Aeronautics, no.1911.
- [3] Tritton D. J. (1959). Experiments on the flow past a circular cylinder at low Reynolds numbers, *Journal of Fluid Mechanics*, vol.6(4), November 1959, pp. 547 – 567.
- [4] Dennis, S. C. R. and Chang, G. (1970). Numerical solutions for steady flow past a circular cylinder at Reynolds numbers up to 100, *Journal of Fluid Mechanics*, vol.42(3), February 1970, pp. 471 – 489.
- [5] Braza, M., Chassaing, P. and Ha Minh, H. (1986). Numerical study and physical analysis of the pressure and velocity fields in the near wake of a circular cylinder, *Journal of Fluid Mechanics*, vol.165, April 1986, pp. 79 – 130.
- [6] Bearman, P. W. and Wadcock, A. J. (1973). The interaction between a pair of circular cylinders normal to a stream, *Journal of Fluid Mechanics*, vol.61(3), November 1973, pp. 499 – 511.
- [7] Williamson, C. H. K. (1985). Evolution of a single wake behind a pair of bluff bodies, *Journal of Fluid Mechanics*, vol.159, October 1985, pp. 1 – 18.
- [8] Zdravovich, M. M. (1977). Review of flow interference between two circular cylinders in various arrangements, *Journal of Fluids Engineering*, vol.99(4), November 1977, pp. 618 – 633.
- [9] Jester, W. and Kallinderis, Y. (2003). Numerical study of incompressible flow about fixed cylinder pairs, *Journal of Fluids and Structures*, vol.17(4), March 2003, pp. 561 – 577.
- [10] Ding, H., Shu, C., Yeo, K. S. And Xu, D. (2007). Numerical simulation of flows around two circular cylinders by mesh-free least square-based finite difference methods, *International Journal for Numerical Methods in Fluids*, vol.53, July 2006, pp. 505 – 332.

[11] Harichandan, A. B. and Roy, A. (2003). Numerical study of incompressible flow about fixed cylinder pairs, *International Journal of Heat and Fluid Flow*, vol.17(4), March 2003, pp. 561 – 577.

[12] Liu, C., Zheng X. and Sung, C. H. (1998). Preconditioned multigrid methods for unsteady incompressible flows, *Journal of Computational Physics*, vol.139, January 1998, pp. 35 – 57.

[13] Qu, L., Norberg C., Davidson, L and Peng, S. (2013). Quantitative numerical analysis of flow past a circular cylinder at Reynolds number between 50 and 200, *Journal of Fluids and Structures*, vol.39, May 2013, pp. 347 – 370.

[14] Wieselsberger, C. (1921). Neuere Feststellungen über die Gesetze des Flüssigkeits- und Luftwiderstandes, *Physikalische Zeitschrift*, vol.22(11), 1921, pp. 321 – 328.

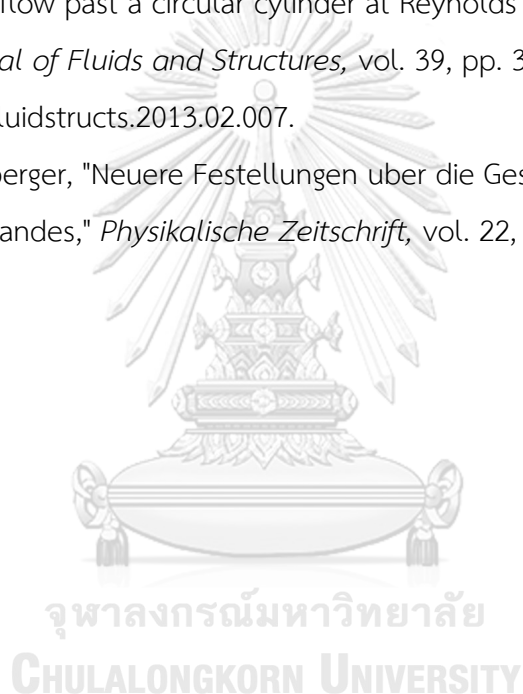
## REFERENCES

- [1] L. Rayleigh, "Acoustical observations," *The London, Edinburgh, and Dublin Philosophical Magazine and Journal of Science*, vol. 7, no. 42, pp. 149-162, 1879, doi: <https://doi.org/10.1080/14786447908639584>.
- [2] Hinterwaldner and Inge, "Parallel Lines as Tools for Making Turbulence Visible," *Representations*, vol. 124, no. 1, pp. 1-42, 2013, doi: 10.1525/rep.2013.124.1.1.
- [3] F. Ahlborn, "Über den Mechanismus des hydrodynamischen Widerstandes," *Abh. Geb. Naturwiss*, vol. 17, 1902.
- [4] H. Bénard, "Formation des centres de giration a L'arrière d'un obstacle en mouvement," *Comptes rendus de l'Académie des Sciences*, vol. 147, pp. 839-842, 1908.
- [5] R. Wille, "Kármán Vortex Streets," in *Advances in Applied Mechanics*, vol. 6, (Advances in Applied Mechanics, 1960, pp. 273-287.
- [6] A. Timme, "Über die Geschwindigkeitsverteilung in Wirbeln," *Ing Arch*, vol. 25, pp. 205-225.
- [7] M. V. Dyke, "An Album of Fluid Motion," *The Parabolic Press*, 1982.
- [8] D. E. Alexander, "Fluid Biomechanics," in *Nature's Machines*, 2017, pp. 51-97.
- [9] M. Bitan and D. Zviely, "Sand Beach Nourishment: Experience from the Mediterranean Coast of Israel," *Journal of Marine Science and Engineering*, vol. 8, no. 4, 2020, doi: 10.3390/jmse8040273.
- [10] U. Thampanya, J. E. Vermaat, S. Sinsakul, and N. Panapitukkul, "Coastal erosion and mangrove progradation of Southern Thailand," *Estuarine, Coastal and Shelf Science*, vol. 68, no. 1-2, pp. 75-85, 2006, doi: 10.1016/j.ecss.2006.01.011.
- [11] DMCR, การแก้ไขปัญหาการกัดเซาะชายฝั่งด้วยการปักไม้ไผ่ชะลอคลื่นโดยประชาชนมีส่วนร่วม. Ministry of Natural Resources and Environment, 2015.
- [12] Saengsupavanich and Cherdvong, "Erosion protection options of a muddy coastline in Thailand: Stakeholders' shared responsibilities," *Ocean & Coastal Management*, vol. 83, pp. 81-90, 2013, doi: 10.1016/j.ocecoaman.2013.02.002.
- [13] R. L. Panton, *Incompressible Flow*, 4th ed. John Wiley & Sons, 2013.

- [14] Bruce R. Munson, Theodore H. Okiishi, Wade W. Huebsch, and A. Rothmayer, *Fundamentals of Fluid Mechanics*, 7th ed. John Wiley & Sons Inc, 2012, p. 747.
- [15] A. Thom, "The flow past circular cylinders at low speeds," *Proceedings of the Royal Society of London. Series A, Containing Papers of a Mathematical and Physical Character*, vol. 141, no. 845, pp. 651-669, 1933, doi: 10.1098/rspa.1933.0146.
- [16] D. J. Tritton, "Experiments on the flow past a circular cylinder at low Reynolds numbers " *Journal of Fluid Mechanics*, vol. 6, no. 4, pp. 547-567, 1959.
- [17] A. Roskho, "On the development of turbulent wakes from vortex streets," 1954, vol. no.1911. [Online]. Available: <https://ntrs.nasa.gov/api/citations/19930092207/downloads/19930092207.pdf>
- [18] R. B. Payne, "Calculations of unsteady viscous flow past a circular cylinder," *Journal of Fluid Mechanics*, vol. 4, no. 1, pp. 81-86, 1958, doi: <https://doi.org/10.1017/S0022112058000318>.
- [19] M. Kawaguti, "Numerical Solution of the Navier-Stokes Equations for the Flow around a Circular Cylinder at Reynolds Number 40," *The Physical Society of Japan*, vol. 8, pp. 747-757, 1953, doi: <https://doi.org/10.1143/JPSJ.8.747>.
- [20] S. C. R. Dennis and G.-Z. Chang, "Numerical solutions for steady flow past a circular cylinder at Reynolds numbers up to 100," *Journal of Fluid Mechanics*, vol. 42, no. 3, pp. 471-489, 1970, doi: <https://doi.org/10.1017/S0022112070001428>.
- [21] M. Braza, P. Chassaing, and H. H. Minh, "Numerical study and physical analysis of the pressure and velocity fields in the near wake of a circular cylinder," *Journal of Fluid Mechanics*, vol. 165, pp. 79-130, 1986, doi: 10.1017/s0022112086003014.
- [22] C. Liu, X. Zheng, and C. H. Sung, "Preconditioned Multigrid Methods for Unsteady Incompressible Flows," *Journal of Computational Physics*, vol. 139, no. 1, pp. 35-57, 1998, doi: <https://doi.org/10.1006/jcph.1997.5859>.
- [23] P. Bearman and A. Wadcock, "The interaction between a pair of circular

- cylinders normal to a stream," *Journal of Fluid Mechanics*, vol. 61, no. 3, pp. 499-511, 1973, doi: <https://doi.org/10.1017/S0022112073000832>.
- [24] C. H. K. Williamson, "Evolution of a single wake behind a pair of bluff bodies," *Journal of Fluid Mechanics*, vol. 159, pp. 1-18, 1985, doi: <https://doi.org/10.1017/S002211208500307X>.
- [25] M. M. Zdravkovich, "Review of Flow Interference Between Two Circular Cylinders in Various Arrangements," *Journal of fluids Engineering*, vol. 99, no. 4, pp. 618-633, 1977, doi: <https://doi.org/10.1115/1.3448871>.
- [26] E. N. S. Ishigai, K. Nishimura, K. Cho, "Experimental Study on Structure of Gas Flow in Tube Banks with Tube Axes Normal to Flow : Part 1, Karman Vortex Flow from Two Tubes at Various Spacings," *Bulletin of the JSME*, vol. 15, pp. 949-956, 1972, doi: <https://doi.org/10.1299/jsme1958.15.949>.
- [27] A. Slaouti and P. Stansby, "Flow around two circular cylinders by the random-vortex method," *Journal of Fluids and Structures*, pp. 641-670, 1992, doi: [https://doi.org/10.1016/0889-9746\(92\)90001-J](https://doi.org/10.1016/0889-9746(92)90001-J).
- [28] H. Ding, C. Shu, K. S. Yeo, and D. Xu, "Numerical simulation of flows around two circular cylinders by mesh-free least square-based finite difference methods," *International Journal for Numerical Methods in Fluids*, vol. 53, no. 2, pp. 305-332, 2007, doi: 10.1002/flid.1281.
- [29] A. B. Harichandan and A. Roy, "Numerical investigation of low Reynolds number flow past two and three circular cylinders using unstructured grid CFR scheme," *International Journal of Heat and Fluid Flow*, vol. 31, no. 2, pp. 154-171, 2010, doi: 10.1016/j.ijheatfluidflow.2010.01.007.
- [30] M. Zhao, L. Cheng, B. Teng, and D. Liang, "Numerical simulation of viscous flow past two circular cylinders of different diameters," *Applied Ocean Research*, vol. 27, no. 1, pp. 39-55, 2005, doi: 10.1016/j.apor.2004.10.002.
- [31] P. S. Rudolph, "EXPERIMENTAL STUDY OF DUNE BUILDING WITH SAND FENCES," *Coastal Engineering Proceedings*, vol. 1, no. 8, 01/29 1962, doi: 10.9753/icce.v8.22.
- [32] C. Chinnarasri and S. Kittirart, "Mud Coastal Protection Using Triangular Modules of Breakwater Made of Bamboo," in *The Twenty-second International Offshore*

- and Polar Engineering Conference*, 2012, vol. All Days, ISOPE-I-12-507.
- [33] S. Dinh, T. Albers, and K. Schmitt, *Shoreline Management Guidelines Coastal Protection in the Lower Mekong Delta*. 2013.
- [34] J. Tu, G.-H. Yeoh, and C. Liu, "CFD Solution Procedure—A Beginning," in *Computational Fluid Dynamics*, 2013, pp. 31-60.
- [35] J. H. Ferziger and M. Peric, *Computational Methods for Fluid Dynamics*, 4th ed. Springer International Publishing, 2020, p. 596.
- [36] L. Qu, C. Norberg, L. Davidson, S.-H. Peng, and F. Wang, "Quantitative numerical analysis of flow past a circular cylinder at Reynolds number between 50 and 200," *Journal of Fluids and Structures*, vol. 39, pp. 347-370, 2013, doi: 10.1016/j.jfluidstructs.2013.02.007.
- [37] C. Wieselsberger, "Neuere Festellungen über die Gesetze des Flüssigkeits- und Luftwiderstandes," *Physikalische Zeitschrift*, vol. 22, no. 11, pp. 321-328, 1921.





จุฬาลงกรณ์มหาวิทยาลัย  
**CHULALONGKORN UNIVERSITY**



## VITA

NAME	Woraphon Wannaviroj
DATE OF BIRTH	13 March 1993
PLACE OF BIRTH	Songkhla, Thailand
INSTITUTIONS ATTENDED	B.Eng. Mechanical Engineering, Kasetsart University
HOME ADDRESS	68 Nakorn Nai Road, Boryang, Meung Songkhla, Songkhla, 90000
PUBLICATION	Wannaviroj, W. & Chongsiripinyo, K. (2021). Numerical study of flow past a pair of cylinders at a low Reynolds number. The 35th Conference of the Mechanical Engineering Network of Thailand.
AWARD RECEIVED	Runners-up Best Paper in the 35th Conference of the Mechanical Engineering Network of Thailand (ME-NETT 2021) from the Paper "Numerical study of flow past a pair of cylinders at a low Reynolds number" presented on July 22, 2021 via Zoom online meeting